UNIVERSITÀ DEGLI STUDI DI UDINE
DOTTORATO DI RICERCA IN
TECNOLOGIE CHIMICHE ED ENERGETICHE

Dynamics of large droplets in turbulent channel flow

Dott. Luca Scarbolo

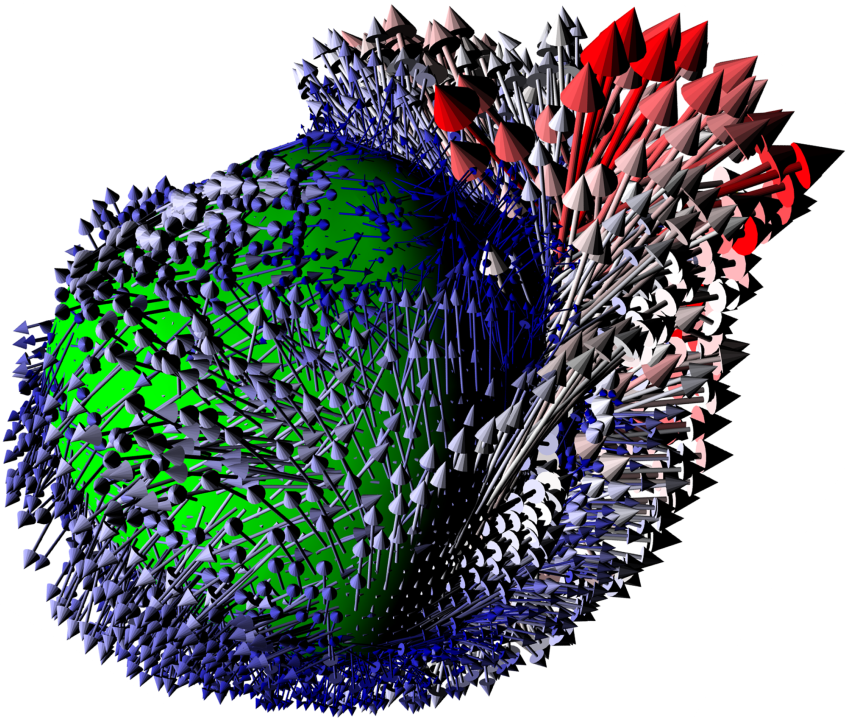

BOARD MEMBERS

Prof. Federico TOSCHI	REVIEWER
Prof. Roberto MAURI	REVIEWER
Prof. Cristian MARCHIOLI	REFEREE
Prof. Giuseppe PASCAZIO	REFEREE
Prof. Pietro POESIO	REFEREE
Prof. Alfredo SOLDATI	SUPERVISOR
Prof. Alfredo SOLDATI	DOCTORATE CHAIR

Author's Web Page: http://158.110.32.35/PEOPLE/Scarbolo.html

Author's e-mail: luca.scarbolo@uniud.com - scarbololuca@gmail.com

Author's address:

Dipartimento di Ingegneria Elettrica
Gestionale e Meccanica
Università degli Studi di Udine
Via delle Scienze, 206
33100 Udine – Italia
mobile. +39 347 3021010
web: `http://www.diegm.uniud.it`

Abstract

In this work the behaviour of large deformable droplets dispersed in a wall bounded turbulent flow has been investigated focusing on the role of the droplets deformability. A simplified physical problem has been considered: density differences and viscosity differences between the two fluids have been neglected while surface tension effects and coalescence/breakup events have been considered. A wide range of Weber numbers We (ratio between inertial forces and surface tension) have been investigated at moderate friction Reynolds numbers $Re_\tau = 100 \div 150$. Under these assumptions the problem represents an archetypal model of an industrial turbulent multiphase flow in which only hydrodynamics and capillary effects are considered. The problem has been studied applying a hierarchical decomposition: first the momentum transfer at the interface of a single large deformable non-breaking droplet in turbulence has been investigated, then the analysis has been extended to a swarm of large droplets: effects on the turbulent wall-drag and the coalescence rate have been measured. The results show flow field modifications in the vicinity of the droplet interface: the flow field deflections at the interface are smaller the larger is the interface deformability. As a consequence also an increment of the local shear stress is observed when decreasing the droplet deformability (namely, decreasing We). The role of deformability is central in the wall drag modifications produced by a large number of droplets; droplets with large Weber number can transport more efficiently small velocities from the near wall regions towards the high velocity regions of the channel center and vice-versa. The deformability is also a leading parameter in determining the coalescence rate and the possibility of breakup of the droplets swarm: when $We < 1$ (inertia smaller than surface tension), the coalescence rate is almost universal, while different coalescence rates and breakup phenomena are observed when $We > 1$ (inertial larger than surface tension). As a conclusion, large droplets in wall bounded turbulence can produce modifications of the flow field depending on their deformability. Significant Drag Enhancement (DE) is registered when the Weber number is smaller than a critical value ($We < We_c$), in particular the smaller is We, the larger is DE. Increasing We over a critical value We_c, no effects are observed on the flow. The coalescence events appear to be decorrelated from the DE: a universal coalescence rate is observed up to $We > 1$, while $We_c < 1$. This indicates that the wall drag modifications are weakly dependent on the droplet diameters d when their size is comparable to the channel height.

Contents

List of Figures

List of Tables

1

Introduction

The injection of small amounts of a disperse phase in wall bounded turbulent flows can produce a significant reduction of the wall drag that can reach 80%, depending on the flow characteristics. This effect has been known for long time: in 1948 Toms [121] observed an “unusually low friction factor” in dilute dispersed multiphase flows. Since then, for more than 60 years, the Drag Reduction (DR) produced by the injection of a dispersed phase in turbulent flows has been extensively investigated because of its wide practical and theoretical relevance: significant energy savings can be achieved in diverse industrial applications (i. e. long-distance fluid transport or movement of large size ships and vessels). Moreover, the study of dispersed turbulent multiphase flows has profound implications in the advancement of the fundamental knowledge of turbulence. Based on these motivations, many authors focused on the experimental, theoretical and numerical analysis of the DR phenomena in turbulent multiphase flows, showing that significant DR can be achieved with the adoption of limited amounts of polymers [129, 91, 134], fibers [51, 85, 8], additives [143, 133] or gas bubbles. Among these investigations, in the last decades many authors focused on the wall-drag modifications produced by the injection of air bubbles much larger than the dissipative turbulence scale in the near-wall region of a turbulent flow observing significant DR [126, 96, 82, 17]. Such turbulent multiphase system is very attractive because it has an important practical application: the reduction of the fuel consumption of large ships and vessels [64, 65, 136]. In fact the air injected near the vessels hull is a non-polluting, largely-available and economic gas that can be freely released in seas and oceans. Moreover, the ships hulls have a large flat bottom where, driven by buoyancy, the released bubbles can persist in the proximity of the wall [56].

Despite the DR produced by bubbles injection is widely known and many investigations have quantified the effect in diverse systems, the models and correlations proposed still give non-univocal and only qualitative results. The development of reliable and accurate models require a clear and robust knowledge of the DR mechanism that, at the moment, lacks. Since the presence of large deformable bubbles produce important modifications of the turbulence structures, the detailed investigation of the turbulence-interface interactions is required for a correct modelling of DR. These analysis have been limited by the complexity of the experimental and computational techniques necessary for the detailed observation of the turbulence-interfaces interactions. From the experimental point of view, the presence of a carried phase is a limiting factor for the optical measurement of the flow field [25], moreover the detection of the interface properties (i. e. deformations and velocity fields) is extremely complex [95]. From the numerical and theoretical point of view the analysis has been limited by three main factors: *i)* the detailed numerical description of the turbulent field [79, 90]; *ii)* the numerical description of deformable interfaces [28, 59, 5]; *iii)* the numerical approximation of large thermophysical properties gradients [123, 50] As a result, only few recent numerical and experimental studies have focused on the detailed description of the wall drag modification produced by large deformable bubbles in turbulence [70, 126, 128]. The Direct Numerical Simulations (DNS) of Lu *et al.* [70] highlighted the role of bubbles deformability in the wall-drag modification produced by a large number of bubbles with the same viscosity of the surrounding fluid and with a small density ratio ($\rho_f/\rho_d = 10$). They observed that large deformable bubbles released in a turbulent channel flow can produce Drag Reduction (DR) or Drag Enhancement (DE), depending on their deformability. Two situations were observed: *i)* bubbles characterized by large deformability produced a near-wall streamwise vorticity cancelling, resulting in DR; *ii)* bubbles with small deformability were slowed down by the near-wall flow field, producing an obstruction to the flow and resulting to DE. The mechanism proposed to explain the streamwise vorticity cancelling is the following: in their near-wall motion, the bubbles that can slide over the quasi-streamwise vortices located in the proximity of the wall. The bubbles squeeze the vortical structures against the opposite sign streamwise vorticity regions attached to the wall. As a result a mutual cancelling of the vorticity is obtained and the wall-drag is reduced. The recent experimental work of Van Gils *et al.* [128] measured important DR (up to 40%) when large deformable bubbles (with viscosity ratio $\rho_f \nu_f/\rho_b \nu_b = 100$ and a density ratio $\rho_f/\rho_d = 1000$) were released in a turbulent Taylor-Couette flow, highlighting the central role of the the bubbles deformability. The results of both investigations emphasized the importance of the bubbles deformability in the wall drag modification, however the DR mechanism is still not completely clear and further analysis are required. Those studies focused on bubbles characterized by inertial effects smaller than those of the surrounding fluid ($\rho_b << \rho_f$), in particular, combining their evidences, it appears that when the bubbles inertia is negligible DR is always achieved [128]. On the contrary, when the bubbles inertia is small, but still comparable with that of the surrounding fluids, the bubbles can produce both DR or DE, depending on their deformability [70] (governed by their surface tension).

In order to further clarify the role of the deformability in the contest of large deformable droplets or bubbles dispersed in turbulent wall-bounded flows, in this work the problem has been simplified neglecting the density differences and the viscosity differences between the droplets and the external flow, considering only the surface tension σ. Since the complex topological changes are dominated by the surface tension [42, 66, 113], also coalescence and breakup phenomena have been retained. The physical system defined through this simplifications is governed by two effects only: *i)* droplet deformability that is controlled by the surface tension; *ii)* droplet inertia that is comparable to that of the surrounding fluid. As a result the problem is set to its simplest configuration, where a minimal physics is involved. Through this simplification, the surface tension effects

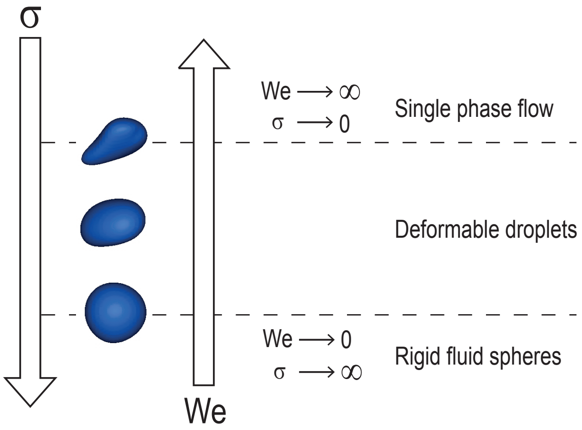

FIGURE 1.1 – Schematics of the physical system respect to the Weber number We and the surface tension σ. Two limit cases are identified: $We \to \infty$ ($\sigma \to 0$) yields to a single phase flow; $We \to 0$ ($\sigma \to 0$) yields to the dispersion of rigid fluid spheres.

are highlighted and a parametric analysis of the role of the droplet deformability can be performed in a system where the inertia of the droplet is non negligible. With this simplification, the droplets can be ideally created through the following procedure: once a fluid system is defined, a volume of fluid is divided from the surrounding fluid by introducing a membrane endowed with surface tension σ. Varying the surface tension the described physical systems can span from the single phase flow $\sigma = 0$ to the case of rigid fluid spheres $\sigma \to \infty$. A schematics of this process is reported in Fig. 1.1, where the connection to the Weber number $We \propto 1/\sigma$ is introduced. In order to give a comprehensive analysis of the phenomena involved, in this work the the simplified problem has been studied applying a hierarchical decomposition: first the behaviour of a single large deformable droplet in turbulence has been investigated, focusing on the momentum exchange at the interface. Then the analysis has been extended to a swarm of large droplets, considering their macroscopic effects on the wall drag turbulence and their collective behaviour (i.e. droplet-droplet collisions, coalescences and breakups)

The numerical analysis of the simplified system described above has been performed adopting a Direct Numerical Simulation (DNS) of the turbulent wall bounded flow, coupled with the Phase Field Model (PFM) for the interface tracking. The DNS technique allows to solve all the length and time scales involved in the turbulent flow, giving a complete and predictive description of the complex turbulent motions [54, 79, 90]. The PFM is a comprehensive theoretical framework that allows to describe, with high accuracy, the behaviour of deformable fluid interfaces. In particular the PFM is one of the most accurate methods for the numerical analysis of breakup [92, 86] and coalescence [113, 73, 86, 140] phenomena. Thus, the DNS-PFM technique adopted in this work represents one of the most developed frameworks for the quantitative analysis of turbulent multiphase flows with complex interfacial dynamics.

Thesis outline

The present work is structured as follows:

- Chap. 2: the governing equations are reported and discussed in detail; in the first section the different approaches for the interface modelling are proposed and in the second section the governing equations of the diffuse interface model are derived. In the third section the mass conservation equation and momentum balance equations are introduced and particularized for the multiphase system under analysis. In the last section the dimensional analysis of the governing equations is proposed.
- Chap. 3: the numerical algorithm adopted for the solution of the governing equations is derived and discussed in detail. In the first section, the governing equations are rewritten and the solution algorithm is exposed; in the second section the spectral approximation of the solution is shown and, in the last section, the discretized set of equations is reported.
- Chap. 4: the numerical method proposed is validated against selected benchmarks. In the first section the problem of a single droplet deformed under shear flow is solved and the results are compared to the available analytical solution. In the second section the accuracy of the method is discussed in comparison with two widely adopted Lattice Boltzmann multicomponent algorithms.
- Chap. 5: the transport of momentum across the interface of a deformable droplet in a turbulent channel flow is investigated considering a wide range of Weber numbers. In the first section the problem is posed and the details of the simulations are provided; in the second section the droplet deformation and the turbulence features at the droplet interface are discussed in detail.
- Chap. 6: the role of deformability in the dispersion of a large number of droplets in a turbulent channel flow is investigated. The droplet-droplet interactions and the wall-drag modifications produced by the droplets swarm are studied exploring a wide range of Weber numbers. In the first section the problem is described, providing the details of the simulations. In the second section the coalescence regimes are discussed in detail and in the third second section the flow field modifications are quantified.

I

Methodology

2

Governing equations

In this chapter the governing equations are reported and discussed in detail. In the first section the different approaches for the multiphase flows modelling are summarized and briefly reviewed. In the second section the phase field model is introduced, then its governing equations are derived and adapted to the physical problem here considered. In the last section the dimensional analysis of the governing equations is proposed.

2.1 Multiphase numerical simulations

The theoretical and numerical analysis of dispersed turbulent multiphase flows requires the definition and solution of a set of governing equations that describe the behaviour of each constituent of the system. Depending on the physical properties of the constituents, their governing equations can be based on diverse approaches: i.e. the continuous fluid phases are usually described by a set of Eulerian continuity and momentum balance equations (Navier-Stokes equations), while diverse approaches can be adopted for the dispersed phases. In the most general case, the governing equations of the different constituents have to be coupled together, in this way mass, momentum and energy exchanges between the system constituents can be accounted (i.e. drag forces, collisions and capillary forces). Following this general description, the physical model equations can be extremely complex and their solution can require numerical algorithms and computational resources beyond those currently available (i.e. direct numerical simulations of turbulent flows at high Reynolds numbers are still non feasible nowadays). However several approximations can be introduced depending on the properties of the physical system considered and, accordingly, different numerical frameworks can be adopted (i.e. the point-wise approximation of particles [24] or Large Eddy Simulation LES of high Reynolds number flows). When considering multiphase flows laden with finite size deformable bodies, namely the dispersion of large deformable droplets in turbulence, the evolution of the system can be summarized in two steps: *i*) interface advection, *ii*) flow field solution. Fig. 2.1 shows a schematic representation of these two steps, where the initial conditions at time t and the final solution at time $t + \Delta t$ are represented by the subscripts n and $n + 1$, respectively. First the interface Ω_n is advected and the new interface Ω_{n+1} is obtained; the displacements of the interface are computed on the basis of the velocity field $\mathbf{u}_n$ that are known at time t. This step requires the definition of a theoretical and numerical framework able, in principle, to reproduce the pure advection of the interface on the basis of the local velocity field. Once the interface has been advected, the local surface forces $\mathbf{f} = \sigma/\bar{r}$ are computed and introduced into the Navier-Stokes equations; in this case only the local capillary forces are considered, but more complex interfacial phenomena can be accounted. The solution of the flow field governing equations modified with the local surface forces requires particular theoretical and numerical models able to treat efficiently the local force variations produced by the presence of the interface. Moreover, since the problem considered in this work involves the Direct Numerical Simulation (DNS) of turbulent flows, a robust and accurate numerical algorithm is required.

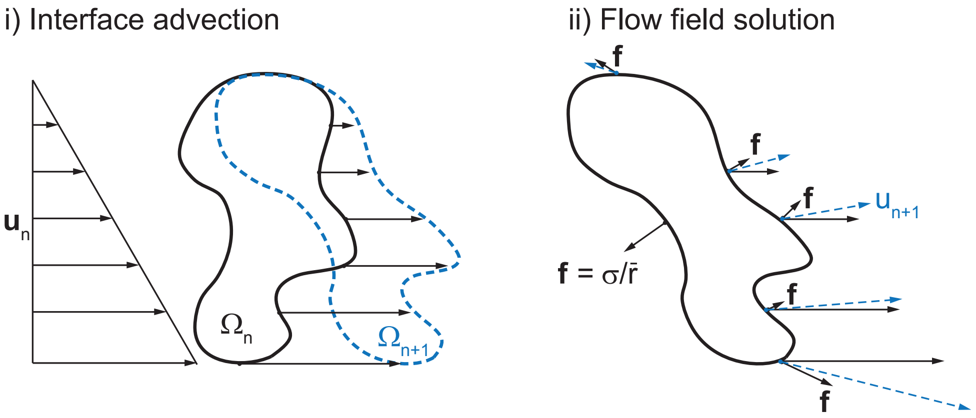

FIGURE 2.1 – Schematic representation of the simulation of a multiphase flow with a deformable interface, subscripts n and $n+1$ stand for the time level t and $t+\Delta t$, respectively. Given the velocity field $\mathbf{u}_n$, the interface Ω_n is advected and the resulting interface is represented by the dashed blue line Ω_{n+1} (left panel). Once the interface position Ω_{n+1} is known, the local surface forces $\mathbf{f}$ are computed (i.e. the capillary forces here presented are proportional to the local curvature $1/\bar{r}$ and directed along the interface normal direction $\mathbf{n}$) and the velocity field is modified adding the force to the Navier-Stokes solution. As result the updated velocity field $\mathbf{u}_n$ is obtained.

2.1.1 Advection of interfaces

The time evolution of a deformable interface, namely the interface advection, requires to describe the interface position at any time; the interface movement is the result of the displacements produced by the velocity field over the single small interface elements (see the schematic representation of Fig. 2.1). The deformed interface reacts with a local force $\mathbf{f}$ that modifies the local flow field, in this way the surface tension effects are kept into account. This procedure requires the the development of a theoretical and numerical frameworks that can be either based on the continuous description of the interface, or on the sharp description of the interface. In the sharp description, the interface is represented as a two dimensional surface, namely a zero-thickness interface; the advection of such a surface is obtained adopting different numerical methods, as the

Front Tracking (FT) [125] or the Volume Of Fluids (VOF) [43]. The FT is based on the Lagrangian advection of some marker points deployed over the interface (or front), once their position is updated, the interface shape is reconstructed adopting tailored geometrical approaches. The VOF is based on a concentration function C defined at the computational cells center; C assumes uniform values $C = 1$ and $C = 0$ in the bulk fluids, while it assumes values $0 \leq C \leq 1$ in cells crossed by the interface. The concentration function C is evolved in time considering the cell faces fluxes and, from the cell value of C the interface is reconstructed. Both FC and VOF require interface reconstructions that involve complex algorithms (in particular for three dimensional simulations) that can lead to inaccurate computation of the local normal vectors $\mathbf{n}$ and the local curvature radius $\bar{r}$ that are required for the flow field forcing. Moreover complex topological changes (i.e. breakup and coalescence) need to be carefully and often artificially accounted. By contrast VOF is extremely accurate in the local mass conservation and the FT appears to be more flexible in the introduction of complex physical behaviours. In the continuous description, the interface evolved in time through the advection of a continuous scalar function $\phi(\mathbf{x})$ whose level-set $\phi = 0$ identifies the actual position of the interface. Within this framework, the most common approach is the so-called Level Set (LS) method [102], were the continuous field ϕ is evolved in time by solving the following pure advection equation:

$$\frac{\partial \phi}{\partial t} + \mathbf{u} \cdot \nabla \phi = 0. \tag{2.1.1}$$

Due to numerical round-off errors that are present even with the high order schemes adopted (i.e. $5^t h$ order WENO schemes), the solution of Eq. 2.1.1 is affected by a numerical diffusion that degrades the interface in time and, as a result, correct computation of local properties (i.e. curvature and normal vectors) requires the solution of a reinitialization equation that does not ensure the local mass conservation [50]. Among the interface tracking methods based on the continuous approach, the Phase Filed Model (PFM) can be found. In this method the numerical diffusion that is the origin of the interface degrading, is circumvented by advecting the scalar field ϕ through a conservative potential-driven advection-diffusion equation. A detailed description of the method will be given in section Sect. 2.2.

2.1.2 Flow field solution

From the theoretical point of view, the evolution of the fluid field is given by a set of independent governing equations (i.e. mass, momentum and energy) written for each fluid domain and coupled through a set of interface boundary conditions, yielding to a free-boundary problem [60, 6]. The interface boundary conditions are obtained through mechanical equilibrium concepts that involve the interface properties, such as the surface tension. I. e. the stress balance across a sharp interface endowed with surface tension σ yields to the following jump condition of the stress tensor $\boldsymbol{\tau}$:

$$\boldsymbol{\tau}|_i^o = \frac{\sigma \mathbf{n}}{\bar{r}} - \nabla \sigma, \tag{2.1.2}$$

where $1/\bar{r}$ is the interface local mean curvature, $\mathbf{n}$ is the interface normal vector and the superscripts o, i refer to the different sides of the interface. When considering immiscible fluids, there is no mass transfer at the interface and the mass balance across the interface yields to the following jumps of the interface-normal velocity component:

$$\mathbf{u} \cdot \mathbf{n}|_i^o = u_n|_i^o = 0. \tag{2.1.3}$$

Applying then the no-slip condition at the interface, also the tangential velocity component is continuous:

$$\mathbf{u} \cdot \mathbf{t}|_i^o = u_t = 0, \tag{2.1.4}$$

where $\mathbf{t}$ is the interface tangential vector. According to the problem under analysis, the stress and velocity jumps (2.1.2)-(2.1.4) can assume various formulations, in particular, when the surface tension is uniform, $\boldsymbol{\tau}|_i^o = \sigma\mathbf{n}/\bar{r}$ (refer to Leal [66] and Gatignol *et al.* [30] for a complete discussion). The theoretical framework described above can be numerically solved by adopting either a sharp approach or a continuous approach. Among the sharp approaches, the Ghost Fluid Method (GFM) [28] is one of the most adopted for the Direct Numerical Simulations (DNS) of turbulent flows. Within this approach, the interface boundary conditions are applied as jumps of velocity and stress tensors across a zero-thickness interface. Despite the computational accuracy granted by the GFM, its application is convenient only adopting prediction-correction algorithms, moreover smearing of the viscous stresses is usually required across the interface [33] limiting the sharp nature of the method. In the continuous approach the local surface forces are applied by adding a continuous volume force smeared over a thin layer across the interface location; in this way the conditions on the velocity continuity are immediately satisfied by solving the continuity equation. Among these approaches the most used are the Force Coupling (FC) [124], and the Phase Field Model (PFM); these two methods can be coupled with both a continuous or sharp interface advection methods but in most of its applications a comprehensive PFM framework is adopted for both the advection of the interface and the flow field solution. The direct equivalence between PFM and the FC will be given in the next Sect. 2.2.4

2.2 The Phase Field Model

2.2.1 Origins of the model

The study of multiphase immiscible fluid systems focused the attention of several authors on the nature of the interface. The first idea, proposed by Young Laplace and Gauss in the early 19^{th} century, was to consider the fluid-fluid interface as a sharp zero-thickness surface provided by some physical properties (i.e. surface tension). During the mid 19^{th} century, almost simultaneously to the development of the sharp or classical approach, Poisson [89], Maxwell [76] and Gibbs [32] started to study the continuous nature of the fluid-fluid interfaces. They represented the interface as a steep but continuous variation of the thermophysical properties from one fluid to the other; in particular Gibbs introduced the concepts of “dividing surface” and surface “excess quantities”, that were the basis for the development of the equilibrium thermodynamics of the continuous approach also known as Diffuse Interface (DI) model. Based on those works, Lord Rayleigh [93] and Van der Waals [127] started to developed in detail the diffuse interface theory and, in particular, Van der Waals used his equation of state to predict the interface thickness of a mixture, showing that it tends to infinite when the mixture approaches critical conditions. In this contest, Korteweg [57] developed the constitutive law for the capillary stress that arises at the fluid-fluid interfaces. Despite the idea of the diffuse interface was introduced only few years after the sharp interface approach, for almost one century it played a minor role remaining almost undeveloped. In the middle of 20^{th} century, the increased interest on the near-critical phenomena triggered the development of the diffuse interface models. Cahn and Hilliard [15, 16] adopted the diffuse approach to the description a binary fluid mixture undergoing spinoidal decomposition. Then, based on the constitutive law developed by Korteweg, the diffuse description of the interface was coupled with the hydrodynamics [52, 115, 44] referring to the "Model-H" which only later was named "diffuse interface model" and known also as "phase field model". In the last 40 years the increased computational resources created the necessary conditions for the development of the Phase Field Model (PFM) that requires high resolutions and robust numerical schemes. The main reasons for its success are the possibility to overcame certain theoretical limits of the sharp interface methods: *i*) problems where the interface thickness l_ξ is comparable to the problem length scale (i.e near critical phenomena) are the natural environment for the diffuse interface models; *ii*) detailed interface-solid walls interaction can be easily introduced (i.e. contact angle or interface laden by solid particles); *iii*) topological changes (i.e. breakup or phase transitions) can be correctly and easily reproduced because of the thermodynamic origin of the model. In particular the PFM models can be adopted as predictive tools in the analysis droplet coalescence [113, 73, 86, 140] or in droplet breakups [92, 86]. From the numerical point of view the diffuse approximation of the interfaces can overcame some unwelcome features of other approaches: *i*) larger accuracy is granted in the interface description: the thermodynamically conservative nature of the model avoids the interface detriment and the need of correction techniques; *ii*) the constitutive law for the capillary stress yields to an accurate description of the interfacial forces; *iii*) proper scaling of the equation parameters allow to extend the model also to the description of immiscible fluid systems. However the diffuse interface model is characterized by some limitations that reduce its applicability: some issues concerning the local mass conservation still arise when modelling immiscible multiphase flows [141, 99, 100]. Moreover the governing equations involve high order (namely 4^{th}-order) operators that require robust and stable numerical methods [5]. The PFM is based on a continuous approach in which the interface between two fluids is a layer of finite thickness rather than a sharp discontinuity. Across the interfacial layer the physical properties of the fluid components vary in a smooth and continuous way from one fluid to the other: the interface volume is a region of controlled diffusion where the two fluids can mix. This assumption has realistic theoretic foundations when considering near-critical mixtures: the interface thickness increases when approaching the critical conditions (as observed by Van der Waals [127]). When the continuous approach is applied to the description of immiscible fluid systems far from the critical region, a fictitious enlargement of the interface should be applied: real interfaces have a thickness of few molecules, namely $O(l_\xi) = 10^{-9}$m [78, 31], that require numerical resolutions that are beyond the current available limits. At that scales the continuous nature of the interface emerges (mixing layer of few molecules thickness), however the continuum hypotheses does not apply, thus, in those cases, the applicability of this approach should be considered with attention. In the Phase Field Model the state of the system is described, at any time, by a scalar order parameter ϕ, which is a function of the position vector $\mathbf{x}$. Differently from the Level Set (LS), in the PFM the order parameter directly represents one of the physical properties of the fluid (i.e. density or molar concentration) and all the remaining properties are in turn modelled as proportional to $\phi(\mathbf{x})$ [5, 99]. According to the continuous approach, the order parameter is mathematically continuous over the entire computational domain (due to the continuous approximation of the interface) and it shows smooth variations across the interface between single fluid regions, where it assumes mostly uniform values. Coupling the continuous representation of the two fluid field with a conservative transport equation of the order parameter, the system evolution can be resolved in time. It worth notice that the conservative nature of the model is a key point for its application to the description of immiscible fluid systems, in fact in this way the detriment of the interfacial layer is avoided and the capillary properties of the interface (i.e. surface tension) are recovered. The best-known PFM is represented by the Cahn-Hilliard equation, where the evolution of the order parameter is driven by the minimization of a suitable chemical potential. Cahn and Hilliard [15, 16] generalized the work of Van der Waals [127] to a time-dependent system by approximating interfacial diffusive fluxes as being proportional to the chemical potential gradients. Within the PFM theoretical framework, the capillary effects produced by the interface on the surrounding fluid are described through a force that is derived from the Korteweg stress tensor [57]. This local force is consisten with the thermodynamic derivation of the Cahn-Hilliard equation, as a result the PFM gives a coherent physical description of both the interface advection and the flow field solution.

2.2.2 The Cahn-Hilliard equation

Following the approach proposed by Cahn and Hilliard [15, 16], the evolution of the multiphase system is described by a generalized mass conservation equation:

$$\frac{\mathrm{D}\phi}{\mathrm{D}t} = -\nabla \cdot \mathbf{J}, \tag{2.2.1}$$

where $\mathbf{J} = -M\nabla\mu$ is a phase field flux (i.e. a generalized mass flux) responsible to drive the system toward its equilibrium conditions following a chemical potential μ. Substituting the phase flux into Eq. (2.2.1) and expanding the total derivative, the convective Cahn-Hilliard equation is obtained:

$$\frac{\partial\phi}{\partial t} = -\mathbf{u} \cdot \nabla\phi + \nabla\left(M\nabla\mu\right), \tag{2.2.2}$$

where $\mathbf{u}$ is the velocity field, $M = M(\phi)$ is the mobility or Onsager coefficient that controls the interface relaxation time and μ is a chemical potential that controls the interfacial layer behaviour. Eq. (2.2.2) models the evolution in time of a diffuse interface in particular it can represent the advection of the scalar field ϕ where the interface does not degrade by numerical diffusion [48, 139, 18] and where complex topological interfaces modifications, namely breakup, coalescence and critical phenomena [81, 61]. Those phenomena are driven by the minimization of the chemical potential μ that is defined as the functional derivative of the free energy functional $f[\phi]$:

$$\mu = \frac{\delta f[\phi(\mathbf{x})]}{\delta \phi}. \tag{2.2.3}$$

The free energy $f[\phi]$ is a conservative, thermodynamically consistent functional that can assume suitable definitions according to the problem under analysis. The PFM representation of an immiscible binary mixture of isothermal fluids is given by the following free energy functional:

$$f[\phi(\mathbf{x})] = f_0 + \frac{1}{2}\kappa|\nabla\phi|^2 \tag{2.2.4}$$

where, in this case, ϕ represents the relative concentration of the two fluid components. The first term on the right-hand-side of Eq. (2.2.4) is the ideal part of the free energy that keeps into account the tendency of the system to separate in pure fluids clusters. For two immiscible fluids, the phobic behaviour can be approximated by a double-well formulation [36] which shows two minima corresponding to the two stable fluid phases:

$$f_0 = \frac{\alpha}{4}\left(\phi - \sqrt{\frac{\beta}{\alpha}}\right)^2 \left(\phi + \sqrt{\frac{\beta}{\alpha}}\right)^2, \tag{2.2.5}$$

where α and β are two positive constants that define the interface properties. The functional (2.2.4) is also know as the Gizburg-Landau free energy. In the continuous diffuse representation of the multiphase fluid system, the two fluids are allowed to mix into the interfacial layer where they store a mixing energy that is kept in account by the non-local term $1/2\kappa|\nabla\phi|^2$ of Eq. (2.2.4). The mixing energy stored into the interfacial layer is controlled by the positive parameter κ and it is the origin of the surface tension in to the PFM. Introducing the double-well potential (2.2.5) into Eq. (2.2.4), the chemical potential for an immiscible binary mixture is obtained:

$$\mu(\phi) = \alpha\phi^3 - \beta\phi - \kappa\nabla^2\phi. \tag{2.2.6}$$

The relative concentration equilibrium profile across the interface is given by the competition of the two terms appearing in the free energy formulation and can be obtained by minimizing the free energy functional (2.2.4) with respect to the variations of the order parameter, namely setting the chemical potential (2.2.6) to zero:

$$\mu = \frac{\delta f[\phi]}{\delta \phi} = 0 \Rightarrow \alpha\phi^3 - \beta\phi - \kappa\nabla^2\phi = 0. \tag{2.2.7}$$

The integration of Eq. (2.2.7) for a mono-dimensional planar interface, where $\phi(z \to \pm\infty) = \phi_\pm$, yields two stable solutions $\phi_\pm = \pm\sqrt{\beta/\alpha}$ and the following non-uniform solution:

$$\phi(z) = \phi_+ \tanh\left(\frac{z}{\sqrt{2}\xi}\right). \tag{2.2.8}$$

The capillary width $\xi = \sqrt{\kappa/\beta}$ is the interface length scale; in particular $-0.9 \leq \phi/\phi_+ \leq 0.9$ across a layer of $l_\xi = 4.164\xi$ that contains the 98.5% of the interface surface tension [5, 139]. The profile of a plane interface and the double well free energy f_0 are reported in the left and right panels of Fig. 2.2, respectively.

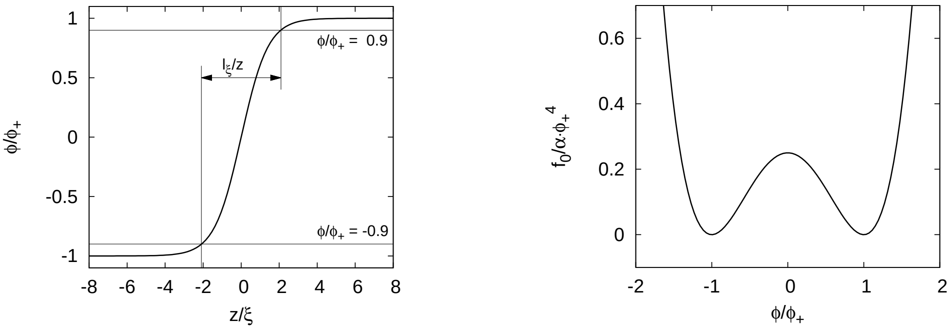

FIGURE 2.2 – Schematic representation of the equilibrium interface profile $\phi(z)$ across a flat interface (left) and the Gizburg-Landau free energy f_0 (right).

2.2.3 The incompressible Navier-Stokes equations

In the PFM, the velocity field evolution for a multiphase system is given by a single set of continuity and momentum equations written for the whole system, in which the thermophysical properties are dependent on the order parameter ϕ. Through this model the capillary forces that arise at the interface are introduced using the Korteweg stress tensor [57]:

$$\boldsymbol{\tau}_c = \kappa \nabla\phi \times \nabla\phi. \tag{2.2.9}$$

Considering a system composed by of Newtonian fluids with matched densities and matched viscosities, the modified Navier-Stokes equation yields to the following:

$$\rho\frac{\partial \mathbf{u}}{\partial t} + \mathbf{u}\cdot\nabla\mathbf{u} = \nu\rho\nabla\cdot\left(\nabla\mathbf{u} + \nabla\mathbf{u}^T\right) - \nabla p + \nabla\cdot\boldsymbol{\tau}_c, \tag{2.2.10}$$

where $\mathbf{u}$ is the velocity vector, p the pressure term, ρ is the fluid density and ν is the fluid kinematic viscosity. In the most general case, the fluids are characterized by different density and viscosity that can be described as dependent to the phase field $\rho = \rho(\phi)$ and $\nu = \nu(\phi)$. In those cases the adoption of a variable viscosity is straightforward (see [146] for a detailed description of the variable viscosity treatment), whereas variable densities lead to so called quasi-incompressible systems that are still argument of debate in the PFM community [69, 27]. The "stress form" of the momentum balance equation (2.2.10) can be rewritten in an equivalent "potential form" [48] where the capillary force term shows a direct dependence on the chemical potential μ:

$$\rho\frac{\partial \mathbf{u}}{\partial t} + \mathbf{u}\cdot\nabla\mathbf{u} = \nu\rho\nabla\cdot\left(\nabla\mathbf{u} + \nabla\mathbf{u}^T\right) - \nabla\tilde{p} + \mu\nabla\phi, \tag{2.2.11}$$

where $\tilde{p} = p + \nabla f$ is a modified pressure term and $\mu \nabla \phi$ is the capillary force. The dimensional form of the continuity equation reads:

$$\nabla \cdot \mathbf{u} = 0. \tag{2.2.12}$$

Since $\rho = const$, Eq. (2.2.12) is exactly the same of adopted to describe incompressible single phase flows. Thanks to the conservative nature of the PFM, the interfacial layer does not diffuse; as a result $\nabla \phi$ keeps the property of a signed distance and the momentum transfer to the flow field is resolved with high accuracy. The surface tension σ is defined as the specific energy stored into the interfacial layer; applying the definition to Eq. (2.2.7), the following value of the surface tension is obtained:

$$\sigma = \kappa \int_{-\infty}^{+\infty} (\nabla \phi \cdot \mathbf{n})^2 \, \mathrm{d}\mathbf{n} = \frac{\sqrt{8}}{3} \frac{\kappa^{\frac{1}{2}} \beta^{\frac{3}{2}}}{\alpha}. \tag{2.2.13}$$

Once the interface thickness ξ and the equilibrium solutions $\phi_{\pm}$ are fixed, Eq. (2.2.13) allows to define the free energy parameters α, β and κ necessary to achieve the desired surface tension value. Although the fictitious enlargement of the interface necessary for its numerical resolution[1], the PFM can describe the desired value of σ by a selection of the free energy functional coefficients [139]. The derivation described above has been adopted and reviewed by several authors [1, 63] moreover the convergence of Eq. (2.2.2) to the "sharp interface limit" has been recently proven by Yue [142] and Magaletti [73] among the others.

2.2.4 Matching with the Force Coupling

In order to directly compare the PFM with the force coupling method, the modified Navier-Stokes Eq. (2.2.11) is rewritten in the following way, where the adoption of the modified pressure $\tilde{p}$ is avoided:

$$\rho \frac{\partial \mathbf{u}}{\partial t} + \mathbf{u} \cdot \nabla \mathbf{u} = \nu \rho \nabla \cdot \left(\nabla \mathbf{u} + \nabla \mathbf{u}^T \right) - \nabla p + \mu \nabla \phi - \nabla f. \tag{2.2.14}$$

The force term $\mathbf{f}_c = \mu \nabla \phi - \nabla f$ is expanded introducing the free energy functional of Eq. (2.2.4):

$$\begin{aligned} \mathbf{f}_c &= \mu \nabla \phi - \nabla f \qquad (2.2.15) \\ &= \left(\alpha \phi^3 - \beta \phi \right) \nabla \phi - \kappa \nabla^2 \phi \nabla \phi - \frac{\partial f}{\partial \phi} \nabla \phi \\ &= -\kappa \left(\nabla \cdot \nabla \phi \right) \nabla \phi. \end{aligned}$$

Starting from a scalar field ϕ, the average curvature $1/\bar{r} = 1/2(1/r_1 + 1/r_2)$ and the local normal vector $\mathbf{n}$ of each level-set curve are:

$$\frac{1}{\bar{r}} = -\nabla \cdot \left(\frac{\nabla \phi}{|\nabla \phi|} \right) = -\frac{\nabla^2 \phi}{|\nabla \phi|} + \frac{1}{|\nabla \phi|^2} \nabla \phi \cdot \nabla \left(|\nabla \phi| \right), \tag{2.2.16}$$

---

[1] At least three mesh-points are necessary to fully resolve the interface. Larger number of mesh-points can be required according to the accuracy of the numerical scheme adopted.

$$\mathbf{n} = -\frac{\nabla\phi}{|\nabla\phi|}, \tag{2.2.17}$$

where definitions (2.2.16) and (2.2.17) are valid only if ϕ has the properties of a signed function, namely each of its iso-surfaces is parallel to the others. This property is conserved when advecting ϕ through the Cahn-Hilliard equation (2.2.2). In particular, as proposed by Magaletti *et al.* [73], the interfacial layers are properly conserved if $M \propto \xi^3 U/L$ where U and L are the velocity and length scale of the problem. With this scaling the controlled diffusion in the interfacial layer is fast enough to restore the local modification of the interface profile produced by the convective effects. As a result the profile of ϕ across the interface is always described by Eq. (2.2.8), that has the properties of a signed function. Substituting Eq. (2.2.16) and (2.2.17) into Eq. (2.2.15), the following force is obtained:

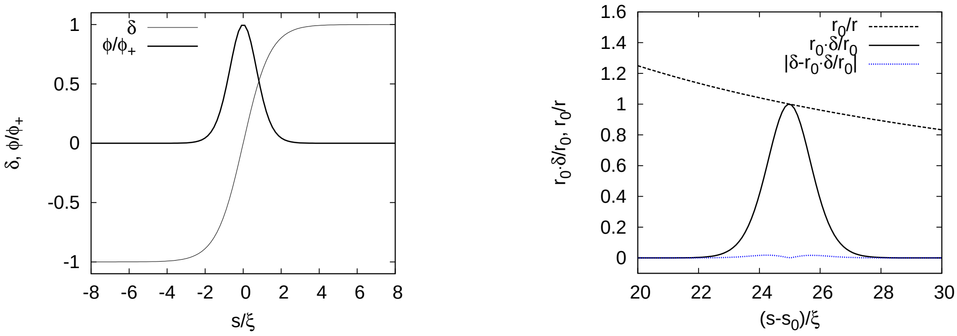

FIGURE 2.3 – Schematic representation of the equilibrium interface profile $\phi(s)$ along the interface normal direction s in comparison with the δ-function $\delta(s)$ (left panel). On the right panel the $\delta/\bar{r}$ term of Eq. (2.2.22) is proposed and normalized by the theoretical curvature radius r_0. The modulus of the difference between the theoretical curvature and $\delta/\bar{r}$ is also proposed.

$$\mathbf{f}_c = -\frac{\kappa}{\bar{r}}|\nabla\phi|^2\mathbf{n} + \kappa\nabla\phi\cdot\nabla\left(|\nabla\phi|\right)\mathbf{n}. \tag{2.2.18}$$

If the interface is correctly described, the surface tension $\sigma = (\sqrt{8}/3)\kappa\phi_+^2/\xi$ is a constant and, substituting to Eq. (2.2.18) it yields the following:

$$\mathbf{f}_c = -\frac{3}{\sqrt{8}}\frac{|\nabla\phi|^2}{\phi_+^2}\xi\sigma\frac{1}{\bar{r}}\mathbf{n} + \kappa\nabla\phi\cdot\nabla\left(|\nabla\phi|\right)\mathbf{n}. \tag{2.2.19}$$

The following δ-function can be isolated:

$$\frac{3}{\sqrt{8}}\frac{|\nabla\phi|^2}{\phi_+^2}\xi = \delta(\mathbf{x}) \Longrightarrow \int_s \delta(\mathbf{x})\mathrm{d}s = 1, \tag{2.2.20}$$

where the integral is performed along a direction s oriented along the interface normal $\mathbf{n}$ and the integration extrema are, by definition, $\pm\infty$. Integrating in the same way Eq.

(2.2.19), the equivalent surface force applied on a sharp interface is obtained:

$$\int_s \mathbf{f}_c \mathrm{d}s = -\sigma \mathbf{n} \int_s \delta(\mathbf{x}) \frac{1}{\bar{r}} \mathrm{d}s + \int_s \left(\kappa \nabla \phi \cdot \nabla \left(|\nabla \phi|\right) \mathbf{n}\right) \mathrm{d}s, \tag{2.2.21}$$

where the last integral is zero because it is the integral of the product between a symmetric positive function by a antisymmetric function. The resulting force has a formulation that matches exactly the Force Coupling proposed by:

$$\int_s \mathbf{f}_c \mathrm{d}s = -\sigma \mathbf{n} \int_s \delta(\mathbf{x}) \frac{1}{\bar{r}} \mathrm{d}s \simeq -\sigma \frac{1}{\bar{r}_0} \mathbf{n} \tag{2.2.22}$$

The difference between $\int \delta/\bar{r}$ and $1/\bar{r}_0$ is due to the computation of the local curvature that is based on a finite thickness layer rather than on a zero-thickness layer. The error committed with this approach is in any case small when the curvature radius is large with respect to the interface thickness. In Fig. 2.3 the difference between $\int \delta/\bar{r}$ and $1/\bar{r}_0$ for an interface with a curvature radius $r_0/\xi = 25$ is proposed; the resulting difference has a maximum magnitude of 0.1% of r_0. However this inaccuracy affects are in fact negligible, moreover all the other continuous approaches (LS) are affected by this minor inaccuracy. The derivation proposed above has been already shown by Chella *et al.* [19] while, among the other authors, [1] examined the same problem adopting variational approaches.

2.3 Dimensional analysis

In this work, the governing equations (2.2.2), (2.2.6), (2.2.11) and (2.2.12) have been solved on a flat channel geometry, where two infinite parallel walls are deployed at a distance $L_z = 2h$. With reference to Fig. 2.4, the governing equations can be rewritten

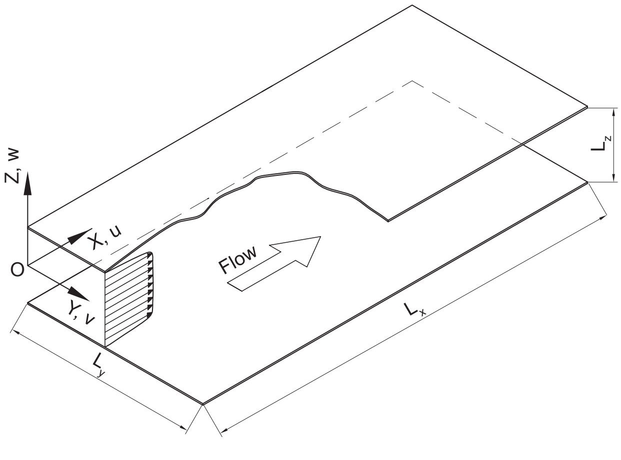

FIGURE 2.4 – Channel geometry

in a non dimensional form by using the following non dimensional variables (denoted by apex "-"):

$$\mathbf{x}^{-} = \frac{\mathbf{x}}{h}, \qquad \mathbf{u}^{-} = \frac{\mathbf{u}}{U_\tau}, \qquad t^{-} = \frac{tU_\tau}{h}, \qquad \tilde{p}^{-} = \frac{\tilde{p}h}{\rho U_\tau^2}, \qquad \phi^{-} = \frac{\phi}{\phi_+} \tag{2.3.1}$$

where h is the channel half height, ϕ_+ is the positive uniform solution of a planar interface (2.2.8) and $U_\tau = \sqrt{\tau_w/\rho}$ is the friction velocity, where τ_w is the shear stress at the channel walls. The non dimensional form of the governing equations reads:

$$\frac{\partial \phi^{-}}{\partial t} = -\mathbf{u}^{-} \cdot \nabla \phi^{-} + \frac{1}{Pe} \nabla^2 \mu^{-}, \tag{2.3.2}$$

$$\mu^{-} = \phi^{-^3} - \phi^{-} - Ch^2 \nabla^2 \phi^{-} = 0. \tag{2.3.3}$$

$$\nabla \cdot \mathbf{u}^{-} = 0, \tag{2.3.4}$$

$$\frac{\partial \mathbf{u}^{-}}{\partial t^{-}} + \mathbf{u}^{-} \cdot \nabla \mathbf{u}^{-} = \frac{1}{Re_\tau} \nabla \cdot \left(\nabla \mathbf{u}^{-} + \nabla \mathbf{u}^{-^T} \right) - \nabla \tilde{p}^{-} + \frac{\sqrt{8}}{3} \frac{1}{We \cdot Ch} \mu^{-} \nabla \phi^{-}. \tag{2.3.5}$$

The following dimensionless groups appear through the non-dimensionalization procedure:

$$Re_\tau = \frac{U_\tau h}{\nu}, \qquad We = \frac{\rho U_\tau^2 h}{\sigma}, \qquad Ch = \frac{\xi}{h}, \qquad Pe = \frac{hU_\tau}{M\beta}. \tag{2.3.6}$$

The friction Reynolds number Re_τ represents the ratio between the inertial forces $U_\tau h$ and the viscous forces ν; the Weber number We is the ratio between inertial forces $\rho U_\tau^2 h$ and the surface tension σ. The Cahn number Ch is the ration between the capillary length ξ and the the channel half height h and it represents the dimensionless capillary length l_ξ^{-}. The Peclet number Pe is the ratio between the diffusive time-scale hU_τ and the convective time-scale $M\beta$ and it controls the interface relaxation time. The Reynolds number can be set considering the flow field and the geometry; once the friction Reynolds number is fixed, the surface tension σ can be imposed through the Weber number. The interface thickness depends, in general, on the problem under analysis and it may assume values ranging several orders of magnitude; this work focuses on the study of immiscible binary mixtures, where the physical interface has a real thickness of $O(Ch^{-9})$). This interface thickness would require numerical resolutions beyond the current computational limits, moreover at that scales the continuum hypotheses breaks down. As a result a fictitious enlargement of the interface is required and the the Cahn number should be set to the minimum value allowed by the numerical scheme adopted, that in general is at least of three mesh points. To overcome this apparent lack of physical meaning and keep the results independent from the interface thickness, a proper scaling between Ch and Pe should be adopted. In the past few years different scaling laws have been proposed based on asymptotic expansion [69, 53, 73]; apparently the best results are obtained imposing $Pe \propto \alpha_s/Ch$, where the effects of the constant α_s are negligible if $O(\alpha_s) = 1$.

2.3.1 The wall units

The results of Part II are reported adopting the so-called “wall-units” (denoted by the superscript “+”), that are defined using the shear velocity U_τ and the cinematic viscosity ν of the fluid. The dimensionless variables are the following:

$$\mathbf{x}^+ = \frac{\mathbf{x}U_\tau}{\nu}, \qquad \mathbf{u}^+ = \frac{u}{U_\tau}, \qquad t^+ = \frac{tU_\tau^2}{\nu}. \tag{2.3.7}$$

Since the phase-field do not depend on the fluid scaling variables, it remains unaltered when described in wall-units: $\phi^- = \phi^+$.

3

Numerical method

In this work the dynamics of large deformable droplets in turbulent multiphase flows is investigated by Direct Numerical Simulation (DNS) of turbulence coupled with the Phase Field Model (PFM) for the interface description. In this chapter, the numerical algorithm adopted for the solution of the governing equations of Chap. 3 is derived and discussed in detail. In the first section, the governing equations are rewritten and the solution algorithm is exposed; in the second section the spectral approximation of the solution is shown and, in the last section, the discretized set of equations is reported.

3.1 Solution algorithm

In this section the dimensionless governing equations (2.3.2)-(2.3.5) are rewritten in a formulation suitable to match the solution algorithm. The momentum and mass balance are rewritten in the so-called "normal-velocity normal-vorticity" formulation; the Cahn-Hilliard equation is rewritten adopting a particular "operator-splitting" technique. A schematic representation of the solution procedure is shown in Fig. 3.1.

3.1.1 Velocity-vorticity formulation

The dimensionless momentum equation (2.3.5)is rewritten as follows (the superscripts have been removed for sake of brevity):

$$\frac{\partial \mathbf{u}}{\partial t} = \mathbf{S} + \frac{1}{Re_\tau}\nabla^2\mathbf{u} - \nabla\tilde{p}', \tag{3.1.1}$$

where the modified pressure term $\tilde{p}$ has been decomposed into its fluctuating and mean components, $\tilde{p} = \tilde{p}' + \tilde{\Pi}$. The mean pressure gradient $\nabla\tilde{\Pi}$, the non-linear convective terms and the source terms have been collected in to the $\mathbf{S}$ term:

$$\mathbf{S} = -\mathbf{u}\cdot\nabla\mathbf{u} - \nabla\tilde{\Pi} + \frac{3}{\sqrt{8}}\frac{1}{We\cdot Ch}\mu\nabla\phi. \tag{3.1.2}$$

To solve the equation system (2.3.4)-(2.3.5) the fluctuating pressure term $\nabla\tilde{p}'$ is removed by taking the curl of eq. (3.1.2), as result the transport equation for the vorticity $\boldsymbol{\omega}$ is obtained:

$$\frac{\partial \boldsymbol{\omega}}{\partial t} = \nabla \times \mathbf{S} + \frac{1}{Re_\tau}\nabla^2 \boldsymbol{\omega}, \tag{3.1.3}$$

where the identity $\nabla \times \nabla \tilde{p}' = 0$ has been substituted. Taking twice the curl of Eq. (3.1.2), substituting the continuity Eq. (2.3.4) and the identity $\nabla \times \nabla \times \mathbf{c} = \nabla(\nabla \cdot \mathbf{c}) - \nabla^2 \mathbf{c}$, the following 4^{th}-order equation for the velocity $\mathbf{u}$ is obtained:

$$\frac{\partial \nabla^2 \mathbf{u}}{\partial t} = \nabla^2 \mathbf{S} - \nabla(\nabla \cdot \mathbf{S}) + \frac{1}{Re_\tau}\nabla^4 \mathbf{u} \tag{3.1.4}$$

Equations (3.1.3)-(3.1.4) are solved for the wall-normal components of the vorticity ω_z and velocity w, adopting the "velocity - vorticity" algorithm developed by Kim *et al.* [54]; rewriting Eq. (3.1.3)-(3.1.4) for ω_z and w, respectively, the following are obtained:

$$\frac{\partial \omega_z}{\partial t} = \frac{\partial S_y}{\partial x} - \frac{\partial S_x}{\partial y} + \frac{1}{Re_\tau}\nabla^2 \omega_z, \tag{3.1.5}$$

$$\frac{\partial (\nabla^2 w)}{\partial t} = \nabla^2 S_z - \frac{\partial}{\partial z}\left(\frac{\partial S_x}{\partial x} + \frac{\partial S_y}{\partial y} + \frac{\partial S_z}{\partial z}\right) + \frac{1}{Re_\tau}\nabla^4 w. \tag{3.1.6}$$

With a suitable set of boundary conditions, ω_z and w are computed and then the stream-wise velocity component u and the span-wise velocity component v are obtained from the continuity equation ad the vorticity definition:

$$\frac{\partial w}{\partial z} = -\frac{\partial u}{\partial x} - \frac{\partial v}{\partial y}, \tag{3.1.7}$$

$$\omega_z = \frac{\partial v}{\partial x} + \frac{\partial u}{\partial y}. \tag{3.1.8}$$

Once the velocity field is fully resolved, the fluctuating pressure $\tilde{p}'$ can be obtained by solving a Poisson-type equation:

$$\nabla^2 \tilde{p}' = \nabla \cdot \mathbf{S}. \tag{3.1.9}$$

3.1.2 Cahn-Hilliard equation splitting

The solution of the Cahn-Hilliard equation requires robust numerical schemes due to the high order operators that it involves; expanding Eq. (2.3.2), a 4^{th}-order operator is highlighted:

$$\frac{\partial \phi}{\partial t} = -\mathbf{u} \cdot \nabla \phi + \frac{1}{Pe}\left(\nabla^2 \phi^3 - \nabla^2 \phi - Ch^2 \nabla^4 \phi\right). \tag{3.1.10}$$

To reduce the stability requirements and adopt the same pseudo-spectral solution involved for the momentum equations, Eq. (3.1.10) is rewritten in the following way:

$$\frac{\partial \phi}{\partial t} = S_\phi + \frac{s}{Pe}\nabla^2 \phi - \frac{Ch^2}{Pe}\nabla^4 \phi, \tag{3.1.11}$$

The operator splitting $\nabla^2\phi = s\nabla^2\phi - (s+1)\nabla^2\phi$ is similar to that adopted by Yue *et al.* [139] and is obtained through a positive coefficient s that is chosen considering the temporal discretization; similar procedures can be found in [5, 62]. The convective term, the non-linear term and the terms rising from the operator splitting are collected in the S_ϕ term:

$$S_\phi = -\mathbf{u}\cdot\nabla\phi + \frac{1}{Pe}\nabla^2\phi^3 - \frac{(s+1)}{Pe}\nabla^2\phi. \tag{3.1.12}$$

3.2 Spectral approximation

Equations (3.1.5), (3.1.6) and (3.1.12) are solved adopting a pseudo-spectral spatial discretization: solutions are approximated by Fourier transforms along the two periodic directions of the channel geometry x and y, respectively; Chebyshev polynomials are adopted to approximate the solution along the wall-normal direction. In order to avoid convolutions in the Fourier-Chebishev space, the multiplication of spectral variables (i.e. convective terms) is obtained transforming back the variables to the physical space, taking the multiplications and the re-transforming to the Fourier-Chebyshev space. For this reason these class of algorithms is also known as “pseudo-spectral algorithms”. A signal g, projected in to the Fourier space along the periodic directions x and y, can be represented by the following sum of harmonics:

$$g(x,y,z) = \sum_{n_x=-\frac{N_x}{2}+1}^{\frac{1}{2}N_x}\ \sum_{n_y=-\frac{N_y}{2}+1}^{\frac{1}{2}N_y} \hat{g}(k_x,k_y,z)e^{j(k_x x + k_y y)}, \tag{3.2.1}$$

where $j=\sqrt{-1}$ is the imaginary unit of the complex representation, $\hat{g}$ is the Fourier coefficient of the signal in the modal coordinates (k_x, k_y); at this point dependence on the physical coordinate z is still present. The two periodic directions are treated with a Fast Fourier Transform (FFT) algorithm imposing periodicity lengths of L_x and L_y and projecting the velocity vector on to N_x and N_y Fourier modes in the x and y directions of the geometry of Fig. 2.4. Through the Fourier transform, the variables are mapped an a uniform grid in the physical space and the nodes spacing is:

$$\Delta x = \frac{L_x}{N_x - 1}, \qquad \Delta_y = \frac{L_y}{N_y - 1}. \tag{3.2.2}$$

The signal is decomposed in a sum of periodical functions characterized by wavenumber and amplitude; the former represents the frequency of the corresponding harmonic, whereas the latter is the magnitude of the harmonic. Each mode n_x or n_y is characterized by the following wave-numbers:

$$k_x = \frac{2\pi n_x}{L_x}, \qquad k_y = \frac{2\pi n_y}{L_y}. \tag{3.2.3}$$

Since the Fourier basis is orthogonal, the Fourier transform $\hat{g}$ can be obtained as follows:

$$\hat{g}(k_x, k_y, z) = \frac{1}{N_x N_y} \sum_{n_x=-\frac{N_x}{2}+1}^{\frac{1}{2}N_x} \sum_{n_y=-\frac{N_y}{2}+1}^{\frac{1}{2}N_y} g(x, y, z) e^{-j(k_x x + k_y y)}. \tag{3.2.4}$$

Along the wall normal direction z, the transformed signal $\hat{g}(k_x, k_y, z)$ is approximated through the sum of Chebyshev polynoms $T_n(z)$:

$$\hat{g}(k_x, k_y, z) = \sum_{n_z=0}^{N_z'} h(k_x, k_y, n_z) T_n(z), \tag{3.2.5}$$

where the prime indicate the first term halving. The Chebyshev polynomial of order n_z in z is defined as follows:

$$T_{nz}(z) = \cos\left[n_z \arccos(z)\right], \tag{3.2.6}$$

where n_z is one of the N_z Chebyshev modes and $-1 \leq z \leq 1$. The orthogonality property holds also for the Chebyshev polynomials and the inverse transform is:

$$\hat{h}(k_x, k_y, n_z) = \frac{2}{N_z} \sum_{n_z=0}^{N_z'} \hat{g}(k_x, k_y, z) T_n(z). \tag{3.2.7}$$

The variables described in the Chebishev space are mapped in the physical space according to the following mapping:

$$z = \cos\left(\frac{n_z \pi}{N_z}\right). \tag{3.2.8}$$

With adoption of Chebychev polynomials for the approximation of the solution along the wall-normal direction, the spatial discretization is characterized by a large resolution near the walls ($z = \pm 1$), where large velocity gradients need to be resolved. A complete review of the method can be find in Boyd [12] Concluding, adopting the transformations of Eq. (3.2.1) and Eq. (3.2.5), the spectral representation of a three-dimensional signal is the following:

$$g(x, y, z, t) = \sum_{n_x=-\frac{N_x}{2}+1}^{\frac{1}{2}N_x} \sum_{n_y=-\frac{N_y}{2}+1}^{\frac{1}{2}N_y} \sum_{n_z=0}^{N_z'} \hat{h}(k_x, k_y, n_z, t) T_{n,z}(z) e^{j(k_x x + k_y y)}. \tag{3.2.9}$$

Due to the presence of products taken in to the physical space, the computational algorithm needs the introduction of de-aliasing procedures also in the Chebyshev transforms; following Boyd [12] a the “2/3 rule” is applied, keeping only the first two thirds of the modes after the application of the pseudo-spectral multiplications.

3.3 Discretization and solution of the equations

3.3.1 Velocity equation

Using the spectral representation of Sect. 3.2, Eq. (3.1.6) reads:

$$\begin{aligned}\frac{\partial}{\partial t}\left(\frac{\partial^2}{\partial z^2}-k_{xy}^2\right)\hat{w} &= \left(\frac{\partial^2}{\partial z^2}-k_{xy}^2\right)\hat{S}_z \\ &- \frac{\partial}{\partial z}\left(ik_x\hat{S}_x+ik_y\hat{S}_y+\frac{\partial}{\partial z}\hat{S}_z\right) \\ &+ \frac{1}{Re_\tau}\left(\frac{\partial^2}{\partial z^2}-k_{xy}^2\right)\left(\frac{\partial^2}{\partial z^2}-k_{xy}^2\right)\hat{w},\end{aligned} \tag{3.3.1}$$

where $k_{xy}^2 = k_x^2 + k_y^2$. The equation above stresses that the z derivatives are taken in a different way, due to the adoption of Chebyshev polynomials. Eq. (3.3.1) is discretized in time adopting an hybrid IMplicit EXplicit (IMEX) scheme: (i) a second-order Adams-Bashfort explicit scheme is adopted for the non-linear convective terms; (ii) the implicit Crank-Nicholson implicit scheme is applied to the diffusive operators. The time-discretized form of Eq. (3.3.1) reads:

$$\begin{aligned}\frac{\hat{w}^{n+1}-\hat{w}^n}{\Delta t}\left(\frac{\partial^2}{\partial z^2}-k_{xy}^2\right)\hat{w} &= \frac{3}{2}\left(\frac{\partial^2}{\partial z^2}-k_{xy}^2\right)\hat{S}_z^n \\ &- \frac{1}{2}\left(\frac{\partial^2}{\partial z^2}-k_{xy}^2\right)\hat{S}_z^{n-1} \\ &- \frac{3}{2}\frac{\partial}{\partial z}\left(ik_x\hat{S}_x^n+ik_y\hat{S}_y^n+\frac{\partial}{\partial z}\hat{S}_z^n\right) \\ &+ \frac{1}{2}\frac{\partial}{\partial z}\left(ik_x\hat{S}_x^{n-1}+ik_y\hat{S}_y^{n-1}+\frac{\partial}{\partial z}\hat{S}_z^{n-1}\right) \\ &+ \frac{1}{Re_\tau}\left(\frac{\partial^2}{\partial z^2}-k_{xy}^2\right)\left(\frac{\partial^2}{\partial z^2}-k_{xy}^2\right)\frac{\hat{w}^{n+1}-\hat{w}^n}{2},\end{aligned} \tag{3.3.2}$$

where superscripts $n-1$, n, $n+1$ indicate the three consecutive time levels $t-\Delta t$, t and $t+\Delta t$, respectively and Δt is the time-step. Eq. (3.3.2) is rearranged and, introducing the coefficient $\gamma = \Delta t/2Re$, the following is obtained:

$$\begin{aligned}\left[1-\gamma\left(\frac{\partial^2}{\partial z^2}-k_{xy}^2\right)\right]\left(\frac{\partial^2}{\partial z^2}-k_{xy}^2\right)\hat{w}^{n+1} &= \frac{3\Delta t}{2}\left(\frac{\partial^2}{\partial z^2}-k_{xy}^2\right)\hat{S}_z^n \\ &- \frac{\Delta t}{2}\left(\frac{\partial^2}{\partial z^2}-k_{xy}^2\right)\hat{S}_z^{n-1} \\ &- \frac{3\Delta t}{2}\frac{\partial}{\partial z}\left(ik_x\hat{S}_x^n+ik_y\hat{S}_y^n+\frac{\partial}{\partial z}\hat{S}_z^n\right) \\ &+ \frac{\Delta t}{2}\frac{\partial}{\partial z}\left(ik_x\hat{S}_x^{n-1}+ik_y\hat{S}_y^{n-1}+\frac{\partial}{\partial z}\hat{S}_z^{n-1}\right)\end{aligned} \tag{3.3.3}$$

$$+ \quad \left[\gamma \frac{\partial^2}{\partial z^2} + \left(1 - k_{xy}^2\right)\right] \left(\frac{\partial^2}{\partial z^2} - k_{xy}^2\right) \hat{w}^n.$$

The discretized continuity Eq. (3.1.7) is:

$$ik_x \hat{u} + ik_y \hat{v} + \frac{\partial w}{\partial z} = 0, \tag{3.3.4}$$

substituting Eq. (3.3.4) into Eq. (3.3.3) and introducing the coefficient $\lambda^2 = (1+\gamma k_{xy}^2)/\gamma$, the following is obtained:

$$\begin{aligned} - \quad & \gamma \left(\frac{\partial^2}{\partial z^2} - \lambda^2\right) \left(\frac{\partial^2}{\partial z^2} - k_{xy}^2\right) \hat{w}^{n+1} = \\ - \quad & k_{xy}^2 \left(\frac{3}{2}\hat{S}_z^n - \frac{1}{2}\hat{S}_z^{n-1}\right) \Delta t - k_{xy}^2 \left[\gamma \frac{\partial^2}{\partial z^2} + \left(1 - \gamma k_{xy}^2\right)\right] \hat{w}^n \\ - \quad & \frac{\partial}{\partial z} ik_x \left(\frac{3}{2}\hat{S}_x^n - \frac{1}{2}\hat{S}_x^{n-1}\right) \Delta t - \frac{\partial}{\partial z} ik_x \left(\gamma \frac{\partial^2}{\partial z^2} + \left(1 - \gamma k_{xy}^2\right)\right) \hat{u}^n \\ - \quad & \frac{\partial}{\partial z} ik_y \left(\frac{3}{2}\hat{S}_y^n - \frac{1}{2}\hat{S}_y^{n-1}\right) \Delta t - \frac{\partial}{\partial z} ik_y \left(\gamma \frac{\partial^2}{\partial z^2} + \left(1 - \gamma k_{xy}^2\right)\right) \hat{v}^n. \end{aligned} \tag{3.3.5}$$

The historical terms $\hat{H}_x^n$, $\hat{H}_y^n$ and $\hat{H}_z^n$ are defined as follows:

$$\begin{aligned} \hat{H}_x^n &= \left(\frac{3}{2}\hat{S}_x^n - \frac{1}{2}\hat{S}_x^{n-1}\right) \Delta t + \left[\gamma \frac{\partial^2}{\partial z^2} + \left(1 - \gamma k_{xy}^2\right)\right] \hat{u}^n \\ \hat{H}_y^n &= \left(\frac{3}{2}\hat{S}_y^n - \frac{1}{2}\hat{S}_y^{n-1}\right) \Delta t + \left[\gamma \frac{\partial^2}{\partial z^2} + \left(1 - \gamma k_{xy}^2\right)\right] \hat{v}^n \\ \hat{H}_z^n &= \left(\frac{3}{2}\hat{S}_z^n - \frac{1}{2}\hat{S}_z^{n-1}\right) \Delta t + \left[\gamma \frac{\partial^2}{\partial z^2} + \left(1 - \gamma k_{xy}^2\right)\right] \hat{w}^n, \end{aligned} \tag{3.3.6}$$

introducing Eq. (3.3.6), Eq. (3.3.5) reads:

$$\left(\frac{\partial^2}{\partial z^2} - \lambda^2\right) \left(\frac{\partial^2}{\partial z^2} - k_{xy}^2\right) \hat{w}^{n+1} = \frac{1}{\gamma} \left[k_{xy}^2 \hat{H}_z^n + \frac{\partial}{\partial z} \left(ik_x \hat{H}_x^n + ik_y \hat{H}_y^n\right)\right]. \tag{3.3.7}$$

Collecting $\hat{H}^n = k_{xy}^2 \hat{H}_z^n + \frac{\partial}{\partial z}(ik_x \hat{H}_x^n + ik_y \hat{H}_y^n)$, the final form of the discretized Eq. (3.1.8) is obtained:

$$\left(\frac{\partial^2}{\partial z^2} - \lambda^2\right) \left(\frac{\partial^2}{\partial z^2} - k_{xy}^2\right) \hat{w}^{n+1} = \frac{\hat{H}^n}{\gamma}. \tag{3.3.8}$$

Introducing the auxiliary variable $\hat{\theta} = \left(\frac{\partial^2}{\partial z^2} - k_{xy}^2\right)$ the 4^{th}-order equation can be split in two 2^{nd}-order equations:

$$\left(\frac{\partial^2}{\partial z^2} - \lambda^2\right) \hat{\theta} = \frac{\hat{H}^n}{\gamma}, \tag{3.3.9}$$

$$\left(\frac{\partial^2}{\partial z^2} - k_{xy}^2\right)\hat{w}^{n+1} = \hat{\theta}. \tag{3.3.10}$$

Eq. (3.3.10) is solved imposing the following boundary conditions:

$$\hat{w}^{n+1}(\pm 1) = 0, \qquad \frac{\partial \hat{w}^{n+1}}{\partial z}(\pm 1) = 0, \tag{3.3.11}$$

which are obtained from the non-slip condition at the wall and from the continuity equation coupled with the non-slip condition at the wall. The solution of Eq. (3.3.10) requires a set of boundary conditions on $\hat{\theta}$ that lack in the physical model definition. To circumvent this problem, $\hat{\theta}$ is rewritten as follows:

$$\hat{\theta} = \hat{\theta}_1 + \hat{A}\theta_2 + \hat{B}\theta_3, \tag{3.3.12}$$

where $\hat{A}$ and $\hat{B}$ are complex constants to be determined. The three components, $\hat{\theta}_1$, θ_2 and θ_3 are the particular solution and two homogeneous solution of Eq. (3.3.9), respectively. Their solution is obtained as follows:

$$\left(\frac{\partial^2}{\partial z^2} - \lambda^2\right)\hat{\theta}_1 = \frac{\hat{H}^n}{\gamma}, \qquad \hat{\theta}_1(1) = 0, \qquad \hat{\theta}_1(-1) = 0, \tag{3.3.13}$$

$$\left(\frac{\partial^2}{\partial z^2} - \lambda^2\right)\theta_2 = 0, \qquad \theta_2(1) = 0, \qquad \theta_2(-1) = 1, \tag{3.3.14}$$

$$\left(\frac{\partial^2}{\partial z^2} - \lambda^2\right)\theta_3 = 0, \qquad \theta_3(1) = 1, \qquad \theta_3(-1) = 0. \tag{3.3.15}$$

In a similar way, also $\hat{w}$ is rewritten as a sum of a particular solution $\hat{w}_1$ and two homogeneous solutions w_2, w_3:

$$\hat{w}^{n+1} = \hat{w}_1 + \hat{A}w_2 + \hat{B}w_3. \tag{3.3.16}$$

Similarly to the solution of $\hat{\theta}$, the solutions for $\hat{w}_1$, w_2 and w_3 can be obtained applying the no-slip BC:

$$\left(\frac{\partial^2}{\partial z^2} - k_{xy}^2\right)\hat{w}_1 = \hat{\theta}, \qquad \hat{w}_1(1) = 0, \qquad \hat{w}_1(-1) = 0, \tag{3.3.17}$$

$$\left(\frac{\partial^2}{\partial z^2} - k_{xy}^2\right)w_2 = 0, \qquad w_2(1) = 0, \qquad w_2(-1) = 0, \tag{3.3.18}$$

$$\left(\frac{\partial^2}{\partial z^2} - k_{xy}^2\right)w_3 = 0, \qquad w_3(1) = 0, \qquad w_3(-1) = 0. \tag{3.3.19}$$

The unknown constants $\hat{A}$ and $\hat{B}$ are determined applying the $\partial\hat{w}/\partial z = 0$ BC:

$$\frac{\partial \hat{w}_1}{\partial z}(1) + \hat{A}\frac{\partial w_2}{\partial z}(1) + \hat{B}\frac{\partial w_3}{\partial z}(1) = 0 \tag{3.3.20}$$

$$\frac{\partial \hat{w}_1}{\partial z}(-1) + \hat{A}\frac{\partial w_2}{\partial z}(-1) + \hat{B}\frac{\partial w_3}{\partial z}(-1) = 0.$$

From Eq. (3.3.16), $\hat{w}^{n+1}$ is obtained. The solutions of equations (3.3.13)-(3.3.15) and (3.3.17)-(3.3.19) are obtained adopting the Chebysev-Tau solution algorithm proposed in [54] and the resulting tridiagonal equations system is solved adopting the Gauss elimination procedure.

3.3.2 Vorticity equation

The wall-normal vorticity component $\hat{\omega}_z$ is obtained solving Eq. (3.1.5); following the discretization described in Sect. 3.3.1, Eq. (3.1.5) reads:

$$\left(\frac{\partial^2}{\partial z^2} - \lambda^2\right)\hat{\omega}_z^{n+1} = -\frac{1}{\gamma}\left[ik_x\hat{H}_y^n - ik_y\hat{H}_x^n\right]. \tag{3.3.21}$$

The solution of Eq. (3.3.21) is obtained adopting the Chebyshev-Tau algorithm with the following BC:

$$\hat{\omega}_z^{n+1}(\pm 1) = ik_x\hat{v}^{n+1} - ik_y\hat{u}^{n+1} = 0. \tag{3.3.22}$$

The resulting tridiagonal equations system is then solved adopting a Gauss elimination technique. Once the wall-normal vorticity component $\hat{\omega}_z$ is known, the other two velocity components $\hat{u}^{n+1}$ and $\hat{v}^{n+1}$ can be derived from the spectral representation of the vorticity definition and the spectral representation of the continuity equation:

$$-ik_y\hat{u}^{n+1} + ik_x\hat{v}^{n+1} = \hat{\omega}_z^{n+1}, \tag{3.3.23}$$

$$-ik_x\hat{u}^{n+1} + ik_y\hat{v}^{n+1} = \frac{\partial \hat{w}^{n+1}}{\partial z}. \tag{3.3.24}$$

3.3.3 Cahn-Hilliard equation

Eq. (3.1.11) is discretized in space adopting the spectral representation shown in Sect. 3.2 and applied in Sect. 3.3.1 and Sect. 3.3.2:

$$\begin{aligned}\frac{\partial \hat{\phi}}{\partial t} &= \hat{S}_\phi + \frac{s}{Pe}\left(\frac{\partial^2}{\partial z^2} - k_{xy}^2\right)\hat{\phi} \qquad (3.3.25)\\ &- \frac{Ch^2}{Pe}\left(\frac{\partial^2}{\partial z^2} - k_{xy}^2\right)\left(\frac{\partial^2}{\partial z^2} - k_{xy}^2\right)\hat{\phi},\end{aligned}$$

The Cahn-Hilliard equation solutions are characterized by a the presence of high frequency harmonics, that need to be damped in order to keep the solution bounded. The adoption of weakly damping schemes, such as the Crank-Nicholson adopted for the velocity field equations in Sect. 3.3.1 leads to aliased solutions [3]. For this reason, following [139], a 1^{th}-order Backward Difference Formula (BDF) is adopted. In particular the non linear convective S_ϕ term is discretized adopting a 2^{nd} order Adams-Bashfort:

$$\frac{\hat{\phi}^{n+1} - \hat{\phi}^n}{\Delta t} = \frac{3}{2}\hat{S}_\phi^n - \frac{1}{2}\hat{S}_\phi^{n-1} + \frac{s}{Pe}\left(\frac{\partial^2}{\partial z^2} - k_{xy}^2\right)\hat{\phi}^{n+1} \tag{3.3.26}$$

$$- \quad \frac{Ch^2}{Pe}\left(\frac{\partial^2}{\partial z^2} - k_{xy}^2\right)\left(\frac{\partial^2}{\partial z^2} - k_{xy}^2\right)\hat{\phi}^{n+1}.$$

Introducing the coefficient $\gamma_\phi = (\Delta t Ch^2)/Pe$, Eq. (3.3.26) yields:

$$\left[\frac{1}{\gamma_\phi} - \frac{s}{Ch^2}\left(\frac{\partial^2}{\partial z^2} - k_{xy}^2\right) + \left(\frac{\partial^2}{\partial z^2} - k_{xy}^2\right)^2\right]\hat{\phi}^{n+1} = \frac{\hat{H}_\phi}{\gamma_\phi}, \tag{3.3.27}$$

where the historical term $\hat{H}_\phi$ has been introduced:

$$\frac{\hat{H}_\phi}{\gamma_\phi} = \frac{1}{\gamma_\phi}\left(\hat{\phi}^n + \frac{3\Delta t}{2}\hat{S}_\phi^n - \frac{\Delta t}{2}\hat{S}_\phi^{n-1}\right). \tag{3.3.28}$$

Defining the auxiliary variable $\theta_\phi = \lambda_\phi \phi + \nabla^2\phi$, the 4^{th}-order Eq. (3.3.27) can be split in two 2^{nd} order equations:

$$\left(\frac{\partial^2}{\partial z^2} - k_{xy}^2 - \lambda_\phi - s\right)\hat{\theta}_\phi = \frac{\hat{H}_\phi}{\gamma_\phi}, \tag{3.3.29}$$

$$\left(\frac{\partial^2}{\partial z^2} - k_{xy}^2 - \lambda_\phi\right)\hat{\phi}^{n+1} = \hat{\theta}_\phi. \tag{3.3.30}$$

In order to recovery Eq. (3.3.25), the coefficients λ_ϕ yields to the following:

$$\lambda_\phi = \frac{s}{2Ch^2}\left(-1 - \sqrt{1 - \frac{4Ch^4}{\gamma_\phi s^2}}\right), \tag{3.3.31}$$

where $s \geq \sqrt{4Pe/\Delta t Ch^2}$. Eq. (3.3.30) is solved imposing the following boundary conditions that emerge imposing a normal contact angle for the interface at the walls:

$$\frac{\partial \hat{\phi}^{n+1}}{\partial z}(\pm 1) = 0, \qquad \frac{\partial^3 \hat{w}^{n+1}}{\partial z^3}(\pm 1) = 0. \tag{3.3.32}$$

The BC on $\hat{\theta}_\phi$ lack prom the physical problem definition, as a result a procedure similar to that adopted to solve Eq. (3.3.9) is employed. Eq. (3.3.29) and Eq. (3.3.30) are solved through a Chebyshev-Tau algorithm and the resulting tridiagonal linear system is solved by Gauss elimination.

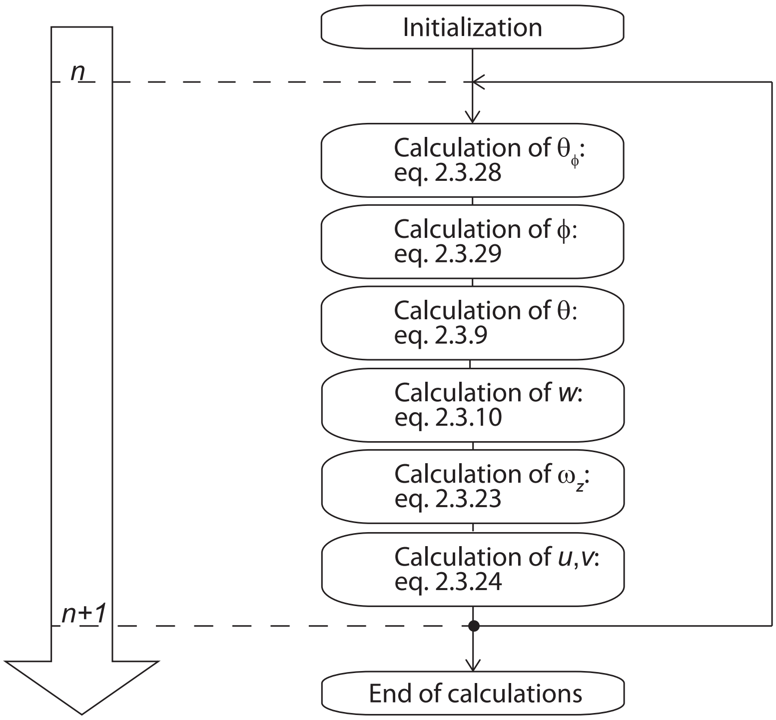

Figure 3.1 – Flux diagram of the phase field-flow field solution algorithm

4

Numerical model validation

Reproduced in part from:

L. Scarbolo, D. Molin, P. Perlekar, M. Sbragaglia, A. Soldati and F. Toschi, “Unified framework for a side-by-side comparison of different multicomponent algorithms: Lattice Boltzmann vs. phase field model”, J. Comp. Phys. 234 (2013).

In this chapter the numerical method proposed in Chap. 3 is validated against selected benchmarks; in the first section the problem of a single droplet deformed under shear flow is solved and the results are compared to the available analytical solution. In the second section the accuracy of the method is discussed in comparison with two widely adopted Lattice Boltzmann multicomponent algorithms.

4.1 Droplet deformation under laminar shear flow

In this section the governing equations of Chap. 2 are applied to the problem of a droplet deformation under laminar shear flow; a schematic of the problem is reported in Fig. 4.1. The analytic solution of the problem was obtained by Taylor [120]: adopting a sharp interface approach he solved the unbounded creeping flow equations in the limit of vanishing droplet deformations. Under these hypothesis, the deformed droplet assumes the shape of a prolate ellipsoid whose major axes is contained in the shear gradient plane and it is tilted according to the velocity profile. After the initial transient, the capillary forces at the interface balance the external shear forcing and the droplet deformation D is proportional to the capillary number Ca:

$$D = \frac{35}{32} Ca. \tag{4.1.1}$$

The deformation parameter $D = (l_a - l_b)/(l_a + l_b)$ is computed measuring the length of the major an minor axis of the ellipsoid in the shear gradient plane, l_a and l_b, respectively. The third axes l_c, normal to the shear gradient plane, remains almost unaltered for small

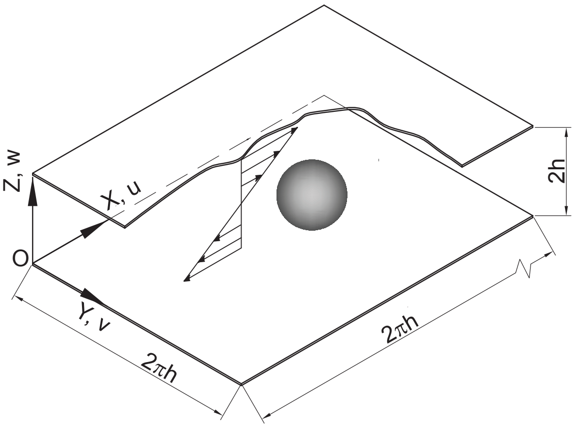

FIGURE 4.1 – Schematics of the problem under analysis: a single deformable droplet under laminar shear flow.

deformations. Eq. (4.1.1) holds for vanishing deformations and matched viscosities[1] yielding to accurate predictions for small deformations, namely $D < 0.3$. The capillary number is defined as follows:

$$Ca = \frac{\dot{\gamma}\nu\rho d}{2\sigma}, \tag{4.1.2}$$

where $\dot{\gamma} = \rho u_w/h$ is the shear rate, d is the undeformed droplet diameter and σ is the surface tension. The extension of the work of Taylor to wall bounded shear flows can be found in [112].

4.1.1 Problem definition

With reference to the schematics of Fig. 4.1, a spherical droplet of diameter d is initialized in the middle of the channel domain of and the initial fluid velocity is set to zero: $\mathbf{u} = 0$. A a stream-free shear flow is applied setting the walls velocity to $u(z = -h) = -u_w$ and $u(z = h) = u_w$, respectively; the other two velocity components are set to zero at the walls: $v(\pm h) = w(\pm h) = 0$. With the numerical framework discussed in Chap. 3, the shear flow condition is obtained setting the following vorticity BCs (3.3.22):

$$\hat{\omega}_z^{n+1}(\pm 1) = \mp i k_y \hat{u}_w^{n+1}. \tag{4.1.3}$$

Adopting the non-dimensional variables of Sect. 2.3, the Capillary number (4.1.2) yields:

$$D = \frac{We}{Re_\tau}\frac{d^-}{2}. \tag{4.1.4}$$

The value of the Reynolds number has been chosen to ensure complete creeping flow conditions: $Re_w = |u_w|h/\nu = 0.2$ and, imposing a dimensionless wall velocity $|u_w^-| = 1$,

---

[1] A more general law, where different viscosities are considered, can be found in [120].

the friction Reynolds number yields to $Re_\tau = 0.2$. A droplet of initial diameter $d^- = 1.0 = h$ has been initialized in the middle of a computational domain of $2\pi h \times 2\pi h \times 2h$ in x, y and z directions, respectively and the grid resolution has been set to $128 \times 128 \times 129$. In order to describe the interface with at least five mesh points, the Cahn number has been set to $Ch = 0.05$ and, adopting the scaling proposed by [73], $Pe = Ch^{-1} = 20$.

4.1.2 Results

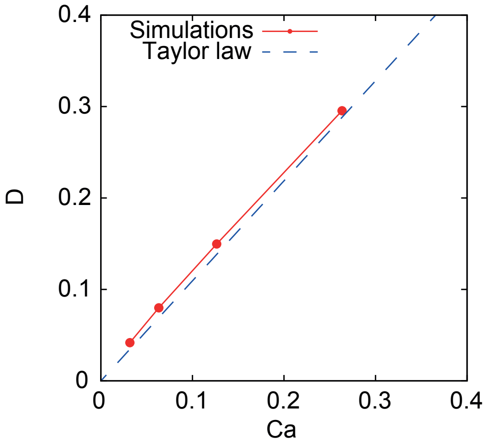

FIGURE 4.2 – Deformation parameter D for different Capillary numbers Ca: Comparison with the analytic Taylor law.

Fig. 4.2 shows the results for four different Capillary numbers Ca; good agreement is observed up to the limit of validity of the Taylor law (4.1.1) $D = 0.3$. Some of the discrepancies that can be observed are probably due to the uncertainties on the exact interface location; due to the diffuse nature of the interface, it location is determined with the iso-surface $\phi = 0$.

4.2 Comparison with multicomponet Lattice Boltzmann models

In this section the PFM proposed in Chap. 2 is modified and solved on selected benchmarks to provide a quantitative comparison with two of the most used multicomponent PFM lattice Boltzmann Models (LBM). Objective of this analysis is the comparison of the peculiar features of the PFM with the features of other widely adopted methods, focusing in particular on the accuracy of the capillary forces modelling and on the local mass conservation.

4.2.1 Introduction to multicomponent LBM

In this section the stochastic LBM for multicomponent fluid modelling is briefly proposed; a detailed discussion on this approach can be found in the literature [35, 116, 38, 39, 117, 145, 34]. Many of the kinetic models developed for the study of mixtures are based on the linearised Boltzmann equations, especially the single-relaxation-time model due to Bhatnagar, Gross, and Krook [11], also named BGK-model:

$$\begin{aligned}\frac{\partial g(\mathbf{x},\mathbf{u},t)}{\partial t} + \mathbf{u}\cdot\nabla g(\mathbf{x},\mathbf{u},t) + \mathbf{a}\cdot\nabla_{\mathbf{u}} g(\mathbf{x},\mathbf{u},t) = \Omega(\mathbf{x},t) = \\ = -\frac{1}{\tau_g}\left[g(\mathbf{x},\mathbf{u},t) - g^{(eq)}(\mathbf{x},\mathbf{u},t)\right],\end{aligned} \tag{4.2.1}$$

where $g(\mathbf{x},\mathbf{u},t)$ is the probability density function to find at the space-time location $(\mathbf{x},t)$ a particle with velocity $\mathbf{u}$. The collisional kernel, on the right hand side of Equation (4.2.1), stands for the relaxation (with a characteristic relaxation time τ_g) towards the local equilibrium $g^{(eq)}(\mathbf{x},\mathbf{u},t)$ which, in turn, depends on the local macroscopic variables, as density and momentum:

$$\rho(\mathbf{x},t) = \int g(\mathbf{x},\mathbf{u},t)\mathrm{d}\mathbf{u} \qquad \rho\mathbf{u}(\mathbf{x},t) = \int \left(g(\mathbf{x},\mathbf{u},t)\mathbf{u}\right)\mathrm{d}\mathbf{u}. \tag{4.2.2}$$

$\mathbf{a}\cdot\nabla_{\mathbf{u}} g(\mathbf{x},\mathbf{u},t)$ represents the effect of a volume/body force density, $\mathbf{a}$, on the kinetic dynamics. Modern discrete-velocity counterparts of (4.2.1), the so-called Lattice Boltzmann methods (LBM), are able to simulate multiphase and multicomponent fluids and have attracted considerable attention from the scientific community [71, 72, 106–109, 119, 13, 14, 104]. The LBM is an discrete form of Boltzmann kinetic equation describing the dynamics of a fictitious ensemble of particles [10, 135, 118, 20], whose motion and interactions are confined to a regular space-time lattice. This approach consists in the following evolution:

$$g_i(\mathbf{x}+\mathbf{c}_i\Delta t, t+\Delta t) - g_i(\mathbf{x},t) = -\frac{\Delta t}{\tau_g}[g_i(\mathbf{x},t) - g_i^{(eq)}(\mathbf{x},t)], \tag{4.2.3}$$

where $g_i(\mathbf{x},t)$ is the probability density function of finding a particle at site $\mathbf{x}$ and time t, moving in the direction of the i-th lattice speed $\mathbf{c}_i$ with $i = 0,\ldots,b$. Systematic ways to derive the discrete set of velocities in these models are either the discretization of the Boltzmann equation on the roots of Hermite polynomials [111, 88, 114, 110, 74, 77, 83] or the construction of high-order lattices for more stable LBM based on entropic approaches [22, 21]. At the same time, the translation of the body/volume force $\mathbf{a}\cdot\nabla_{\mathbf{u}} g(\mathbf{x},\mathbf{u},t)$ onto the discrete-lattice framework represented one of the most challenging issues in the last years of Lattice Boltzmann research [106–109, 119, 13, 14, 40, 74, 41, 138, 58]. Through one of the first approaches proposed in the literature, the so called Shan-Chen (SC) approach [106, 107], the non-ideal interactions have been introduced directly at the discrete lattice level among the constituent (kinetic) particles [106, 107, 103]. These lattice forces embed the essential features and are able to produce phase separation (i.e. a non-ideal equation of state and a non-zero surface tension) as well as a detailed diffuse interface structure. The application of the SC models has been particularly fruitful for many applications [47, 58, 144, 7, 97, 9]. Despite that, its theoretical foundations have been object of debate in the recent years [40, 103, 7, 97], mainly because of the thermodynamic consistency of the mesoscopic interactions involved. However, in the so called Free-Energy (FE) models [119, 13, 14], the collisional properties of the model have been chosen in such a way that the large scale equilibrium is consistent with an underlying free energy functional, embedding both hard core effects and weak interacting tails. In this case, more traceable theoretical foundations have been provided, at least from the point of view of a continuum theory [132]. Among others, some studies have also performed where more elaborated lattice models, including the effect of an exclusion volume based on Enskog theory [40, 41, 74], effective equilibria [144], or even effective SC forces, were designed to match the desired bulk pressure of a given fluid [138, 58].

4.2.2 Advantages and disadvantages of the methods

Multicomponent LBM and PFM have demonstrated excellent performances to predict the dynamics of multiphase and multicomponent flows. Yet, both methods show their own peculiar characteristics and drawbacks which can limit their use, performances and range of validity. A particular unexpected, and unwanted, feature of multiphase and multicomponent solvers is the manifestation of non physical velocities near equilibrium interface, present even for systems at rest. From a physical viewpoint the velocity should clearly vanish at equilibrium but, as it has been observed by many authors, small spurious currents most often exist in the proximity of the interfaces. In an attempt to remove these unwanted features several improvement to the LBM have been proposed in recent years [37, 23, 131, 67, 103, 98]. It worth noticing that some of these improvement are capable to remove these spurious current to machine precision [67]. Spurious currents have also been observed in other numerical methods including the PFM [49, 94, 101]. Because of the magnitude of these spurious current drastically depend on the actual variant of the LBM or PFM, the comparison between the two methods may be somewhat ill defined. Here we aim at comparing the LBM vs. the PFM for their most widespread and used variants. Our answer will thus not provide a general statement valid for the two methods as such, but will still provide some extremely useful insight in what can be expected from the most employed variations of the approaches. As a side results, we will also quantitatively compare two of the most widely used lattice Boltzmann variants, the SC-LBM and the FE-LBM, under the same conditions (i.e. same diffuse interface model, same surface tension, same chemical potential, etc.). In order to achieve our goal, the problem of a one-to-one matching of the PFM with SC/FE multicomponent LBM needs to be addressed first. The one-to-one matching of the two methods gives also the opportunity to clarify how they compare with respect to the computational costs. In order to address these issues we start by analysing the SC model for two population with inter-particle repulsion; the large scale continuum limit is reviewed and formulated in terms of a diffuse interface model with an underlying thermodynamic FE functional. In this way one of the crucial issues in the matching of SC model vs. the corresponding FE model is being solved. Then, starting from the matched SC/FE multicomponent LBM, a new formulation for the free-energy of the PFM is derived in order to directly compare them. Finally, a comparison of the numerical results obtained, on the same problem, from both LBM and PFM is presented, focusing in particular on unwanted spurious currents or mass leakage in sheared suspensions. This work focuses only the case of binary mixtures, even if modelling more than two components is nowadays far from trial extension [2, 4, 105, 55, 84].

4.2.3 Matching the diffuse interface model

In this section the free energy (2.2.4) of the PFM for a multicomponent fluid system discussed in Chap. 2 is rewritten to match the LBM models here adopted. According to Scarbolo *et al.* [99], the free energy functional f_0 necessary to describe the system and match the LBM models features, gives the following τ_g-dependent chemical potential $\mu^{(\tau_g)}(\phi)$:

$$\mu^{(\tau_g)}(\phi) = \frac{c_S^2}{2} \log\left(\frac{\rho+\phi}{\rho-\phi}\right) - \frac{g_{AB}^{(\tau_g)}}{2} c_S^2 \phi - \frac{g_{AB}^{(\tau_g)}}{4} c_S^4 \nabla^2 \phi, \tag{4.2.4}$$

where the surface tension parameter is $\kappa = g_{AB}^{(\tau_g)} c_S^4/4$ and the coupling coefficient is $g_{AB}^{(\tau_g)} = (\tau_g g_{AB})/(\tau_g - 1/2)$. Using the chemical potential (4.2.4), the Cahn-Hilliard equation yields:

$$\frac{\partial \phi}{\partial t} + \mathbf{u} \cdot \nabla \phi = M(\rho, \tau_g) \Delta \mu^{(\tau_g)}(\phi). \tag{4.2.5}$$

In order to match the same hydrodynamical properties of the multicomponent LBM, the capillary stress $\mu \nabla \phi$ is obtained adopting the following chemical potential:

$$\mu(\phi) = \frac{c_S^2}{2} \log\left(\frac{\rho+\phi}{\rho-\phi}\right) - \frac{g_{AB}}{2} c_S^2 \phi - \frac{g_{AB}}{4} c_S^4 \Delta \phi. \tag{4.2.6}$$

Equation (4.2.6) is derived from the matching procedure proposed in [99]. Within this formulation, $\mu(\phi)$ represents the large τ_g-limit of the equation (4.2.4), and $\mu^{(\tau_g)} \to \mu$ when $\tau_g \gg 1/2$. The equations of the PFM implemented in this benchmark are the following:

$$\nabla \cdot \mathbf{u} = 0, \tag{4.2.7}$$

$$\frac{\partial \phi}{\partial t} + \mathbf{u} \cdot \nabla \phi = M(\rho, \tau_g) \nabla^2 \mu^{(\tau_g)}(\phi), \tag{4.2.8}$$

$$\frac{\partial \mathbf{u}}{\partial t} + \mathbf{u} \cdot \nabla \mathbf{u} = -\nabla p + \nu(\tau_g) \nabla \cdot (\nabla \mathbf{u} + \nabla \mathbf{u}^T) + \mu(\phi) \nabla \phi, \tag{4.2.9}$$

where the chemical potentials μ and $\mu^{(\tau_g)}$ are given by equations (4.2.6) and (4.2.4) respectively. Their formulation is similar to that used by Mauri *et al.* [75], Vladimirova *et al.* [130] and Molin *et al.* [80]. The mobility coefficient of equation (4.2.8) is $M(\rho, \tau_g) = \rho\,(\tau_g - 1/2)$, whereas the kinematic viscosity of equation (4.2.9) reads $\nu(\tau_g) = c_S^2(\tau_g - 1/2)$. The coefficients τ_g, ρ, g_{AB} and $c_S^2 = 1/3$ are the LBM input parameters and their definitions are reported in Tab 4.1. Equations (4.2.7)-(4.2.9) have been rewritten in a dimensionless form using the dimensionless variables (2.3.1), where the characteristic

Table 4.1 – Definition of the Lattice Boltzmann input parameters and of the corresponding phase field model dimensionless groups.

$\nu = c_S^2\left(\tau_g - \frac{1}{2}\right)$	$M = \rho\left(\tau_g - \frac{1}{2}\right)$	$\kappa = \frac{g_{AB}c_S^4}{4}$
$\beta = \frac{g_{AB}c_S^2}{2}$	$\beta^{(\tau_g)} = \frac{g_{AB}^{(\tau_g)}c_S^2}{2}$	$\xi = \sqrt{\frac{\kappa}{\beta}}$
$Pe = \frac{UH}{\beta^{(\tau_g)}M}$	$Ch = \frac{\xi}{H}$	$Ca = \frac{\nu\rho U}{\sqrt{\beta\kappa}}$
$Re = \frac{UH}{\nu(\tau_g)}$		

length, velocity and concentration h, U_τ and ϕ_+ assume different values depending on this particular problem. Starting from equation (4.2.4), the chemical potential yields to:

$$\mu^-(\phi) = \frac{1}{G_{AB}}\log\left(\frac{\rho^- + \phi^-}{\rho^- - \phi^-}\right) - \phi^- - Ch^2\nabla^2\phi^-, \tag{4.2.10}$$

consistently, equation (4.2.6) reads:

$$\mu^{(\tau_g)-}(\phi) = \frac{1}{G_{AB}^{(\tau_g)}}\log\left(\frac{\rho^- + \phi^-}{\rho^- - \phi^-}\right) - \phi^- - Ch^2\nabla\phi^-, \tag{4.2.11}$$

where $\rho^- = \rho/\phi_+$, $G_{AB} = g_{AB}\phi_+$ and $G_{AB}^{(\tau_g)} = g_{AB}^{(\tau_g)}\phi_+$. The dimensionless form of equations (4.2.7), (4.2.8) and (4.2.9) are:

$$\nabla\cdot\mathbf{u}^- = 0, \tag{4.2.12}$$

$$\frac{\partial\phi^-}{\partial t^-} + \mathbf{u}^-\cdot\nabla\phi^- = \frac{1}{Pe}\nabla^2\mu^{(\tau_g)-}, \tag{4.2.13}$$

$$\frac{\partial\mathbf{u}^-}{\partial t^-} + \mathbf{u}^-\cdot\nabla\mathbf{u}^- = -\nabla\tilde{p}^- + \frac{1}{Re}\nabla\cdot\left(\nabla\mathbf{u}^- + \nabla\mathbf{u}^{-^T}\right) + \frac{1}{ReChCa}\mu^-\nabla\phi^-. \tag{4.2.14}$$

The non-dimensional groups introduced into the equations system (4.2.10)-(4.2.14) are the Cahn number, the Peclet number, the Reynolds number and the Capillary number, which are defined as follows:

$$Ch = \frac{\xi}{H}, \qquad Pe = \frac{UH}{\beta^{(\tau_g)}M}, \qquad Re = \frac{UH}{\nu}, \qquad Ca = \frac{\nu\rho U}{\sqrt{\beta\kappa}}. \tag{4.2.15}$$

The dimensionless groups (4.2.15) appear to be different from those defined for the channel geometry (2.3.6); in this particular case the physical parameters are mapped to match the LBM input parameters, explaining the differences with (2.3.6), in any case their physical meaning still holds. The Cahn number is the ratio between the interface thickness ξ

and the length-scale H, the Peclet number is the ratio between the diffusive time-scale $H^2/(\beta^{(\tau_g)}M)$ and the convective time-scale H/U. The Reynolds number is the ratio between the inertial forces HU and the viscous forces ν. Finally the capillary number is the ratio between the viscous forces $\nu\rho U$ and the capillary forces $\sqrt{\beta\kappa}$ at the interface. All the dimensionless groups and the definitions of the fluid properties with respect to the LBM input parameters are reported in Tab 4.1.

4.2.4 The numerical method

The solution procedure discussed in Chap. is applied to the equations system (4.2.10)-(4.2.14); with the adoption of the chemical potential (4.2.11), the operator splitting adopted for the solution of the Cahn-Hilliard equation yields (where the apex "-" has been removed for sake of simplicity):

$$\frac{\partial \phi}{\partial t} = S_\phi + s\frac{Ch^2}{Pe}\nabla^2\phi - Ch^2\nabla^4\phi. \tag{4.2.16}$$

The non linear term S_ϕ yields:

$$\begin{aligned} S_\phi &= -\mathbf{u}\cdot\nabla\phi + \frac{1}{Pe}\nabla\left[\frac{1}{G_{AB}^{(\tau_g)}}\log\left(\frac{\rho+\phi}{\rho-\phi}\right) - 3\phi\right] \\ &- (s+1)\frac{Ch^2}{Pe}\nabla^4\phi, \end{aligned} \tag{4.2.17}$$

In this benchmark a periodic two dimensional domain is considered; to this aim the numerical algorithm proposed in Chap. 3 has been simplified by neglecting the wall normal direction. As a result, the solution is obtained using Fourier transforms only, thus the Chebyshev-Tau solution has been removed and the resulting linear equations system is solved by Gauss elimination.

4.2.5 Numerical tests

In this section the numerical results obtained from both the PFM and the LBM approaches are discussed. Two different tests have been performed with the three models, SC-LBM, FE-LBM and PFM. First, the equilibration of a two dimensional static droplet has been simulated until the steady state has been reached. Then, starting from the settled droplet, its deformation under a Kolmogorov flow has investigate. For the numerical analysis a SC-LBM model with $\tau_g = 0.55$, $\rho = 1.4$ and $g_{AB} = 0.164$ has been used. The interaction parameter τ_g has been chosen small enough to avoid spurious contributions from the pressure tensor. The other parameters (g_{AB} and ρ) have been chosen in order to obtain $\phi = \rho_A - \rho_B = \pm 1$ inside the pure components. The simulations have been carried out on a two dimensional fully periodic grid of 100×100 nodes, on a computational domain of dimensions $L_x \times L_y = 100 \times 100$. The same simulations performed with the SC model have been repeated with the FE-LBM. Then the PFM simulations have been performed on a two dimensional fully periodic grid[2] composed by 128×128 nodes on a computational domain of dimensions $L_x \times L_y = 2\pi H \times 2\pi H = 100 \times 100$. In particular, PFM dimensionless numbers have been calculated following the definitions reported in Tab 4.1 and their values are collected in Tab 4.2. In order to match $\phi = \pm 1$ in the regions of pure components, the scaling concentration parameter has been chosen $\phi^* = 1$. As result SC/FE-LBM and the phase field model have been set with the same interface and transport properties and thus the results can be both qualitatively and quantitatively compared.

Table 4.2 – Definition of the Lattice Boltzmann and phase field input values.

ρ	τ_g	g_{AB}	$g_{AB}^{(\tau_g)}$	c_S^2
1.4	0.5	0.164	1.804	$\frac{1}{3}$
Pe	Ch	Ca	Re	
0.7930	0.0256	0.0021	1.000	

4.2.6 A steady droplet

A two dimensional static droplet with radius approximately $d/L_x \simeq 1/8$ initiated in a resting fluid has been studied. The simulations have been run letting the drop attain a stationary, equilibrium state. The kinetic energy at the curved interface (Fig 4.3) and the associated stationary configuration of velocity field and order parameter (Fig 4.4 and Fig 4.5) have been measured. The spurious currents shown by the PFM simulations are found almost one order of magnitude smaller that the ones from the LBM. On the other hand both FE and SC LBM models show comparable velocity magnitudes. The flow fields patterns are similar within the three methods, even if in the PFM case these currents are confined in a thinner layer along the interface. Fig 4.6 displays the temporal evolution of the surface tension σ, which is proportional to the difference between the pressure inside the drop (P_i) and the pressure outside the drop (P_o):

$$\sigma(t) = \frac{d}{2} \left[P_i(t) - P_o(t) \right]. \tag{4.2.18}$$

Both the left panel of Fig 4.5 and Fig 4.6 show that the interface properties of the three models are the same (i.e. the same interface structure and the same surface tension at the curved interface). Nevertheless, the oscillations observed in the LBM models in Fig 4.6 are probably non-physical pressure fluctuations which are ruled out in the PFM simulations. The most important feature observed appears to be the change in magnitude and structure of spurious currents: in both the LBM simulations approximately the same spurious currents are found while their intensity is reduced in the case of PFM

---

[2] Due to the use of a spectral solver it is convenient to choose a power of 2 for the number of grid nodes.

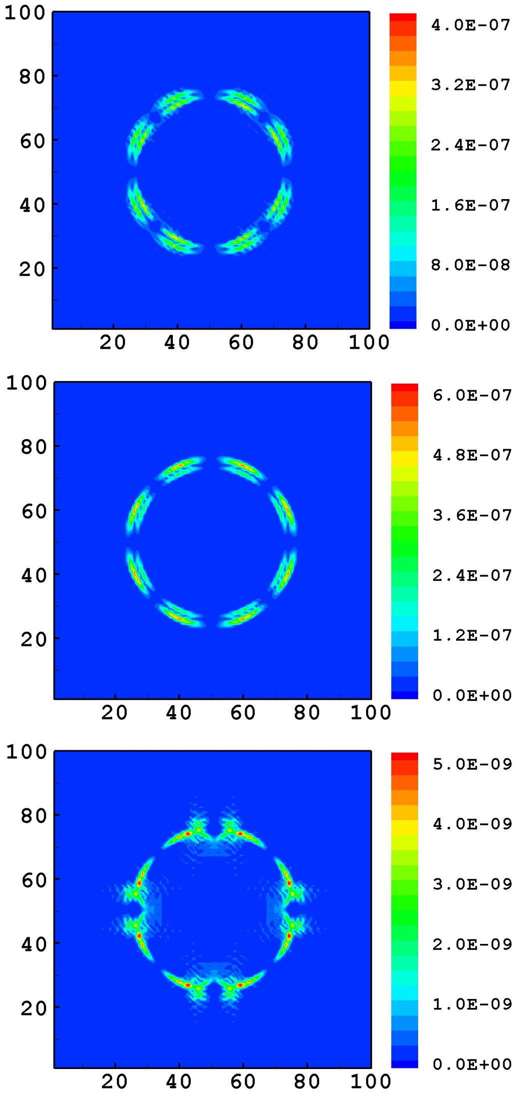

FIGURE 4.3 – Contour plots of the local kinetic energy, per unit density, $\frac{1}{2}(u^2+v^2)$ due to the spurious currents for the FE-LBM (top), SC-LBM (center) and PFM (bottom) methods when simulating a stationary two dimensional droplet. The snapshots are taken at the same time when a steady state has been attained. The intensity and structure of the spurious kinetic terms comparable in the lattice Boltzmann models and is reduced by a factor 100 in the PFM (i.e. a factor 10 on the velocity magnitudes).

simulations. Nevertheless, it is important to remark that the LBM used here are basic versions of the two widely adopted approaches. Improvements can be obtained by curing

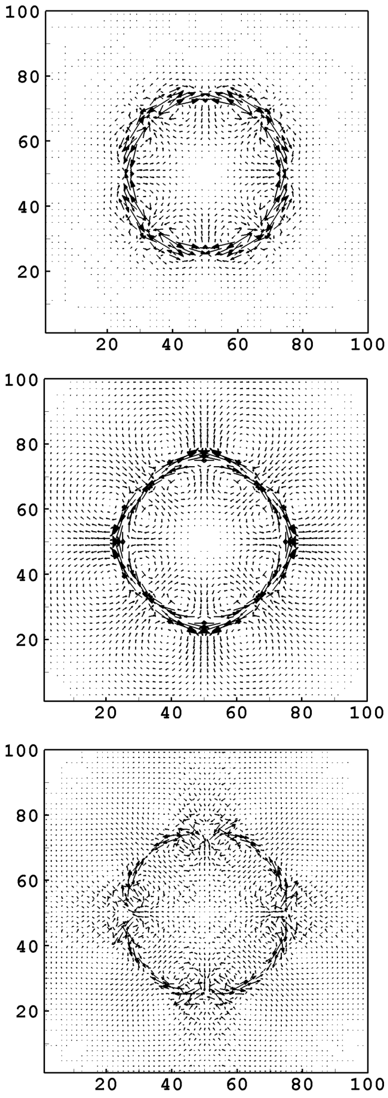

Figure 4.4 – Vector plots of the velocity field due to the spurious currents contributions for the FE-LBM (top), SC-LBM (center) and PFM (bottom) simulations for the two dimensional static droplet. The plots are taken at the same time when the steady state has been reached. The velocity field of the Lattice Boltzmann simulations (top and center plots) have been magnified by a factor 10^4 whereas the vector field of the PFM simulation have been magnified by a factor $5 \cdot 10^4$ for the sake of readability.

discretization errors in the computation of the intermolecular force causing parasitic currents as described by Lee & Fischer [67]. Such improvements have been shown to

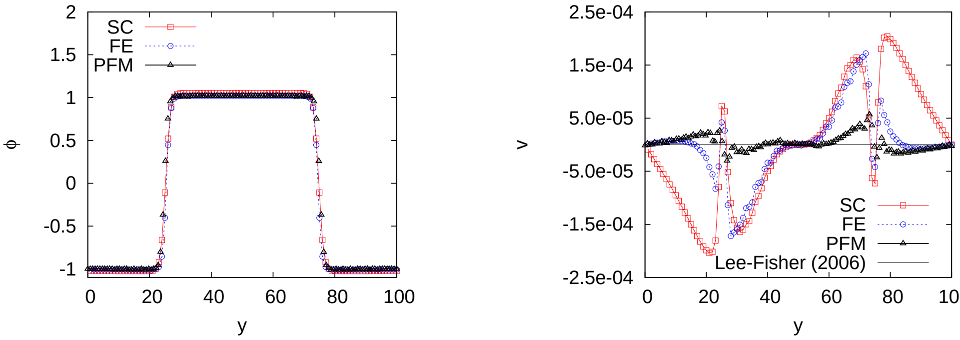

FIGURE 4.5 – Local concentration and velocity profiles from FE-LBM, SC-LBM and PFM simulations of a two dimensional static droplet. On the left the local order parameter, $\phi = \rho_A - \rho_B$, is plotted as a function of the coordinate, y, for fixed $x = 50$. On the right the local (spurious) velocity in the vertical direction, u_y, is plotted as a function of the coordinate, y, for fixed $x = 50$. The order of magnitude of both spurious contributions is comparable in the lattice Boltzmann models while is reduced by a factor 10 (for the velocity, 100 for energy) in the PFM. Improvements in the LBM can be obtained by curing discretization errors in the computation of the intermolecular force as described by Lee & Fischer [67].

eliminate currents to roundoff if the potential form of the intermolecular force is used with compact isotropic discretization. For the sake of completeness the results obtained with the Lee-Fischer scheme have been reported in Fig 4.5.

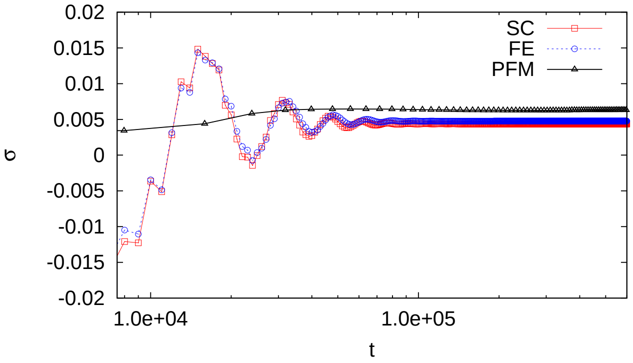

FIGURE 4.6 – Time evolution of the surface tension (Laplace test) from FE-LBM, SC-LBM and PFM simulations of a two dimensional static droplet. Starting from the same initial conditions, the local value of surface tension $\sigma(t)$ is plotted as a function of time.

4.2.7 Droplet deformation under Kolmogorov flow

Starting from the equilibrium droplet obtained from the simulation of Section 4.2.6, a sinusoidal forcing has been applied on the flow field until a new stationary state was reached. The forcing term has been chosen with the following formulation in order to generate a Kolmogorov flow:

$$F_x(\boldsymbol{x}) = \rho A \sin\left(\frac{2\pi y}{L_y}\right), \tag{4.2.19}$$

where $A = 10^{-6}$. In the PFM the dimensionless forcing term is:

$$F_x^-(\boldsymbol{x}) = \frac{AH}{U^2} \sin\left(\frac{2\pi y}{L_y}\right). \tag{4.2.20}$$

The evolution of the total kinetic energy reported in the right panel of Fig 4.9 shows a good matching between the three models, thus the same hydrodynamical transport properties have indeed been imposed. Little discrepancies (less than 10%) between PFM and LBM simulations are shown in the total kinetic energy of the steady state. Moreover little deformation differences can be observed for the concentration iso-contours of Fig 4.8, with the PFM showing a slightly less deformed drop with respect to both LBM. On the contrary both LBM models (SC and FE) show the same concentration profile. The differences in kinetic energy and deformation seem to be consistent one with the other, in fact the less deformed the droplet, the less energy is absorbed from the flow and thus the higher the total kinetic energy (for same external forcing). Qualitative snapshots of the kinetic energy are reported in Fig 4.7, where the iso-contours of $\phi = -0.9$ and $\phi = 0.9$ have been superposed to show the interfacial layer location. Similar patterns and magnitudes are observed within the three models, confirming the correct matching of the models. To test the importance of spurious mass flux across the interface, the mass leakage Δm has been monitored in time:

$$\Delta m(t) = \frac{m(t)}{m_0}, \tag{4.2.21}$$

where $M(t)$ and M_0 are the number of computational nodes inside the droplet at time t and at time $t = 0$, respectively. The nodes with a local order parameter $\phi(\mathbf{x}) \geq \phi_T$, with $\phi_T = 0.0$, have been considered as belonging to the droplet. The results reported in Fig 4.10 show a negligible mass leakage (less than 0.5%) for the PFM and FE, whereas it slightly higher (in the order of 1-3%) for SC-LBM.

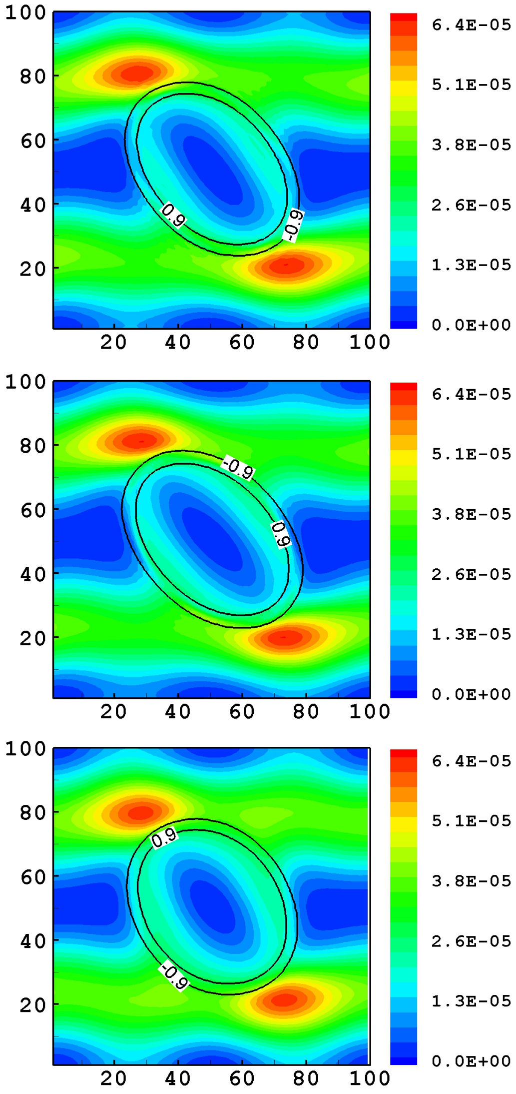

FIGURE 4.7 – Contour plot of the local kinetic energy per unit density $\frac{1}{2}(u^2 + v^2)$ for the FE-LBM (top), SC-LBM (center) and PFM (bottom) simulations of a two dimensional droplet deformation under Kolmogorov flow. The plots are taken at the same time when the steady state has been reached. Similar magnitudes and patterns can be observed for all the models.

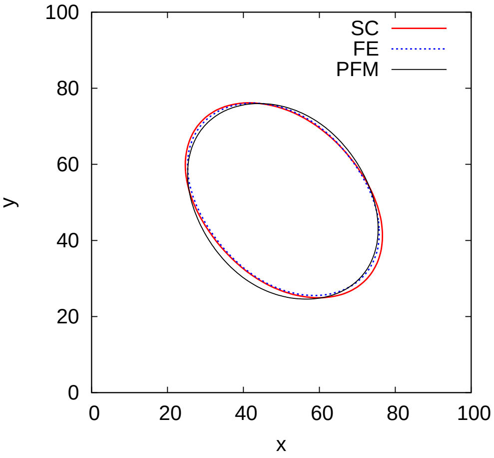

FIGURE 4.8 – Isocontour plot of the concentration field at $\phi = 0$ for the FE-LBM, SC-LBM and PFM for a stationary two dimensional droplet under shear.

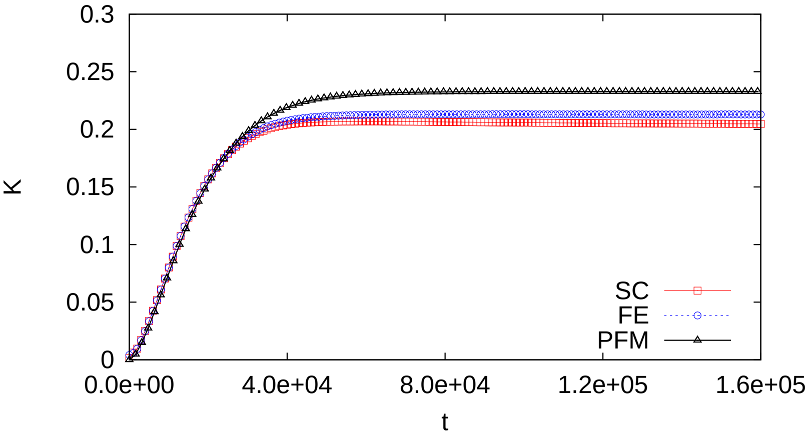

FIGURE 4.9 – Time evolution of the total kinetic energy from FE-LBM, SC-LBM and PFM simulations of a two dimensional droplet deformation under Kolmogorov flow. Starting from the same initial conditions, the total value of the kinetic energy $\iint(u^2 + v^2)\mathrm{d}x\mathrm{d}y$ is plotted as a function of time. Similar evolution in time is registered for all the models, even if the PFM showed an asymptotic value higher than the LBM. The CPU elapsed time of both PFM (T_{PFM}) and SC (T_{SC}) methods have been measured through this simulation. The Lattice Boltzmann method was roughly three times faster than the analogous Phase Field Model ($\frac{T_{PFM}}{T_{SC}} = 2.9$).

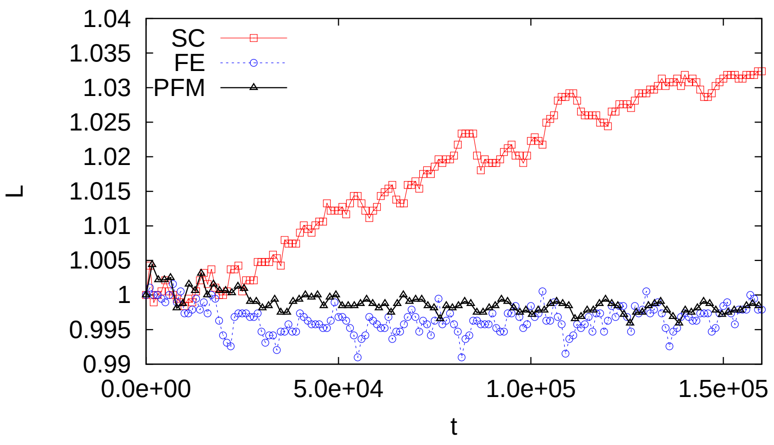

FIGURE 4.10 – Time evolution of the relative leakage of the order parameter from FE-LBM, SC-LBM and PFM simulations of a two dimensional droplet deformation under Kolmogorov flow. Starting from the same initial conditions, the relative leakage $L(t)$ is plotted as a function of time. Longer simulations show that the leakage reached the saturation value for all the three methods.

II

Results

5

Single droplet

Reproduced in part from:

L. Scarbolo and A. Soldati, "Turbulence modulation across the interface of a large deformable drop", J. Turb., 14 (2013).

In this Chapter a single large deformable droplet dispersed in a turbulent channel flow is investigated focusing on the momentum transfer at the interface and its correlation with the Weber number. In the first section the problem is posed and the details of the simulations are provided; in the second section the simulation results are analysed and discussed in detail.

5.1 Problem definition

With reference to the schematic of Fig. 5.1 the evolution of a single fluid droplet of diameter d released in a fully developed turbulent channel flow is analysed. The two fluids are considered immiscible, incompressible, Newtonian, density-matched and viscosity-matched. The interface between them is physically maintained by the surface tension σ. With this assumptions the system is set to its simplest configuration, allowing to isolate the surface tension effects and the turbulence interface interactions. Under these hypotheses the droplet can be considered as a portion of the fluid domain that has been separated from the contiguous fluid introducing an elastic membrane. Setting the Weber number, different systems can be analysed, from a single phase flow when $We \to \infty$ to the dispersion of a rigid fluid sphere in the limit of vanishing Weber number: $We \to 0$ (see Fig. 1.1). In this analysis only small Weber number droplets are considered in order to limit the average deformations, avoiding breakup and getting a linear correlation between We and deformations [95, 92]. The reference coordinate system is located at the center of the channel and x-, y- and z-axes point in the stream-wise, span-wise and wall-normal directions, respectively. The size of the channel is $4\pi h \times 2\pi h \times 2h$ in x, y, and z directions, respectively and h is the channel half-height. The chosen domain size guarantees the complete decorrelation of the velocity field along the periodic directions,

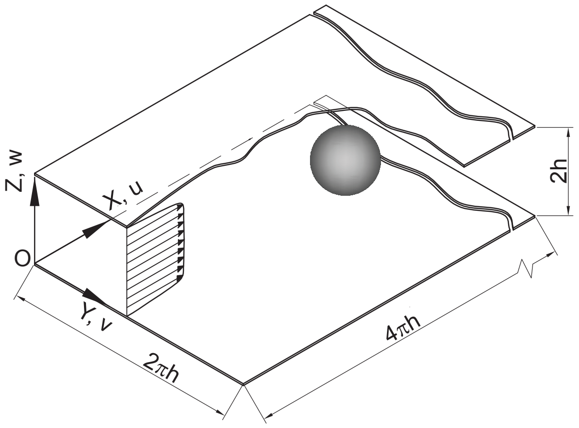

FIGURE 5.1 – Computational domain and problem under analysis: a single deformable droplet is released in a fully developed turbulent channel flow.

thus the droplet behaviour is not affected by periodicity effects. The droplet is initialized by superposing the phase field ϕ over a fully developed turbulent flow obtained from previous single phase DNSs in a statistically steady state. The CHNS equations system (2.3.2)-(2.3.5) are here recalled in their non-dimensional form, where the superscript "−" indicates non-dimensional quantities. The scaling variables here adopted are U_τ, h, and ϕ_+, where $U_\tau = \sqrt{\tau_w/\rho}$ is the shear velocity based on the wall shear stress τ_w and ρ is the fluid density; $\phi_+ = \sqrt{\beta/\alpha}$ is one of the two stable solutions given by the chemical potential (2.2.6).

$$\frac{\partial \phi^-}{\partial t^-} = -\mathbf{u}^- \cdot \nabla \phi^- + \frac{1}{Pe}\nabla^2 \mu^-, \tag{5.1.1}$$

$$\nabla \cdot \mathbf{u}^- = 0, \tag{5.1.2}$$

$$\frac{\partial \mathbf{u}^-}{\partial t^-} = -\mathbf{u}^- \cdot \nabla \mathbf{u}^- - \nabla p^- + \frac{1}{Re_\tau}\nabla^2 \mathbf{u}^- + \frac{3}{\sqrt{8}}\frac{1}{We \cdot Ch}\mu^- \nabla \phi^-, \tag{5.1.3}$$

$$\mu = \phi^{3-} - \phi^- - Ch^2 \nabla^2 \phi^-. \tag{5.1.4}$$

The dimensionless groups (2.3.6) are here recalled:

$$Re_\tau = \frac{U_\tau h}{\nu}, \qquad Pe = \frac{U_\tau h}{M\beta}, \qquad We = \frac{\rho U_\tau^2 h}{\sigma}, \qquad Ch = \frac{\xi}{h}. \tag{5.1.5}$$

Re_τ is the shear Reynolds number, that is the ratio between inertial forces and viscous forces and Pe is the Peclet number that represents the interface relaxation time. We is the Weber number, that is the ratio between inertial forces and the surface tension and Ch is the Cahn number that represents the dimensionless capillary width. All the results reported in this section are measured in wall-units (denoted by the superscript "+") that are obtained normalizing by U_τ, ρ, ν and ϕ_+ (Sect. 2.3.1).

5.1.1 Simulation parameters and accurancy

In this analyses, Re_τ, We, Ch and Pe are macroscopic input parameters defined considering the physical fluid properties, the flow regime, the simulated surface tension and the diffuse interface modelling. Once fixed the shear Reynolds number, the value of the surface tension is chosen by changing the Weber number. When considering immiscible fluids, the interface thickness depends on the numerical algorithm only, thus the Cahn number can be fixed to the smallest possible value. To obtain results independent from Ch, the Peclet number should be properly chosen: for this reason the scaling proposed by Khatavkar [53] has been adopted. Eq. (5.1.1)-(5.1.5) have been solved using a pseudo-spectral algorithm discussed in Chap. 3. In this work the shear Reynolds number based on the half channel height is $Re_\tau = 100$, leading to a fully developed turbulent flow; namely the bulk Reynolds number based on the mean flow velocity u_b is $Re_b = 2u_b h/\nu = 2500$; following [53], the Peclet number is $Pe = 2.56 \cdot 10^5$. Four different Weber numbers have been considered: $We = 0.0053, 0.0106, 0.0212, 0.0424$ and a single droplet diameter $d^+ = 80$. This diameter is much larger than the Kolmogorov length scale η_κ^- at all the positions in the domain: the ratio between the Kolmogorov length scale and the droplet diameter is $0.06 \leq \eta_\kappa^+/d^+ \leq 0.13$. The simulations were run on a $256 \times 128 \times 129$ fixed cartesian grid which is fine enough to resolve the smallest length scale of the turbulent flow $(\max[\Delta z^+] < \Delta x^+ \simeq \Delta y^+ < \eta_\kappa^+)$[1], while the time step $\Delta t^+ = 10^{-2}$ has been chosen to resolve correctly the smallest temporal scales and respond to the numerical stability requirements associated with the grid resolution. The pseudo-spectral scheme adopted can resolve accurately the interfacial layer with a minimum number of three mesh-points [5, 99]. With reference to Eq. (2.2.7) the interface thickness is $l_\xi^+ = 4.164 Re_\tau Ch$, yielding to a variation of the order parameter $-0.9 \leq \phi^+ \leq 0.9$. Choosing $Ch = 0.036$, the interfacial layer is described by three-mesh points along x and y directions, where a uniform discretization is adopted ($\Delta y^+ \simeq \Delta x^+ = 4 Re_\tau \pi h/255$). Along the z direction, a finer non-uniform discretization is adopted: l_ξ^+ is described by a minimum number of seven mesh-points. The DI models cannot completely fulfil local mass conservation [141] and this issue has been observed also in this work. However, thanks to the accuracy of the numerical scheme adopted, the mass loss is in any case small and the estimated jumps of the interface-normal velocity component across the interface are of $O(10^{-5})$ [99]. In particular, after the entire simulation ($3 \cdot 10^5$ time-steps), losses of volume V^+ (or equivalently of mass m) range from 4% to 14% for $We = 0.0053$ to $We = 0.0424$, respectively. This correspond to a maximum reduction of 6% of the equivalent droplet diameter $d_{eq}^+ = \sqrt[3]{3V^+/4\pi}$ and a relative mass transfer $\Delta(m/m_0)/\Delta t^+ = 5 \cdot 10^{-3}$. A collection of the relevant parameters of each simulation is reported in Tab. 5.1.

---

[1] The Chebyshev transform, adopted along the wall-normal direction, produces a non-uniform grid spacing highly refined at the walls where large gradients have to be resolved.

TABLE 5.1 – Summary of the simulation parameters and average deformation $\langle S/S_0 - 1\rangle$ for each simulation.

Simulation	We	Re_τ	Ch	Pe	$\langle S^+/S_0^+ - 1\rangle$
W1	0.0053	100	0.036	$2.56 \cdot 10^5$	$0.39 \cdot 10^{-3}$
W2	0.0106	100	0.036	$2.56 \cdot 10^5$	$1.28 \cdot 10^{-3}$
W3	0.0212	100	0.036	$2.56 \cdot 10^5$	$2.41 \cdot 10^{-3}$
W4	0.0424	100	0.036	$2.56 \cdot 10^5$	$6.54 \cdot 10^{-3}$

5.2 Results and Discussion

In this Chapter, the effects of surface tension on the turbulent velocity fluctuations at the interface of a large deformable droplet released in a turbulent channel flow are investigated. To study the features of the turbulent flow in proximity to a deformable interface moving in a non-homogeneous flow, first the velocity field over the droplet interface has been examined (Sect. 5.2.2), then the behaviour of the flow field at both sides of the interface has been analysed (Sect. 5.2.3) and, finally, the turbulence inside of the droplet has been compared with that outside the droplet (Sect. 5.2.4). To examine these different issues of the problem, the analysis has been performed adopting different viewpoints, so that the investigate features have been highlighted. In Fig. 5.2, the three different fluid domains considered for the analysis are reported: velocity field over the droplet surface (Fig. 5.2-a), velocity field across the interface of the droplet (Fig. 5.2-b) and turbulent field inside and outside of the droplet (Fig. 5.2-c). Time-independent statistical results have been obtained by time averaging over a window $\Delta T^+_{sim} = 3000$, that corresponds to a ~ 30 eddy turnover times $T_e = h/U_\tau$.

5.2.1 Droplet behavior and turbulent features

After released in the fully developed turbulent channel flow (Fig. 5.1), the droplet is advected by the flow field, and its center of mass moves with non-zero stream-wise velocity u^+_{cm}. Due to the turbulent fluctuations, the droplet also moves along the span-wise and wall-normal directions with a meandering trajectory and, during the entire simulation, the droplet never reaches wall distances closer than $20 w.u.$. Since the droplet has a density equal to that of the external fluid, its velocity and position are affected by inertial effects: the main difference from a rigid body is due to the deformability, thus inertial effects are expected to be dependent on We. When We is small (simulation $W1$), the surface tension prevents the turbulent motions from deforming the interface while increasing the Weber number, the interface of the droplet reduces its ability to react to the external turbulent forcing resulting in larger deformations. To quantify the droplet instantaneous deformations, the external surface of the droplet $S^+ = S^+(t^+)$ is monitored in time. The time averaged deformation $\langle S^+/S_0^+ - 1\rangle$ is reported in Fig. 5.3 for a wide range of Weber numbers, where $S_0^+ = S_0^+(t^+)$ is the area of an equivalent sphere

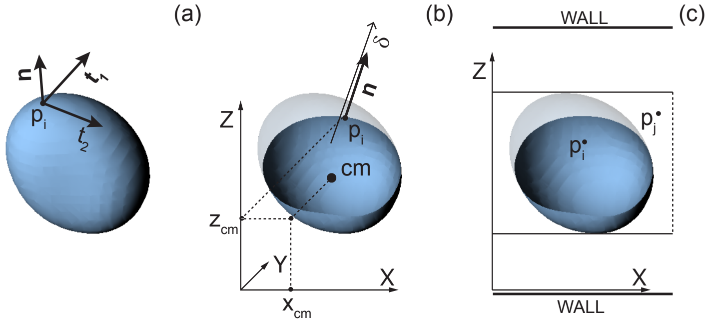

FIGURE 5.2 – Sketch of the fluid domains adopted for data analysis. Statistics on the droplet surface (a) are obtained considering all the points p_i on the droplet surface, where $\mathbf{n}$, $\mathbf{t_1}$ and $\mathbf{t_2}$ are the interface-normal vector and the interface-tangential vectors, respectively. Statistics across the interface (b) are computed considering first the interface-normal directions at points $p_i(x, y, z_{cm})$ of the interface, where z_{cm} is the wall-normal coordinate of the droplet center of mass. Averages are made over the ensemble of points located at distance δ from the interface. Statistics inside of the droplet (c) are obtained considering the points p_i the volume of fluid inside the droplet interface; statistics outside of the droplet are made on the points p_j of the volume of fluid external to the droplet and limited to the channel flow buffer layer ($30w.u. \leq z^+ \leq 170w.u.$)

computed from the the instantaneous droplet volume[2] (brackets denote time averaging). The Weber number range reported in Fig. 5.3 has been extended up to breaking droplets; in the next sections, only cases of non-breaking droplets will be considered and in particular the chosen We lead to small average deformations: ($0.03\% < \langle S^+/S_0^+ - 1\rangle < 0.7\%$). The droplet deformation shows almost linear behaviour $\langle S^+/S_0^+ - 1\rangle \propto We$ up to values close to a critical We, where the turbulent forcing is strong enough to split the droplet. This behaviour is consistent with the experimental observations of Risso *et al.* [95] and the numerical analysis of Qian *et al.* [92], who found an almost linear behaviour of the deformations in the limit of non breaking bubbles. Since for the considered Weber numbers ($W1$-$W4$) the droplet deformations are linear with We and ultimately with $1/\sigma$, it is possible to directly correlate the Weber number with the droplet deformability. The presence of the interface is responsible for the modification of the local turbulent structures and in particular of turbulent transport at length scales $l^+ \propto d^+$. In Fig. 5.4 the vortical structures near the interface are shown for two different We: snapshots of simulation $W1$ (small deformations) and $W4$ (large deformations) at non-dimensional time $t^+ = 1600$ are reported in Fig. 5.4-a and Fig. 5.4-b, respectively. Coherent structures are identified using the second invariant Q of the velocity gradient tensor $\nabla \mathbf{u}^+$ [46]:

$$Q = \frac{1}{2}\left(\Omega_{ij}\Omega_{ij} - S_{ij}S_{ij}\right), \tag{5.2.1}$$

where $\Omega_{ij} = 1/2(u^+_{ij} - u^+_{ji})$ and $S_{ij} = 1/2(u^+_{ij} + u^+_{ji})$ are the anti-symmetric and symmetric components of $\nabla \mathbf{u}$, respectively. The vorticity magnitude $|\boldsymbol{\omega}^+|$ has been superim-

---

[2] The small mass losses are sufficient to affect the average deformation if the nominal droplet radius is considered to compute S_0^+. Adopting an equivalent spherical radius computed from the instantaneous volume yields to an accurate prediction of the droplet deformation.

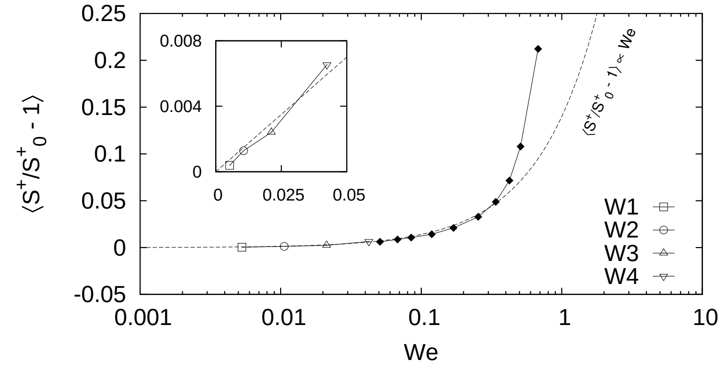

FIGURE 5.3 – Average droplet deformation $\langle S^+/S_0^+ - 1\rangle$ at various Weber numbers We: plain dots represent the Weber numbers considered also for the velocity field analysis, filled dots complete the discussion on the droplet deformation and breakup.

posed to the vortices identified with iso-surfaces $Q = Q_t > 0$, where the threshold value $Q = 0.0038$ has been chosen for a non biased representation of the eddies. When the deformability is low ($W1$, Fig. 5.4-a), the region of fluid near the droplet is populated by a larger number of turbulent structures than in the large deformability case ($W4$, Fig. 5.4-b). The reduced number of coherent structures observed is probably due to the elastic behaviour of the interface that first damps the turbulent forcing, releasing it at different lengths scales, at different times, and at different positions over the surface. The release of energy acts as a non-synchronous damper in the turbulent chain, producing fluid motions which are not coherent with those responsible for the energy accumulation. By contrast the higher number of coherent structures observed in the low deformability case ($W1$) is probably due to the deviation of the flow produced by the interface that yields to structures smaller in size than the typical channel flow vortices. These structures are coupled with peaks of vorticity magnitude, which are likely due to the shear stress induced by the interface, while, when the interface is more deformable, the vorticity levels appear to be comparable to those registered in the buffer layer (see vorticity contours in Fig. 5.4).

5.2.2 Velocity fluctuations over the droplet surface

In this section the surface-normal velocity fluctuations $u_n^{+,*}$ and the surface-tangential velocity fluctuations $u_t^{+,*}$ measured over the surface of the droplet are analysed. Since the droplet is a finite size body moving in a non-homogeneous flow field, the definition of homogeneous statistical directions is not trivial, therefore Probability Density Functions (PDF) of the normal an tangential velocity fluctuations are presented. The interface has been defined as the position where $\phi = 0$ and the velocity components have been projected on the directions normal and tangential to the surface. Since two tangential vectors are identified at each interface location, only the magnitude of the tangential component

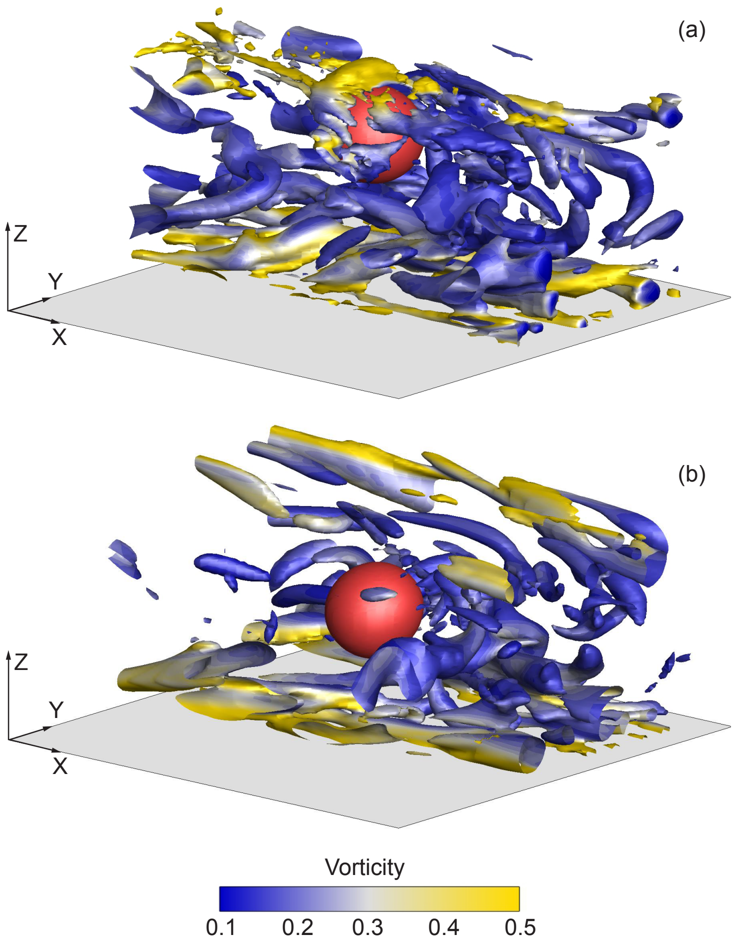

FIGURE 5.4 – Interactions between vortical structures and droplet for different Weber numbers at time $t^+ = 1600$: (a) simulation $W1$, (b) simulation $W4$. Vortices are identified with iso-surfaces of the second invariant of the velocity gradient: $Q = 0.0038$ (Q-criterion). Contour plots of the local vorticity magnitude $\omega^+ = |\boldsymbol{\omega}^+|$ are superposed to the vortices. The droplet interface is located by the iso-surface $\phi^+ = 0$ and is rendered in red. The entire computational domain along the wall-normal direction is shown (portion of the bottom wall is shown for clarity), while only a portion of it is shown along the length-wise and span-wise directions ($\Delta x^+ \times \Delta y^+ = 400 \times 250$). Near the more deformable droplet ($W4$), the observed turbulent structures density is reduced and their size is larger compared to those near the stiffer droplet ($W1$). Peaks of vorticity magnitude are observed near the stiffer droplet.

has been considered $u_t^{+,*} = |\mathbf{u}_t^{+,*}|$. To compare the results with those available in the literature in absence of mean flow, the velocity fluctuations $\mathbf{u}^{+,*}$ have been defined with respect the droplet center of mass velocity $\mathbf{u}_{cm}^+$: $\mathbf{u}^{+,*} = \mathbf{u} - \mathbf{u}_{cm}$. Adopting this decomposition, also the convective effects are better highlighted. In Fig. 5.5, PDFs of

$u_n^{+,*}$ and $u_t^{+,*}$ are shown for the different Weber numbers. Increasing We, a reduction of the interface-normal component (Fig. 5.5-a) coupled with a strengthening of the interface-tangential component (Fig. 5.5-b) is observed. This effect can be attributed to the wall-blocking effects, as indicated by Perot and Moin [87], who showed how the flow streams impacting solid interfaces are deflected from the interface-normal direction to the interface-tangential directions (intercomponent energy exchanges). In our case, responsible for the wall blocking effect is the local normal stress $\tau_n = \sigma/\bar{r} \cdot \mathbf{n}$ that arises at the droplet interface because of the surface tension and the finite curvature radius $\bar{r}$. A first effect is due to the dependency of τ_n on the surface tension: the wall-blocking effects increase when We is reduced and, in turn, intercomponent exchanges are larger for smaller We (as observed also by Trontin [122]). A second effect is related to the normal

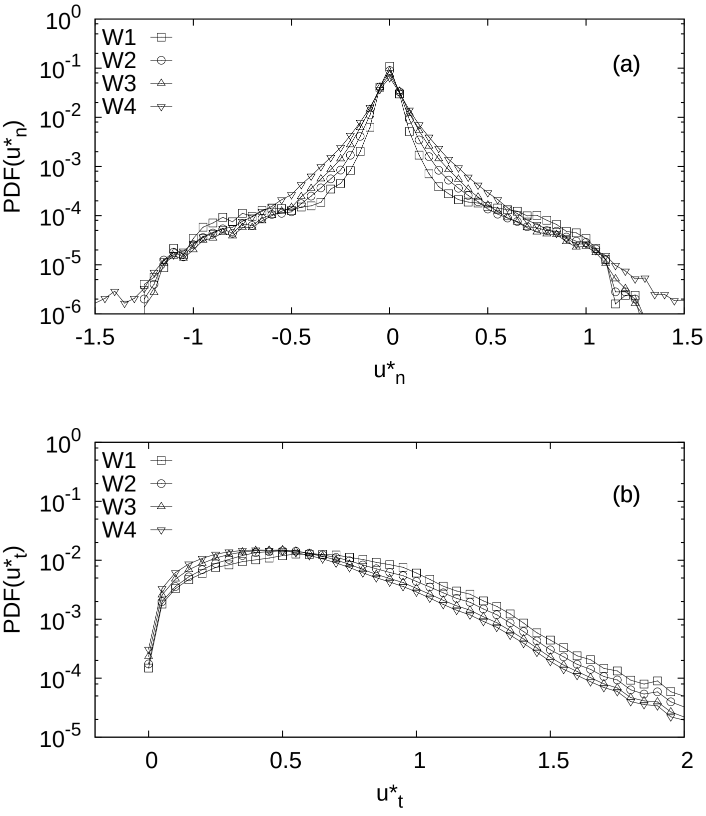

Figure 5.5 – Probability Density Functions (PDF) of the velocity fluctuations $\mathbf{u}^{+,*}$ (computed with respect to the droplet center of mass velocity) on the surface of the droplet at various Weber numbers We: (a) surface-normal velocity fluctuations $u_n^{+,*}$; (b) surface-tangential fluctuations $u_t^{+,*}$. Interface-normal components increase with the droplet deformability (increasing We), whereas tangential components reduce with the interface deformability.

stress dependency on the local deformations: large and energetic structures impacting on the interface act to reduce the local curvature, corresponding to a reduction of τ_n. This can explain the dependence of $u_n^{+,*}$ on We confined in a range of small velocities ($0.5 \leq |u_n^{+,*}| \leq 0$) observed in Fig. 5.5. The velocity field modification in the proximity of the droplet is shown in in Fig. 5.6: the vector plot of the fluctuating velocity field $\mathbf{u}'$ and the contour plot of the turbulent kinetic energy $k^+ = \mathbf{u}' \cdot \mathbf{u}'$ are depicted on a x-y plane (parallel to the walls) that crosses the droplet center of mass. The flow stream impacting on the droplet surface for the smaller Weber number ($W1$, Fig. 5.6-b) is deflected from the interface-normal to the interface-tangential direction, generating then some small vortical structures. By contrast, when the interface is more deformable ($W4$, Fig. 5.6-b), the flow stream impacting on the droplet can deform the droplet, flattening the interface and, as a result, the velocity modifications are of smaller entity. The presence of intercomponent exchange effects dependent on We is also consistent with the increment of small coherent structures observed in Fig. 5.4.

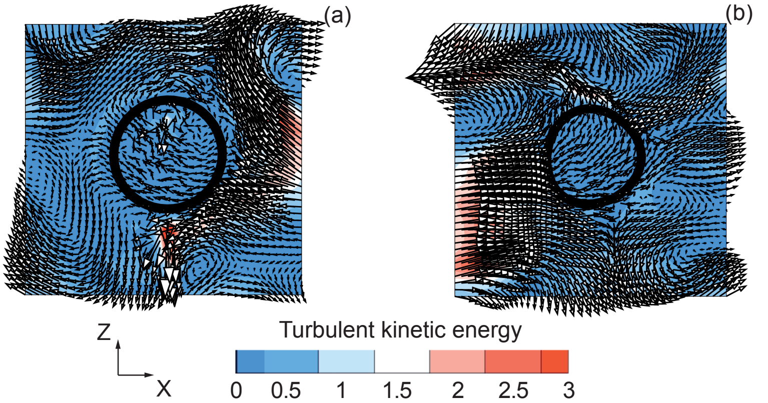

FIGURE 5.6 – Detail of the interactions between the droplet interface and the fluctuating velocity field for different Weber numbers at time $t^+ = 1500$: (a) simulation $W1$, (b) simulation $W4$. Contour plots of the local turbulent kinetic energy $k^+ = \mathbf{u}^+ \cdot \mathbf{u}^+$ are depicted on a x-y plane that crosses the droplet center of mass. The vector plot of the fluctuating velocity field $\mathbf{u}^{+'} = \mathbf{u}^+ - \hat{\mathbf{u}}^+(z)$ is reported and the droplet interface is located by the iso-surface $\phi^+ = 0$. Near the less deformable droplet ($W1$), the velocity field is deflected by the interface; in the proximity of the more deformable droplet ($W4$) the velocity field is less modified and the droplet interface is flattened.

5.2.3 Statistics across the interface of the droplet

To clarify the intercomponent exchange discussed in Sect. 5.2.2, the behaviour of the turbulent field across the interface is analysed. Turbulence kinetic energy $k^+ = \mathbf{u}^{+,*} \cdot \mathbf{u}^{+,*}$, vorticity magnitude $\omega^+/\omega_0^+ = |\nabla \times \mathbf{u}^+|/\omega_0^+$ and Root Mean Square (RMS) of the velocity fluctuations have been analysed across the interface (identified by the surface where $\phi = 0$). The vorticity has been normalized with the average vorticity magnitude ω_0^+ measured in the buffer layer of a single phase flow. and the same velocity decomposition presented in Sect. 5.2.2 has been maintained: $\mathbf{u}^{+,*} = \mathbf{u}^+ - \mathbf{u}_{cm}^+$. With reference to the interface points p_i shown in Fig. 5.2-b, the analysis has been performed along the directions normal to the droplet surface at p_i. Then, considering the droplet center of mass position $\mathbf{x}_{cm} = (x_{cm}, y_{cm}, z_{cm})$, only the interface points p_i with wall-normal coordinate z_{cm} have been considered: $p_i = p_i(x_{\phi=0}, y_{\phi=0}, z = z_{cm})$. Along those interface-normal directions, the quantities under analysis have been measured at distances δ^+ from the interface ranging from $-20w.u. \leq \delta^+ \leq 60w.u.$, where $\delta^+ = 0$ represents the intersection with the droplet interface and δ^+ increases moving outside of the droplet (see Fig. 5.2-b). With the adoption of this framework, the quality of the statistical samples is improved: since z_{cm} is in confined in the channel buffer layer for most of the time, measures are made in regions of limited wall-normal non-homogeneity. Furthermore, the velocity fluctuations $\mathbf{u}^{+,*}$ show a nearly flat profile in the center of the channel. In addition the selected range of Weber numbers yields to small average deformations, thus to small variations of curvature and in the end to small deflections of $\mathbf{n}$ from the x-y planes. As a result, the accuracy of the statistical analysis is increased. The measured quantities have been time and ensemble averaged (denoted by brackets), where ensemble averaging has been made over all the realizations obtained at the same distance δ^+ from the interface. The evolution of the turbulence kinetic energy and the evolution of the vorticity magnitude along the interface normal direction are shown in Fig. 5.7-a and Fig. 5.7-b, respectively. The turbulent kinetic energy is damped moving from outside of the droplet to the droplet interface for all the Weber numbers considered (Fig. 5.7-a). The damping rate $\Delta k^+/\Delta\delta^+$ is larger near the interface and it reduces at larger δ^+. Inside of the droplet ($\delta^+ < 0$) a damping of 80% of k^+ is observed with respect to the value measured at $\delta^+ = 60w.u.$ and, across the interface (half-thickness of $7.4w.u.$ measured at $\phi^+ = \pm 0.9$ [5]), k^+ shows a magnitude comparable to that observed inside the droplet. The results indicate that the damping effects take place in a region outside of the droplet and, as expected, the interface effects reduce moving far from the interface. Near the interface a vorticity production ($\omega^+/\omega_0^+ > 1$) can be observed for all the considered Weber numbers and at both sides of the interface (Fig. 5.7-b). In the outer side of the interface, production is due to the intercomponent energy transfer (wall-blocking effect [87]) that yields to the generation of the small coherent structures highlighted in Sect. 5.2.1. Since the wall-blocking effect depends on the surface tension, the vorticity production peak increase when We reduces. This result is consistent with the results of Trontin [122] and Li [68] and with the wall-blocking mechanism discussed in Sect. 5.2.2. The peak of production is registered in a region of $7w.u. \leq \delta^+ \leq 14w.u$, then vorticity production reduces increasing the distance from the interface and, at $\delta^+ = 60w.u.$, $\omega^+/\omega_0^+ \approx 1.1$. This behaviour indicates a weaker flow field deviation with respect to the near interface region, where the blocking effect is larger. By contrast, at $\delta^+ = 60w.u.$, the droplet effects on the turbulent kinetic energy are still important. The evolution of the RMSs of the interface-normal and the interface-tangential velocity fluctuations along the interface normal direction are shown in Fig. 5.8-a and Fig. 5.8-b, respectively. The RMSs of the interface-normal fluctuations decrease moving from large δ^+ to the droplet surface (Fig. 5.8-a), in particular their behaviour appear to be almost independent from We and the profiles collapse on a single line. The interface effects are non-negligible along the whole

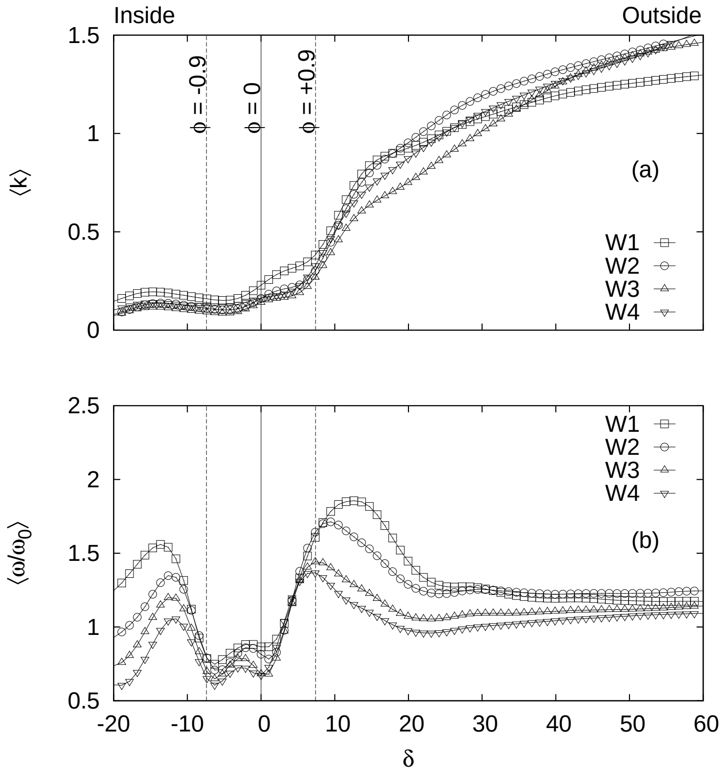

FIGURE 5.7 – Statistics across the droplet interface at various Weber numbers We: (a) averaged turbulent kinetic energy $\langle k^+ \rangle = \langle \mathbf{u}^{+,*} \cdot \mathbf{u}^{+,*} \rangle$ (where $\mathbf{u}^{+,*}$ is computed with respect to the droplet center of mass velocity); (b) average normalized vorticity magnitude $\langle \omega^+/\omega_0^+ \rangle = \langle (\nabla \times \mathbf{u}^+)/\omega_0^+ \rangle$. Turbulent kinetic energy decays moving closer to the droplet, while vorticity increases in the proximity of the interface. Vorticity production peak decreases with the droplet surface tension (decreasing We).

distance considered $\delta^+ = 60 w.u.$, thus statistics extended[3] to larger δ^+ are needed to define the complete range of spatial interaction. At distances $\delta^+ \geq d^+/2$, the RMSs decay is compared with the ${\delta^+}^{1/3}$ scaling law showing a qualitative consistency with the theory developed by Hunt and Graham [45] for a solid interface in a free-stream flow. The authors indicated that the distortion in the velocity field can be seen up $\delta^+ \propto L$ where L is the size of the largest vortex of the flow and that the interface-normal RMS decays as ${\delta^+}^{1/3}$ in regions close to distances L. In our case the droplet is expected to interact with eddies of size spanning from the Kolmogorov length scale η_k^+ $(2.5 w.u - 11 w.u.)$ to the droplet diameter $d^+ = 80 w.u.$, furthermore the droplet interface is deformed by large and energetic structures. As a result discrepancies from theory [45] are observed. The

---

[3] The extension to larger distances can lead to an increasing statistical non-homogeneity of the sample, thus different analysis framework should be adopted.

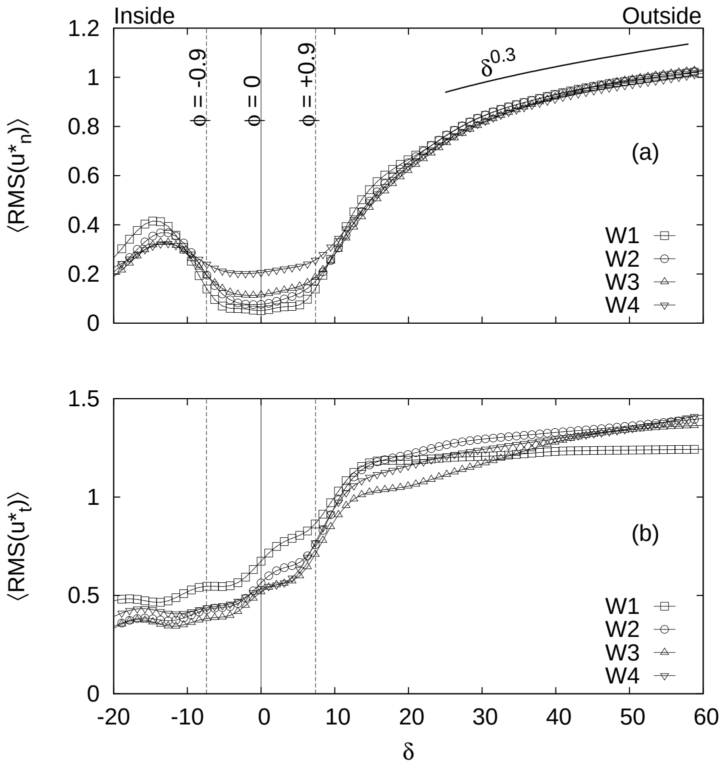

Figure 5.8 – Statistics across the droplet interface at various Weber numbers We: (a) interface-normal velocity fluctuations $\langle RMS(u_n^{+,*})\rangle$; (b) interface-tangential velocity fluctuation $\langle RMS(u_t^{+,*})\rangle$. Velocity fluctuations $\mathbf{u}^{+,*}$ are computed with respect to the droplet center of mass velocity. Both velocity components are damped approaching the droplet interface. Near the droplet $\langle RMS(u_t^{+,*})\rangle$ shows a faster decay with respect to $\langle RMS(u_n^{+,*})\rangle$. A qualitative comparison with the scaling ${\delta^+}^{0.3}$ at distances $\delta \propto d^+$ [45] is proposed.

RMSs of the interface-tangential components (Fig. 5.8-b) show a fast decay in a region close to the droplet interface $15 w.u.$ (corresponding to large vorticity production), while smaller reduction rates are observed at larger distances. The simultaneous damping of $u_t^{+,*}$ and $u_n^{+,*}$ is the origin of the reduction of k^+ and is probably associated to the vorticity production ω^+/ω_0^+ that yields to an incomplete energy transfer between the two components. These effects are large in the near interface regions $\delta^+ \leq 15 w.u.$, where the flow field deflection (and the vorticity production) is large, while they reduce moving far from the interface.

5.2.4 Velocity fluctuations inside the droplet

In Sect. 5.2.3 the damping of the turbulent kinetic energy across the droplet interface has been shown. To quantify the modulation effects produced by the presence of the interface on the fluid embedded inside of the droplet, the velocity fluctuations inside the droplet have been measured. In this case the usual turbulent channel flow decomposition $\mathbf{u}^{+'} = \mathbf{u}^{+} - \hat{\mathbf{u}}^{+}(z)$ has been adopted to compare the fluctuating field $\mathbf{u}^{+'}$ with the single phase turbulent channel flow statistics. The PDFs[4] of the velocity fluctuations measured inside of the droplet (points p_i in Fig. 5.2-c) have been compared with the PDFs of the velocity fluctuations measured outside of the droplet: a channel slab parallel to the walls with the same height of the deformed droplet and centered into the droplet center of mass has been considered (points p_j in Fig. 5.2-c). In both cases the statistical ensemble has been restricted to the points of the volume of fluids contained in the channel flow buffer layer (defined as the region $30 w.u.$ far from both walls). Even if the droplet surface sometimes reaches positions $20 w.u.$ close to to the walls, the largest part of its volume lies into the buffer layer, thus the PDFs of the velocity fluctuations can be compared with the single phase turbulent channel flow statistics [26]. A schematic of the fluid domains considered for this analysis is shown in Fig. 5.2-c, while the PDFs of $u^{+'}$, $v^{+'}$ and $w^{+'}$ are shown in Fig. 5.9-a, Fig. 5.9-b and Fig. 5.9-c, respectively. The presence of the droplet shows a small influence on the outer flow field, except for stream-wise fluctuations $u^{+'} \leq -3$ where some damping effects can be observed. These effects could be due to two different mechanisms: first, the droplet moves in a region characterized by a negative skewness factor [146], thus the damping effects introduced are expected to affect more the negative velocity components. Second, the meandering motion of the droplet from the channel center to the near-wall regions introduce an higher mean flow component that can damp the negative fluctuations and enhance the positive components. Since the velocity difference is smaller for the positive components, their enhancement is negligible compared to the negative fluctuations damping. All the three velocity components are damped inside the droplet (dots), with respect to the velocity fluctuations measured outside the droplet (lines). Due to the damping of turbulence kinetic energy discussed in Sect. 5.2.3, the velocity fluctuations near the droplet interface are small and, as a result, the momentum transfer across the interface is limited. Inside of the droplet, the negative skewed stream-wise velocity distribution is shifted toward an almost centered shape (Fig. 5.9-a). The increased isotropy of $u^{+'}$, observed inside the droplet reducing We, can be explained by the redistribution of the external turbulent forcing over the whole interface produced by the surface tension. This process is more effective when surface tension is high, by contrast a more deformable interface can easily transfer the external field features to the fluid inside of the droplet across its local deformations.

---

[4] As in Sect. 5.2.2, The results analysis across Probability Density Functions allow to treat the sample non homogeneity.

5.3 Conclusions

In this chapter the surface tension effects on the velocity field in the proximity of a large deformable droplet in turbulence have been analysed for a wide range of Weber numbers in which the average deformation is linear with We. The velocity fluctuations relative to the droplet center of mass, measured at the droplet interface have been analysed in terms of interface-normal and interface-tangential components. The normal components are reduced increasing the surface tension, whereas the tangential components show an opposite behaviour, according to the presence of the wall-blocking effects [87, 68, 122]. The presence of the interface produces a deviation of the surrounding velocity field, that results in a vorticity generation dependent on the surface tension and in a damping of the turbulence intensity near the interface. These effects are experienced at larger distances from the interface increasing the surface tension. Furthermore the turbulent features observed at the surface of the droplet show similarities to those observed for solid walls in free-stream flows [45]. As a result, the convective effects at the droplet surface are damped, the momentum transport across the interface is reduced and the turbulence inside the droplet is weaker.

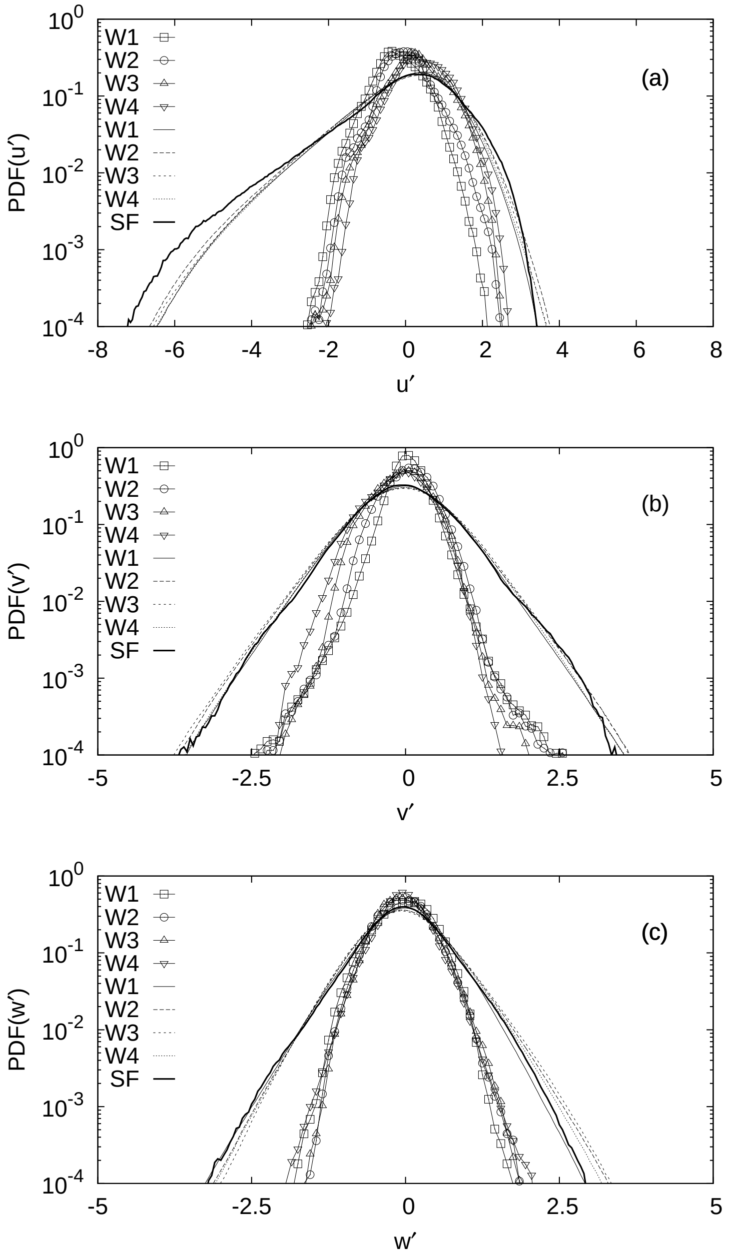

FIGURE 5.9 – Probability Density Functions (PDF) of the velocity fluctuations $\mathbf{u}^{+'}$ (computed with respect to the channel flow mean velocity), measured inside the droplet (dots), in the buffer layer outside the droplet (lines) and for a single phase flow (SF) at various Weber numbers We: (a) stream-wise fluctuations $u^{+'}$; (b) span-wise fluctuations $v^{+'}$; (c) wall-normal fluctuations $w^{+'}$. Velocity fluctuations are damped inside of the droplet, whereas the effects produced on the external velocity components are of small entity.

6

Large number of droplets

Reproduced in part from:

L. Scarbolo and A. Soldati, “Wall drag modification by large deformable droplets in turbulent channel flow”, Comp. Fluids, (2013) *under review.*

L. Scarbolo, F.Bianco and A. Soldati, “Turbulent motions of large coalescing droplets”, J. Fluid Mec., (2013) *in preparation.*

In this chapter the behaviour of a swarm of large deformable and coalescing droplets in wall-bounded turbulence is examined. Droplet-droplet interactions and the wall-drag modifications are investigated exploring a wide range of Weber numbers. In the first section the problem is posed and the details of the simulations are provided; in the second section the coalescence regimes are discussed in detail and in the third second section the flow field modifications are quantified.

6.1 Problem definition

A swarm of droplets of initial diameter d_0 dispersed in a fully developed turbulent channel flow is simulated; the two fluids are considered immiscible, incompressible, Newtonian, density-matched and viscosity-matched. Moreover the complex droplet-droplet interactions (i.e. collisions and coalescences) and the breakup phenomena are properly modelled through the PFM. With this assumptions the system is set to its simplest configuration, allowing to isolate the surface tension effects and the role of droplets deformability on the wall-drag modification. With reference to figure 6.1 the coordinate system is located at the center of the channel and x-, y- and z-axes point in the streamwise, spanwise and wall-normal directions, respectively. The size of the channel is $4\pi h \times 2\pi h \times 2h$ in x, y, and z directions, respectively, and h is the channel half-height. The droplets are initialized by superposing the phase field ϕ over a fully developed turbulent flow obtained from previous single phase DNSs in a statistically steady state. The CHNS equations (2.3.2)-(2.3.5) have been recalled in their non-dimensional form, where the superscript

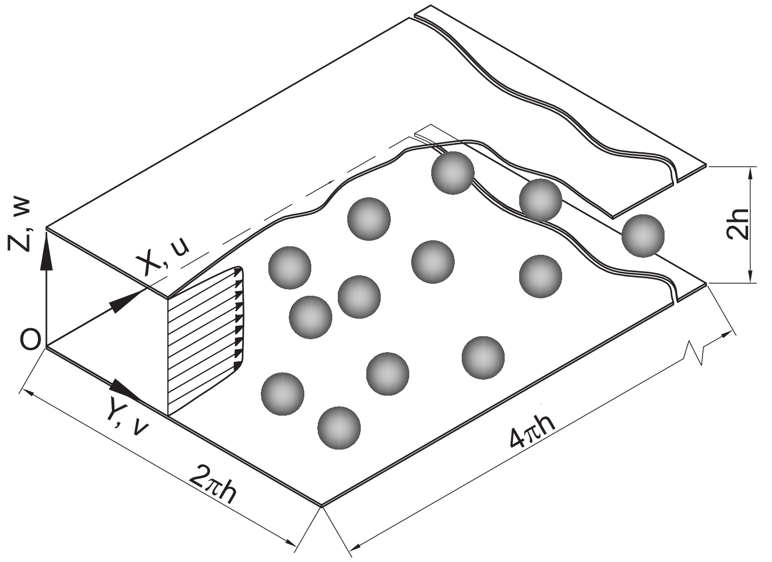

FIGURE 6.1 – Schematics of the problem under analysis: dispersion of a swarm of large deformable droplets in a turbulent channel flow.

"–" indicates non-dimensional quantities. The scaling variables here adopted are U_τ, h, and ϕ_+, where $U_\tau = \sqrt{\tau_w/\rho}$ is the shear velocity based on the wall shear stress τ_w and the fluid density ρ; $\phi_+ = \sqrt{\beta/\alpha}$ is one of the two stable solutions given by the chemical potential (2.2.6).

$$\frac{\partial \phi^-}{\partial t^-} = -\mathbf{u}^- \cdot \nabla \phi^- + \frac{1}{Pe}\nabla^2 \mu^-, \tag{6.1.1}$$

$$\nabla \cdot \mathbf{u}^- = 0, \tag{6.1.2}$$

$$\frac{\partial \mathbf{u}^-}{\partial t^-} = -\mathbf{u}^- \cdot \nabla \mathbf{u}^- - \nabla p^- + \frac{1}{Re_\tau}\nabla^2 \mathbf{u}^- + \frac{3}{\sqrt{8}}\frac{1}{We \cdot Ch}\mu^- \nabla \phi^-, \tag{6.1.3}$$

$$\mu = \phi^{3-} - \phi^- - Ch^2 \nabla^2 \phi^-. \tag{6.1.4}$$

where the Eq. (6.1.4) is the dimensionless chemical potential (2.2.6). The following dimensionless groups appear:

$$Re_\tau = \frac{U_\tau h}{\nu}, \qquad Pe = \frac{U_\tau h}{M\beta}, \qquad We = \frac{\rho U_\tau^2 h}{\sigma}, \qquad Ch = \frac{\xi}{h}. \tag{6.1.5}$$

The shear Reynolds number (Re_τ) is the ratio between inertial forces and viscous forces, the Peclet number (Pe) represents the interface relaxation time, the Weber number (We) is the ratio between inertial forces and the surface tension and the Cahn number (Ch) is the dimensionless capillary width. In our approach, Re_τ, Pe, We and Ch are governing parameters that defined by considering the physical fluid properties, the flow regime, the simulated surface tension and the phase field modelling. Once the shear Reynolds number is fixed, the value of the surface tension is chosen by changing the Weber number. When considering immiscible fluids, the interface thickness depends on the numerical algorithm only, thus the Cahn number can be fixed to the smallest possible value. To obtain results independent from Ch, the Peclet number should be properly chosen: for this reason the scaling proposed by Magaletti *et al.* [73] has been adopted: $Pe \propto Ch^{-1}$. The adoption of a proper scaling between Pe and Ch ensures also a correct description of breakup and coalescence phenomena [140, 113]. Eq. (6.1.1)-(6.1.4) have been solved using a pseudo-spectral algorithm discussed in Chap. 3 and previously adopted in Chap. 5. All the results reported in this section are measured in wall-units "+" obtained by normalizing with U_τ, ρ, ν and ϕ_+.

6.1.1 Simulation parameters

In this work the shear Reynolds number based on the half channel height is $Re_\tau = 150$, leading to a fully developed turbulent flow. A large number of droplets ($n_{d,0} = 256$) of initial diameter $d_0^+ = 60 w.u.$ yielding a volume fraction $\varphi = 0.053$ have been simulated considering wide range of Weber numbers: $We = 0.18 \div 2.8$. The droplet diameter is much larger than the Kolmogorov length scale η_κ^+ at all the positions in the domain: the ratio between the Kolmogorov length scale and the droplet diameter is $0.027 \leq \eta_\kappa^+/d^+ \leq 0.063$. During the simulations the droplet can coalesce, as a result their diameter increases; moreover the breakup events produce daughter droplets always larger than the Kolmogorov length scale. The simulations were run on a $512 \times 256 \times 257$ fixed cartesian grid fine enough to resolve the smallest length scale of the turbulent flow, while the time step $\Delta t^- = 3 \cdot 10^{-2}$ has been chosen to resolve the smallest temporal scales and respond to the numerical stability requirements associated with the grid resolution. The pseudo-spectral scheme adopted can resolve accurately the interfacial layer with a minimum number of three mesh-points [5, 99, 100]. The interface is described by three mesh-points along x and y directions (where a uniform discretization is adopted) and by a minimum number of seven mesh-points along the z direction where a finer non-uniform discretization is adopted (Chebyshev polynomials). With reference to Eq. (2.2.7) the interface thickness (a layer where $-0.9 \leq \phi^+ \leq 0.9$) is fixed choosing $Ch = 0.0185$ and, adopting the scaling law proposed by Magaletti *et al.* [73], the Peclet number is $Pe = 162.2$. The PFM cannot completely fulfil local mass conservation [141]; thanks to the accuracy of the numerical and to the small interface thickness adopted, however, the mass loss is in any case small[1]. A collection of the relevant parameters of each simulation is reported in Tab. 6.1.

---

[1] After the entire simulation ($2 \cdot 10^5$ time-steps, corresponding to ~ 50 channel length covered by the mean flow), losses of volume V^+ (or equivalently of mass m) range from 2% to 10%.

Table 6.1 – Collection of simulation parameters

Simulation	We	Re_τ	Ch	Pe	φ
$WE1$	0.18	150	0.0185	168.2	0.053
$WE2$	0.21	150	0.0185	168.2	0.053
$WE3$	0.25	150	0.0185	168.2	0.053
$WE4$	0.28	150	0.0185	168.2	0.053
$WE5$	0.35	150	0.0185	168.2	0.053
$WE6$	0.71	150	0.0185	168.2	0.053
$WE7$	1.41	150	0.0185	168.2	0.053
$WE8$	2.83	150	0.0185	168.2	0.053

6.2 Droplet-droplet interactions

After a short transient, droplets start to interact and collide, fostered by two distinct effects: the presence of a mean shear, thus regions of the domain with different mean streamwise velocity, and turbulent fluctuations. In general, not every collision results in a coalescence event and, in particular, two leading mechanisms can prevent the coalescence: *i*) turbulent fluctuations that cause a trajectory deviation so that droplets move away from each other before colliding; *ii*) the presence of a thin film between the colliding droplets does not drain rapidly enough causing droplets deformation and bouncing. Supported by a simple scaling analysis, the coalescence can be prevented more efficiently by the turbulent velocity field; as a result coalescence is expected to be the most likely event to observe provided that the two droplets collide. In particular, approximating two droplets as spheres of diameter $d_l > d_s$ with $d_l \sim O(d_s)$ colliding at velocity u_r, their collisional momentum Q_d can be estimated. In a similar way, the momentum of the thin film of fluid that separates two colliding droplets Q_f can be estimated:

$$Q_d = \rho_f \frac{4\pi d_s^3}{3} u_r, \qquad Q_f = \rho_f h_f \frac{\pi \ell_f^2}{4} u_f. \tag{6.2.1}$$

The film is approximated by a thin disk of heigh h_f and diameter ℓ_f while u_f is the characteristic velocity at which the film is drained; following Frostad *et al.* [29], u_f can be estimated adopting the lubrication theory into the film: $u_f \simeq (2\sigma h_f^2)(\mu_f d_s \ell_f)$. Hence, the film-droplet inertial ratio results:

$$\frac{Q_f}{Q_d} \sim \left(\frac{\rho_f}{\rho_d}\right)\left(\frac{d_s}{\ell_f}\right)\left(\frac{u_\tau}{u_r}\right)\left(\frac{Re_\tau}{We}\right)\left(\frac{h_f}{d_s}\right)^3. \tag{6.2.2}$$

In the present simulations, $\rho_f/\rho_d = 1$ and the ratio d_s/ℓ_f can be safely considered as $O(1)$. Since a large number of droplets is dispersed in a three-dimensional turbulent flow, the exact features of every single collision event are difficult to detect. It is possible to roughly estimate u_r as the relative velocity between a pair of nearest neighbours droplets, averaged over all the pairs, for each time step. The ratio $\langle u_\tau/u_r\rangle$ is in general $O(1)$ (slightly decreasing in time) for every set of tested Weber number. We explore regimes Re_τ/We from $O(10^2)$ to $O(10^3)$ while $(h_f/d_s)^3$ varies in time, at least in the initial transient, because droplets increase in volume while they coalesce. However, since h_f is of the order of the interface thickness ($h_c \simeq 4Ch \simeq 0.04$), on average $O(2 \cdot 10^{-6}) \leq \langle (h_f/d_s)^3 \rangle \leq O(\cdot 10^{-4})$. Consequently, the ratio Q_f/Q_d varies from $O(10^{-1})$ to $O(10^{-4})$ meaning that, in average, colliding droplets have larger inertia with respect to the thin fluid film. The local Reynolds number into the film, can be roughly estimated as:

$$Re_f = \frac{\rho_f u_f h_f}{\mu_f} = \frac{Re_\tau^2}{We} \frac{h_f^3}{d_s^2 H}. \tag{6.2.3}$$

Re_f is relatively small at the early stages of the simulations ($O(10^{-2})$ for large We) because of the small droplets diameters but, in general, it is larger because of droplets growth (up to $O(10^1)$ for the largest droplets and the smallest We). Therefore, since droplets inertia is larger with respect to the film inertia and viscous forces into the film play a minor role during drainage, droplets bouncing is likely to be observed only in the early stages of simulations while, most of the time, the coalescence of two colliding droplets is expected. Hence, the only way to prevent coalescence, when droplets are large, is avoiding collision by transport mechanisms. The number of distinct droplets in the channel ($n_d/n_{d,0}$) is shown in Fig. 6.2-a as function of time for different Weber numbers. As expected, $n_d/n_{d,0}$ decreases in time and it stabilizes toward an asymptotic value after a transient. By contrast the average droplet diameter $\langle d \rangle$ increases in time due to the coalescence events and the volume conservation. Two different dynamics of coalescence are observed depending on the Weber number.

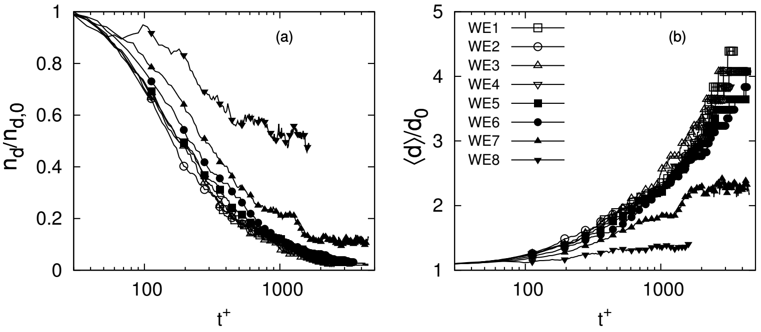

FIGURE 6.2 – Time evolution of the normalized number of droplets $n_d/n_{d,0}$ and normalized droplet averaged diameter $\langle d \rangle/d_0$ varying the Weber number We.

6.2.1 Small Weber number: $We < 1$

For small Weber numbers ($WE1 \div WE6$), a strictly monotonic reduction of the total number of droplets ($n_d/n_{d,0}$) is observed. This trend is possible only if breakups events do not exist and this behaviour is consistent with the balance between inertial forces and surface tension given by $We < 1$. In order to shed some light on the coalescing events, in

Fig. 6.3 the time evolution of a coalescence event (top panels) is compared with the case in which the collision is prevented (bottom panels). The fluctuating streamwise velocity field is rendered on a slice crossing the two droplets. It seems that the coalescence or separation of the droplets is driven by the successive flow regions experienced by the droplets. In the bottom panels, at the beginning, both droplets are experiencing a similar velocity region, as a result their distance is not reduced. After $15t^+$ the front droplet encounters a region of positive velocity fluctuations that drives it apart from the droplet behind. After $30t^+$, the droplets separated by different spanwise velocities, indicating that the large scales turbulent structures encountered are, in this case, preventing the coalescence. It worth noting that in case of no coalescence, the liquid film between the droplets produces only a slightly flattening of the front droplet interface and, proceeding in time, the local shape do not differ much from a spherical shape ($\ell_f < d_s$). In this case, as predicted in the momentum scaling of Sect. 6.2, the film inertia is negligible and the collision dynamics is controlled by the velocity field. On the contrary the initially non homogeneous flow regions encountered by the coalescing droplets (A and B depicted in the top panels), move the droplets closer fostering collision. The fluid film is squeezed by the motion of the droplets and, as a result, large negative streamwise velocity fluctuations ($u'^+ \simeq 3$) can be observed into the film. After $15t^+$ the film is completely drained and the droplets interface collide; after $30t^+$ a large bridge between the droplets is generated. It worth notice that, as proposed by Yang *et al.* [137], the coalescence because the

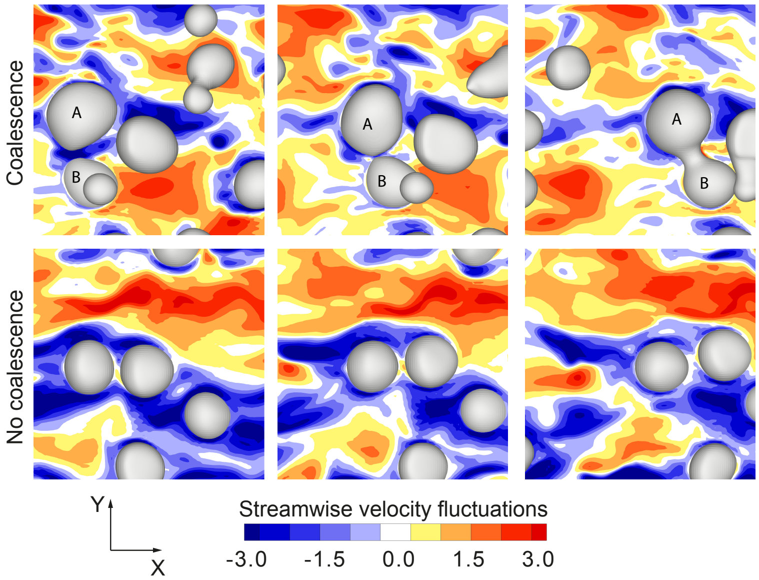

FIGURE 6.3 – Time evolution of two coalescing droplets (top panels) and two non coalescing droplets (bottom panels) taken at time distances of $15t^+$. The streamwise velocity fluctuations u'^+ are rendered over a $x-y$ plane crossing the droplets ($z^+ = 50w.u.$ and $z^+ = 250w.u.$ for the top panels and bottom panels, respectively). The time sequences are taken at the same initial time $390t^+$, at different positions on the computational domain and for simulation $WE1$.

film drainage characteristic time ℓ_f/u_f is smaller than the characteristic collision time h_f/u_r. In fact, in this case $u_f \simeq 3\langle u_r \rangle$, and $h_f \simeq \ell_f$, since no flattening of the droplet is observed. Fig. 6.4 helps to clarify the coalescence driving mechanism: it is evident that the spanwise velocity fluctuations are acting to push the droplets tips close together. Combining top panel of Fig. 6.3 and Fig. 6.4 a coalescing event in a xy plane can be summarized: *i*) the spanwise velocity fluctuations push the droplets closer, *ii*) the film drains in the streamwise direction helped by the local velocity fluctuations; *iii*) the bridge between the droplets forms. Finally, in the early stages ($t^+ < 2000$) the coalescing regime shows a weak dependence from We, while, for $t^+ > 2000$ the number of droplets observed in the asymptotic regime is almost universal. For larger t^+ coalescence becomes a rare event confirming that for larger droplets coalescence is driven by the turbulent mixing that becomes ineffective when the average distance between the droplets is large. [ht!]

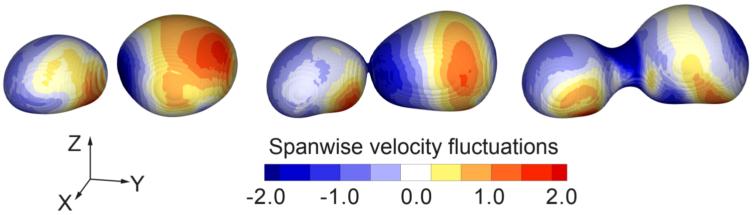

Figure 6.4 – Time evolution of the coalescence process depicted in the top panels of Fig. 6.3. The snapshots are taken at time distances of $15t^+$ and the spanwise velocity fluctuations v'^+ are rendered over the droplets isosurfaces (that are identified by $\phi = 0$).

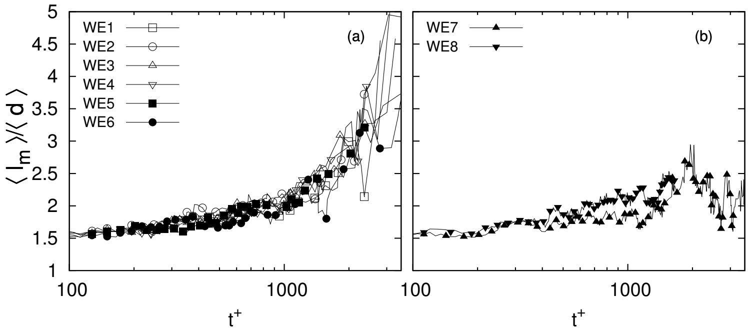

Figure 6.5 – Time evolution of the average minimal distance $\langle l_m \rangle$ normalized by the average droplet diameter $\langle d \rangle$. Small Weber numbers ($WE1 \div WE6$) are reported in panel (a). Large Weber numbers ($WE7$, $WE8$) are reported in panel (b) where the case $We = 0.71$ is also shown for sake of comparison.

Fig. 6.5-a shows the minimal distance between the two closest droplets, averaged over all the droplets pair $\langle l_m \rangle$ and normalized by the average droplet diameter $\langle d \rangle$. In the case of small Weber numbers the distance increases in time, consequently the probability of interaction decreases in time. At large times the minimal distance can be $\langle l_m \rangle / \langle d \rangle \simeq 2 \div 3$, such that droplets are essentially too distant to interact and coalescences are dramatically

reduced.

6.2.2 Large Weber number: $We > 1$

In the case of large We ($WE7$ and $WE8$), $n_d/n_{d,0}$ decreases in time until an asymptotic behaviour is observed. However, if We is larger than a critical value, here $We > 1$, n_d is not decreasing monotonically. Such behaviour is due to the breakups produced by the combined action of mean and turbulent shear stress. As shown in Fig. 6.2-a, local increments of the number of droplets are observed after an early transient in which breakups are rare. Indeed, at this stage ($t^+ < 1000$), droplets are small and the local shear produced by the velocity fluctuations requires large We to produce large deformations, as a result, $n_d/n_{d,0}$ is first dominated by coalescence. Growing in size the droplets can be large enough to be subjected to velocity fluctuations strong enough break them. This behaviour is consistent with the critical stable diameter pointed out by Hinze [42]. After an initial transient that depends on the Weber number, an asymptotic regime (in the statistical sense) is reached and coalescence/breakup events are in a dynamic equilibrium. Droplets generate by breakup are compensate by other coalescences and, as a result, at equilibrium the number of droplets is much larger than that observed in the case of small Weber numbers. For instance, $We = 1.41 \div 2.82$ yield to a steady number of droplets that is from one to two magnitude orders larger than the small Weber number cases Sect. 6.2.1. Fig. 6.6 depict the time evolution of a breakup event; subjected to the local velocity field the droplet loses its initial sphere-like shape and deforms assuming an elongate shape with a neck where the pinch-off will take place. Observing the streamwise velocity fluctuations u'^+ rendered over the droplet surface, it seems that the local velocity field is responsible to create a curvature that will allow the surface tension to complete the breakup. When the concave curvature is produced, the local velocity field that tends to pull apart the thin neck helps the surface tension to finalize the breakup. Fig. 6.5-b shows how the breakup events tend to create an upper bound to $\langle l_m \rangle / \langle d \rangle$; on average the minimal distance between a droplet pair is not larger than a diameter $\langle d \rangle$. Due to the bounded $\langle l_m \rangle / \langle d \rangle$, the probability of droplet-droplet collisions and coalescences is larger. The droplets produced by coalescence can have a diameter larger than the stable size for the given We, resulting in a new breakups. This mechanism is repeated in time, producing the dynamical equilibrium observed in Fig. 6.2-a.

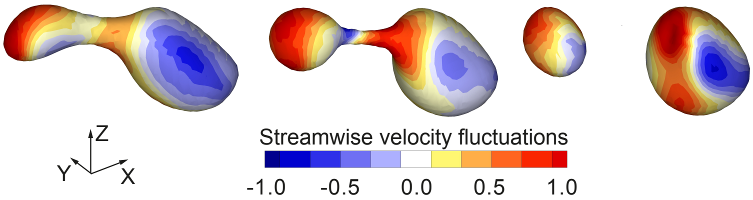

FIGURE 6.6 – Time evolution of a breakup event observed in the $We = 1.41$. The snapshots are taken at time distances of $15t^+$ starting from an initial time of $1170t^+$. The streamwise velocity fluctuations u'^+ are rendered over the droplets isosurfaces.

6.3 Wall-drag modification

The wall-drag modifications produced by the droplets in have been studied focusing on the correlation between the droplets deformability and the wall-drag modifications. Time-independent statistical results have been obtained by time and ensemble averaging (denoted by brackets "$\langle\rangle$"); the time window adopted corresponds to a ~ 24 eddy turnover times $T_e = h/U_\tau$.

6.3.1 Qualitative analysis

Fig. 6.7 and Fig. 6.8 show the detail of one droplet moving in the near wall region: in panels (a) a small Weber number case ($WE1$) is shown and in panels (b) a large Weber number case ($WE6$) is depicted. In Fig. 6.7 the streamwise component of the velocity field relative to the droplet velocity ($\mathbf{u}_r^+ = \mathbf{u}^+ - \mathbf{u}_d^+$) is shown by the contour plot reported on a $x-z$ slice that spans all the channel height ($300w.u.$). The droplets are modified by the turbulent structures encountered in their motion: when the Weber number is small ($We = 0.18$), the small deformations observed are limited to the near wall region and are probably due to the wall mean shear; when the Weber number is large ($We = 0.71$), the deformations are much larger and the droplet assumes an elongated shape that is oriented in the direction of the stream flow. The relative velocity u_r^+ increases reducing We: higher magnitude are measured in the channel center, while the regions of negative u_r^+ shrink toward the walls. This effect is due to the droplet velocity $\mathbf{u}_b^+$ that decreases with We: in this particular case the less deformable droplet ($WE1$) has a mean velocity $u_d^+ = 13.5$, while the more deformable droplet ($WE6$) has an higher mean velocity $u_d^+ = 16.7$. Droplets with small deformability are slowed down by the near wall velocity field where they move in a negative relative velocity region, as observed in the fluid

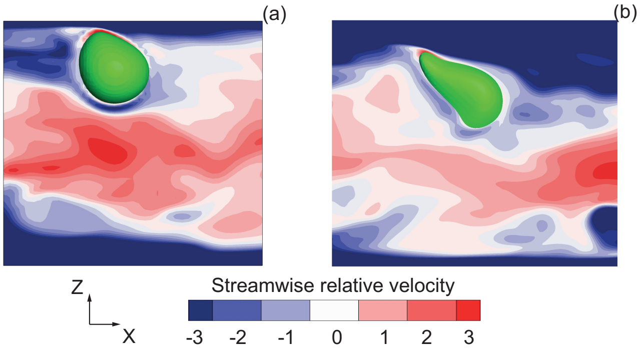

FIGURE 6.7 – Detail of the near-wall motion of a droplet for different Weber numbers: (a) simulation $WE1$, (b) simulation $WE6$. The contour plot of the streamwise velocity u_r^+ relative to the droplet streamwise velocity u_d^+ is depicted on a $x-z$ plane passing across the droplet. The droplet interface is located by the iso-surface $\phi = 0$ and is rendered in green. The entire computational domain along the wall-normal direction z is shown, while only a portion of $\sim 300w.u.$ is shown along the streamwise direction.

regions near the droplet of (Fig. 6.7-a). The shape of droplets with large deformability show deformations that correlate with the relative velocity field: the droplet seems to be forced and deformed by two opposite sign flow regions (Fig. 6.7-b): a region of positive u_r^+ acting on its back side and a region of negative u_r^+ insisting on its front side. As a result the flow field modifications are larger the smaller is the Weber number and droplets with large deformability can be more easily deformed by the surrounding flow field. In

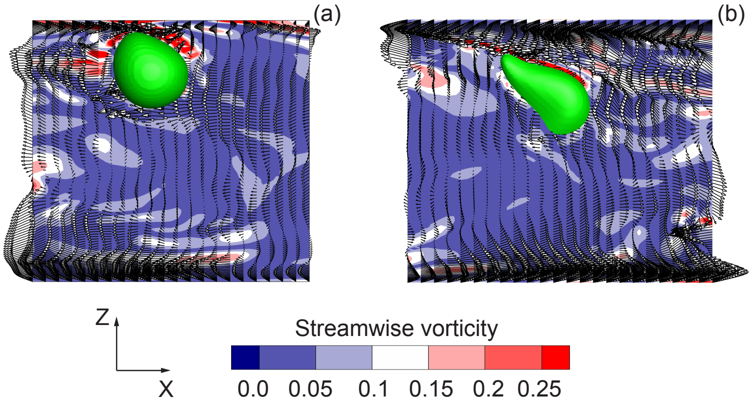

FIGURE 6.8 – Detail of the near-wall motion of a droplet for different Weber numbers: (a) simulation $WE1$, (b) simulation $WE6$. The contour plot of the streamwise vorticity component ω_x^+ is depicted on a $x - z$ plane passing across the droplet and the vector plot of the velocity fluctuations $\mathbf{u}$ are superposed on it. The droplet interface is located by the iso-surface $\phi = 0$ and is rendered in green. The entire computational domain along the wall-normal direction z is shown, while only a portion of $\sim 300 w.u.$ is shown along the streamwise direction.

Fig. 6.8 the contour plot of the streamwise vorticity component (ω_x^+) is reported on a x-z plane spans all the channel height ($300 w.u.$). The vector plot of the velocity fluctuations $\mathbf{u}'^+$ is superposed on the same plane. The effect of produced by the presence of droplets with small deformability ($WE1$) is highlighted by the high vorticity regions observed in the back side of the droplet: the droplet moves faster than the near-wall fluid, as a result a its back side is characterized by local intense vortical regions. By contrast the vorticity magnitude in the proximity of the droplet with large deformability is almost comparable to that measured in the channel center.

6.3.2 Velocity statistics

To analyse the effects of the droplets dispersed in the turbulent channel flow, first the the streamwise mean velocity $\langle u^+ \rangle$ is measured. Since the simulations are run with fixed average pressure gradient, the flow rate depends on the shear stress at the wall; small mean velocity fluctuations are ruled out by the ensemble and time averaging procedure. Fig. 6.9 shows that the mean streamwise velocity profile is shifted down when decreasing the Weber number (and thus the droplets deformability). Compared with the turbulence wall law, $\langle u^+ \rangle$ is reduced when We is small ($WE1 \div WE4$) and the resulting velocity profile is characterized by a logarithmic region that is shifted down and reduced in slope.

In agreement with the observations of Lu *et al.* [70], droplets with small deformability produce Drag Enhancement (DE). On the contrary, when the We is large (simulations $WE5 \div WE8$), $\langle u^+ \rangle$ is slightly increased with respect to the single phase flow, but no significant Drag Reduction (DR) is observed. In order to correlate DE and DR with We and with the droplet deformability, the averaged friction coefficient C_f has been computed:

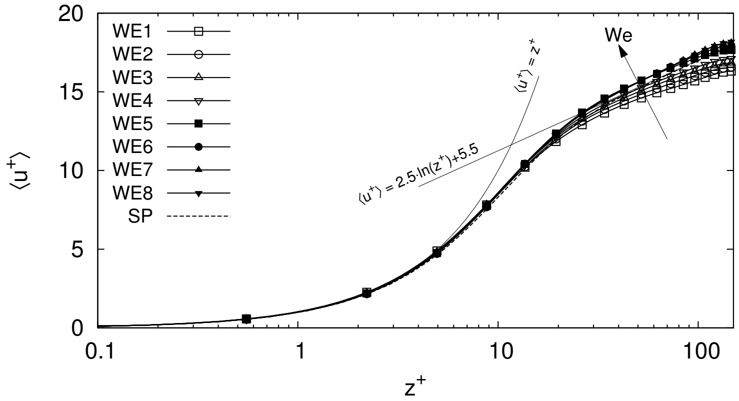

FIGURE 6.9 – Mean streamwise velocity profile $\langle u^+ \rangle$ along the wall-normal direction z^+ for different Weber numbers. Arrow points in the increasing Weber number direction (increasing deformability). The average streamwise velocity decreases reducing the droplets deformability (reducing We) with respect to the single phase profile SP.

$$C_f = \frac{\tau_w}{\frac{1}{2}\rho\langle u_0 \rangle^2}, \tag{6.3.1}$$

where $\langle u_0 \rangle$ is the flow average bulk velocity. Fig. 6.10-a shows the friction coefficient normalized with its value measured for a single phase flow $C_{f,s}$; plain dots refer to simulations where DE is observed, while filled dots are cases of no DE (or slight DR). The friction coefficient increases up to 11% for the smaller Weber number (simulation $WE1$), while a slight reductions of $1\% \div 2\%$ is observed for large Weber numbers (simulations $WE6 \div WE8$). The DE observed in [70] for small Weber number bubbles was addressed to the flow obstruction produced by droplets with streamwise velocity smaller than the surrounding fluid. Based on this evidence the average droplets velocity u_d^+ has been investigated. Fig. 6.10-b shows that increasing the Weber number, the droplet average velocity increases reaching an almost uniform value when the DE vanishes (filled dots); this result confirms the qualitative behaviour observed in Fig. 6.7 and it is in agreement with [70]. In particular, the droplet average velocity seems to correlate well with the inverse of the friction factor represented by the dashed line in Fig. 6.10-b, confirming that the DE observed for small Weber number droplets is likely due to the slip velocity between the droplets and the surrounding fluid. In particular, since the droplets average diameter $\langle d \rangle$ increases in time (see Fig. 6.2-b), the droplets motion can easily decorrelate from the flow. As a result the DR mechanism [70] cannot be observed.

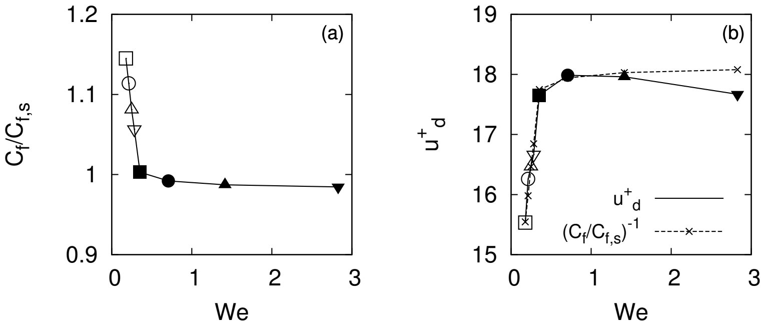

FIGURE 6.10 – Average friction coefficient C_f normalized with the single phase flow friction coefficient $C_{f,s}$ for different Weber numbers (panel a). Droplets average velocity u_d^+ for different Weber numbers (panel b). Plain dots refer to simulations where DE is observed; filled dots refer to simulations with no DE. The normalized friction coefficient increases reducing the droplets deformability (reducing We), while the droplets average velocity reduces reducing the deformability. The droplets average velocity correlate with the inverse of the friction factor (dashed line).

6.3.3 Vorticity fluctuations statistics

In a flow where large and highly deformable bubbles are dispersed, the DR is mainly due to the streamwise vorticity cancelling produced by the bubble motion in the near-wall region [70, 128]. Fig. 6.11 shows the near-wall behaviour of the Root Mean Square (RMS) of the streamwise vorticity fluctuations $\langle RMS(\omega_x'^+)\rangle$; when We is small (simulations $WE1$ and $WE2$), the vorticity fluctuations at the wall are increased with respect to the single phase flow, while, when We is large (simulations $WE5 \div WE8$), $\langle RMS(\omega_x'^+)\rangle$

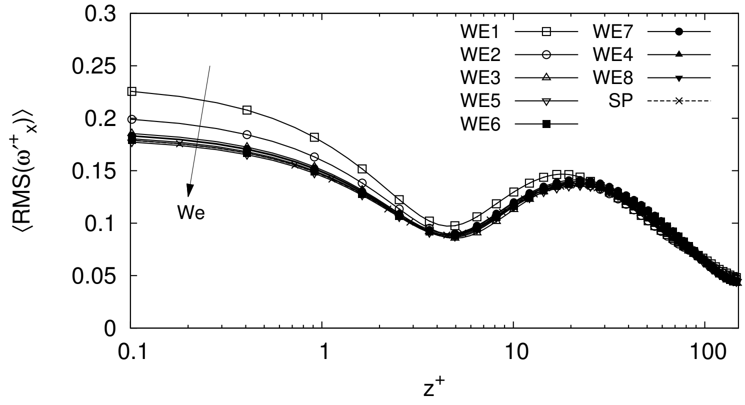

FIGURE 6.11 – Root Mean Square of the streamwise vorticity component fluctuations $\langle \omega_x'^+\rangle$ along the wall-normal direction z^+. Arrow points in the increasing Weber number direction (increasing deformability). In the near-wall region, the average streamwise vorticity fluctuations increase reducing the droplets deformability (reducing We) with respect to the single phase profile SP.

collapses over the single phase flow vorticity. Thus the presence of small We droplets is responsible for the enhancement of the near-wall streamwise vorticity fluctuations, while large We is not affecting $\langle RMS(\omega_x'^+)\rangle$. In Fig. 6.12 the RMS of the spanwise vorticity fluctuations $\langle RMS(\omega_y'^+)\rangle$ is shown; in near-wall region there is an enhancement of $\langle RMS(\omega_y'^+)\rangle$ that is larger the smaller is We and the profiles collapse over the single phase flow curve when the We is large. In this region the wall-normal vorticity component (not displayed for brevity) has no major deviations from the single phase behaviour. In the channel center (in a region from $70w.u.$ to $230w.u.$) the spanwise vorticity fluctuations are increased reducing We; this behaviour is observed also in the wall-normal vorticity component (not displayed for brevity) which is affected in a similar way, but on a wider region ($40w.u.$ to $260w.u.$). The vorticity behaviour suggests that when a droplet moves from the channel center towards the wall, it transports an higher streamwise velocity in the near wall region producing an increment of the near wall vorticity components. At the same time the droplet velocity is slowed down thus, when the droplet is transported again towards the center of the channel, it introduces a smaller streamwise velocity in that region. As a result the droplet is accelerated and the local vorticity fluctuations are enhanced. This mechanism is much more effective when the droplet behaves like a rigid body: once the velocity in some regions of the droplet surface are slowed down, also the neighbourhood regions velocity are reduced because of the limited displacements allowed by the high surface tension. On the contrary when the droplet deformability is large, the interface can deform and adapt to the velocity difference in different regions, introducing a smaller obstruction to the flow (Fig. 6.7-a).

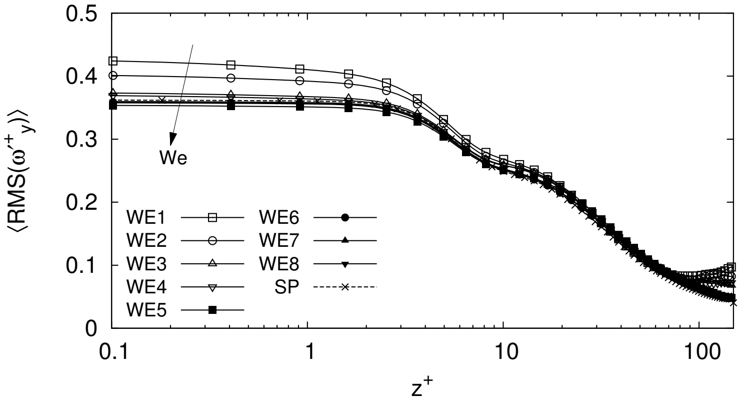

FIGURE 6.12 – Root Mean Square of the spanwise vorticity component fluctuations $\langle\omega_y'^+\rangle$ along the wall-normal direction z^+. Arrow points in the increasing Weber number direction (increasing deformability). In the near-wall region, the average spanwise vorticity fluctuations increase reducing the droplets deformability (reducing We) with respect to the single phase profile SP. Also in the channel center ($70w.u.$ to $150w.u.$) a similar behaviour is observed.

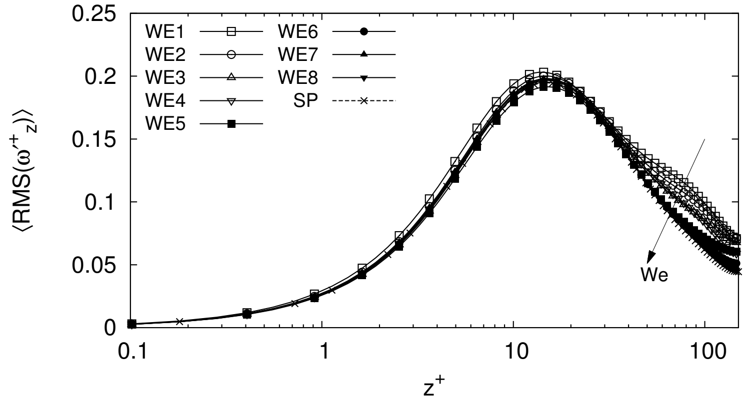

FIGURE 6.13 – Root Mean Square of the wall-normal vorticity component fluctuations $\langle \omega_z'^{+} \rangle$ along the wall-normal direction z^+. Arrow points in the increasing Weber number direction (increasing deformability). In the channel center ($40 w.u.$ to $150 w.u.$), the wall-normal vorticity fluctuations increase reducing the droplets deformability (reducing We) with respect to the single phase profile SP. Near the wall no significant modifications are observed.

6.4 Conclusions

In this chapter the behaviour of a swarm of large deformable and coalescing droplets in wall-bounded turbulence is examined. Droplet-droplet interactions and the wall-drag modifications are investigated exploring a wide range of Weber numbers. The deformability is a leading parameter in determining the coalescence rate and the possibility of breakup of the droplets swarm. When $We < 1$, the coalescence rate is almost universal and no breakups are observed. In this regime the number of droplets reaches an asymptotic value that is due to the increased distance between the droplets. When $We > 1$ different coalescence rates are observed and breakup phenomena can be detected. Due to the breakups, the droplet distance cannot increase over an upper limit and coalescences are always possible. As a result a dynamical equilibrium between coalescences and breakups is observed. The presence of the droplets produces an increment of the wall drag that decreases with the droplet deformability: significant DE is produced by the less deformable droplets, while these effects reduce increasing the deformability. When the deformability is sufficiently large, no DE is observed and an almost negligible DR is produced. The analysis of the droplet average velocity and of the vorticity fluctuations suggest that the DE is likely due to the droplet slip velocity. The absence of the vorticity cancelling can be explained keeping into account the differences between the physical system considered here and the system considered by [70] and [128]: the inertia of the droplets considered in this work is much larger because of their density and their diameter, thus the droplets can easily decorrelate from the vortical structures encountered. As a result the droplets do not produce the near-wall streamwise vorticity cancelling and they act as a flow obstruction when their slip velocity increases.

Conclusions and further developments

In this work the effects produced by the dispersion of large deformable droplets in wall bounded turbulence have been investigated focusing on the role of the droplet deformability. Many experimental investigations pointed out that the dispersion of large deformable bubbles can produce significant modifications of the turbulence features and in particular of the wall shear stress, that yields to Drag Reduction (DR) or Drag Enhancement (DE) phenomena. In spite of the large practical relevance of these effects, a clear knowledge of the mechanisms underpinning the turbulence modifications is still missing. The few available detailed investigations of turbulence-interface interactions emphasized the central role of the bubbles deformability in the wall turbulence modification. Moreover it seems that when deformable bodies (bubbles or droplets) lighter than the surrounding fluid are dispersed, DR is always achieved. On the contrary increasing the density of the deformable body to values comparable with that of the surrounding fluid, both DR or DE is obtained depending on the deformability (governed the surface tension). In order to further clarify the role of the deformability on the wall turbulence modifications produced by the dispersion of large deformable droplets in turbulence, in this work the problem has been simplified neglecting the density differences and the viscosity differences between the droplets and the external flow, considering only the surface tension σ. In this way the described physical system is governed by two leading phenomena: *i)* droplet deformability that is controlled by the surface tension (and the Weber number); *ii)* droplet inertia that is comparable to that of the surrounding fluid. In Chap. 5 the momentum transfer at the interface of a large deformable droplet released in turbulence has been analysed. The modifications of the near-interface flow field have been quantified and correlated with the the Weber number (that is proportional to the average droplet deformability). The velocity fluctuations relative to the droplet center of mass, measured at the droplet interface have been analysed in terms of interface-normal and interface-tangential components. The interface-normal components are reduced reducing the deformability, whereas the interface-tangential components increase reducing the deformability. This behaviour is likely due to the presence of wall-blocking effects [87, 68, 122] that yield to a deviation of the interface-normal components toward the interface-tangential direction. The presence of the interface produces a deviation of the surrounding velocity field, that results in a vorticity generation dependent on the surface tension and in a damping of the turbulence intensity near the interface. These effects are experienced at larger distances from the interface increasing the surface tension. Furthermore the turbulent features observed at the surface of the droplet show similarities to those observed for solid walls in free-stream flows [45]. Responsible for the wall blocking effect is the local normal stress $\tau_n = \sigma/\bar{r} \cdot \mathbf{n}$ that arises at the droplet interface because of the surface tension and the finite curvature radius $\bar{r}$. A first effect is due to the dependency of τ_n on the surface tension: the wall-blocking effects increase when We is reduced and, in turn, intercomponent exchanges are larger for smaller We. A second effect is related to the normal stress dependency on the local deformations: large and energetic structures impacting on the interface act to reduce the local curvature, corresponding to a reduction of τ_n. The effectiveness of this mechanism is likely due to the inertia of the droplet that act obstructing the flow motion, producing a wall-blocking effect that is modulated by the surface tension. As a result the flow field modifications in proximity of the droplet interface depend on the droplet deformability. In Chap. 6 the behaviour of a swarm of large deformable and coalescing droplets in wall-bounded turbulence is examined. Droplet-droplet interactions and the wall-drag modifications are investigated exploring a wide range of Weber numbers. The deformability is a leading parameter in determining the coalescence rate and the possibility of breakup of the droplets swarm. When $We < 1$, the coalescence rate is almost universal and no breakups are observed. In this regime the number of droplets reaches an asymptotic value that is due to the increased distance between the droplets. When $We > 1$ different coalescence rates are observed and breakup phenomena can be detected. Due to the breakups, the droplet distance cannot increase over an upper limit and coalescences are made possible. As a result a dynamical equilibrium between coalescences and breakups is observed. The most evident effect produced by the droplets on the flow field is a significant increment of the wall drag (DE) that is measured through a reduction of the streamwise average velocity. The effect decreases with the droplet deformability: significant DE is produced by the less deformable droplets, while these effects reduce increasing the deformability. When the deformability is sufficiently large, no DE is observed and an almost negligible DR is produced. The analysis of the droplet average velocity and of the vorticity fluctuations suggests that the DE is likely due to the droplet slip velocity, in fact the droplet average velocity is reduced reducing We. This result is confirmed by the qualitative correlation between the average droplets velocity and the inverse of the average friction coefficient. An important feature observed in this analysis is the absence of the vorticity cancelling that is the source of DR in the work of Lu *et al.* [70]. The apparent contrast can be explained keeping into account the differences between the physical system considered here and the system considered by [70] and [128]: the inertia of the droplets considered in this work is much larger because of their inertia and diameter, thus they can easily decorrelate from the vortical structures encountered, increasing the flow obstruction produced by the slip velocity and, in fact, avoiding the droplets to couple with the near-wall vortical structures. As a results the necessary conditions for the DR [70] are not recovered. The results of this work confirm that the role of deformability is a central factor in the turbulence modifications produced by large droplets. The investigation have also highlighted a particular aspect of the dispersion of deformable bodies in turbulence that requires further investigations: the droplet inertia. The most important difference between the droplets and bubbles is the difference of density, that yields to a larger inertia in the cases of droplets. When air bubbles dispersed in a water flow are considered [128] the density ratio is large ($\rho_f/\rho_d = 1000$) and large DR is observed. Increasing the bubbles density of two magnitude orders ($\rho_f/\rho_d = 10$), both DR and DE can be achieved depending on the deformability [70]. When the two fluids have the same density ($\rho_f/\rho_d = 1$), as in the physical system considered in this work, no DR is observed but significant DE is measured. From this simple analysis it is immediate to connect the increased inertia as a limiting factor to the DR, thus a systematic analysis of the droplets density effects can push further ahead the knowledge on the DR mechanisms. .

Bibliography

[1] D. M. Anderson, G. B. McFadden, and A. A. Wheeler. Diffuse-interface methods in fluid mechanics. *Annual Review of Fluid Mechanics*, 30(1):139–165, 1998.

[2] S. Arcidiacono, I. V. Karlin, J. Mantzaras, and C. E. Frouzakis. Lattice boltzmann model for the simulation of multicomponent mixtures. *Physical Review E*, 76(4):046703, 2007.

[3] U. M. Ascher, S. J. Ruuth, and B. T. R. Wetton. Implicit-explicit methods for time-dependent partial differential equations. *SIAM Journal on Numerical Analysis*, 32(3):797–823, 1995.

[4] P. Asinari. Lattice boltzmann scheme for mixture modeling: Analysis of the continuum diffusion regimes recovering maxwell-stefan model and incompressible navier-stokes equations. *Physical Review E*, 80(5):056701, 2009.

[5] V. E. Badalassi, H. D. Ceniceros, and S. Banerjee. Computation of multiphase systems with phase field models. *Journal of Computational Physics*, 190(2):371–397, 2003.

[6] G. K. Batchelor. *An introduction to fluid dynamics.* Cambridge University Press, 1967.

[7] R. Benzi, L. Biferale, M. Sbragaglia, S. Succi, and F. Toschi. Mesoscopic modeling of a two-phase flow in the presence of boundaries: the contact angle. *Physical Review E*, 74(2):021509, 2006.

[8] R. Benzi, E. S. C. Ching, E. De Angelis, and I. Procaccia. Comparison of theory and direct numerical simulations of drag reduction by rodlike polymers in turbulent channel flows. *Physical Review E*, 77(4):046309, 2008.

[9] R. Benzi, M. Sbragaglia, S. Succi, M. Bernaschi, and S. Chibbaro. Mesoscopic lattice boltzmann modeling of soft-glassy systems: Theory and simulations. *The Journal of Chemical Physics*, 131(10):104903–104903, 2009.

[10] R. Benzi, S. Succi, and M. Vergassola. The lattice boltzmann equation: theory and applications. *Physics Reports*, 222(3):145–197, 1992.

[11] P. L. Bhatnagar, E. P. Gross, and M. Krook. A model for collision processes in gases. i. small amplitude processes in charged and neutral one-component systems. *Physical review*, 94(3):511, 1954.

[12] J. P. Boyd. *Chebyshev and Fourier spectral methods.* Courier Dover Publications, 2001.

[13] A. J. Briant, A. J. Wagner, and J. M. Yeomans. Lattice boltzmann simulations of contact line motion. i. liquid-gas systems. *Physical Review E*, 69(3):031602, 2004.

[14] A. J. Briant and J. M. Yeomans. Lattice boltzmann simulations of contact line motion. ii. binary fluids. *Physical Review E*, 69(3):031603, 2004.

[15] J. W. Cahn and J. E. Hilliard. Free energy of a nonuniform system. i. interfacial free energy. *The Journal of Chemical Physics*, 28:258, 1958.

[16] J. W. Cahn and J. E. Hilliard. Free energy of a nonuniform system. iii. nucleation in a two-component incompressible fluid. *The Journal of Chemical Physics*, 31:688, 1959.

[17] S. L. Ceccio. Friction drag reduction of external flows with bubble and gas injection. *Annual Review of Fluid Mechanics*, 42:183–203, 2010.

[18] A. Celani, A. Mazzino, P. Muratore-Ginanneschi, and L. Vozella. Phase-field model for the rayleigh-taylor instability of immiscible fluids. *Journal of Fluid Mechanics*, 622:115, 2009.

[19] R. Chella and J. Viñals. Mixing of a two-phase fluid by cavity flow. *Physical Review E*, 53(4):3832, 1996.

[20] S. Chen and G. D. Doolen. Lattice boltzmann method for fluid flows. *Annual review of fluid mechanics*, 30(1):329–364, 1998.

[21] S. S. Chikatamarla and I. V. Karlin. Entropy and galilean invariance of lattice boltzmann theories. *Physical Review Letters*, 97(19):190601, 2006.

[22] S. S. Chikatamarla and I. V. Karlin. Lattices for the lattice boltzmann method. *Physical Review E*, 79(4):046701, 2009.

[23] A. Cristea and V. Sofonea. Reduction of spurious velocity in finite difference lattice boltzmann models for liquid–vapor systems. *International Journal of Modern Physics C*, 14(09):1251–1266, 2003.

[24] C. T. Crowe, J. D. Schwarzkopf, M. Sommerfeld, and Y. Tsuji. *Multiphase flows with droplets and particles.* CRC press, 2011.

[25] S. S. Dearing, M. Campolo, A. Capone, and A. Soldati. Phase discrimination and object fitting to measure fibers distribution and orientation in turbulent pipe flows. *Experiments in Fluids*, 54(1):1–14, 2013.

[26] S. P. G. Dinavahi, K. S. Breuer, and L. Sirovich. Universality of probability density functions in turbulent channel flow. *Physics of Fluids*, 7:1122, 1995.

[27] H. Ding, P. D. M. Spelt, and C. Shu. Diffuse interface model for incompressible two-phase flows with large density ratios. *Journal of Computational Physics*, 226(2):2078–2095, 2007.

[28] R. P. Fedkiw, T. Aslam, B. Merriman, and S. Osher. A non-oscillatory eulerian approach to interfaces in multimaterial flows (the ghost fluid method). *Journal of Computational Physics*, 152(2):457–492, 1999.

[29] JM Frostad, J Walter, and LG Leal. A scaling relation for the capillary-pressure driven drainage of thin films. *Physics of Fluids (1994-present)*, 25(5):052108, 2013.

[30] R. Gatignol and R. Prud'homme. *Mechanical and thermodynamical modeling of fluid interfaces*, volume 58. World Scientific, 2001.

[31] A. Giacomello, S. Meloni, M. Chinappi, and C. M. Casciola. Cassie–baxter and wenzel states on a nanostructured surface: Phase diagram, metastabilities, and transition mechanism by atomistic free energy calculations. *Langmuir*, 28(29):10764–10772, 2012.

[32] J. W. Gibbs. On the equilibrium of heterogeneous substances. *American Journal of Science*, (96):441–458, 1878.

[33] F. Gibou, L. Chen, D. Nguyen, and S. Banerjee. A level set based sharp interface method for the multiphase incompressible navier–stokes equations with phase change. *Journal of Computational Physics*, 222(2):536–555, 2007.

[34] E. Goldman and L. Sirovich. Equations for gas mixtures. *Physics of Fluids*, 10:1928, 1967.

[35] E. P. Gross and E. A. Jackson. Kinetic models and the linearized boltzmann equation. *Physics of Fluids*, 2:432, 1959.

[36] J. D. Gunton, M. San Miguel, P. S. Sahni, C. Domb, and J. L. Lebowitz. *Phase transitions and critical phenomena.* Academic, New York, 1983.

[37] Z. Guo, C. Zheng, and B. Shi. Force imbalance in lattice boltzmann equation for two-phase flows. *Physical Review E*, 83(3):036707, 2011.

[38] B. B. Hamel. Kinetic model for binary gas mixtures. *Physics of Fluids*, 8:418, 1965.

[39] B. B. Hamel. Two-fluid hydrodynamic equations for a neutral, disparate-mass, binary mixture. *Physics of Fluids*, 9:12, 1966.

[40] X. He and G. D. Doolen. Thermodynamic foundations of kinetic theory and lattice boltzmann models for multiphase flows. *Journal of Statistical Physics*, 107(1-2):309–328, 2002.

[41] X. He, X. Shan, and G. D. Doolen. Discrete boltzmann equation model for nonideal gases. *Physical Review E*, 57(1):R13, 1998.

[42] J. O. Hinze. Fundamentals of the hydrodynamic mechanism of splitting in dispersion processes. *AIChE J.*, 1:289–295, 1955.

[43] C. W. Hirt and B. D. Nichols. Volume of fluid (vof) method for the dynamics of free boundaries. *Journal of computational physics*, 39(1):201–225, 1981.

[44] P. C. Hohenberg and B. I. Halperin. Theory of dynamic critical phenomena. *Reviews of Modern Physics*, 49(3):435, 1977.

[45] J. C. R. Hunt and J. M. R. Graham. Free-stream turbulence near plane boundaries. *Journal of Fluid Mechanics*, 84(02):209–235, 1978.

[46] J. C. R. Hunt, A. A. Wray, and P. Moin. Eddies, streams, and convergence zones in turbulent flows. In *Studying Turbulence Using Numerical Simulation Databases, 2*, volume 1, pages 193–208, 1988.

[47] J. Hyväluoma and J. Harting. Slip flow over structured surfaces with entrapped microbubbles. *Physical review letters*, 100(24):246001, 2008.

[48] D. Jacqmin. Calculation of two-phase navier–stokes flows using phase-field modeling. *Journal of Computational Physics*, 155(1):96–127, 1999.

[49] D. Jamet, D. Torres, and J. U. Brackbill. On the theory and computation of surface tension: the elimination of parasitic currents through energy conservation in the second-gradient method. *Journal of Computational Physics*, 182(1):262–276, 2002.

[50] Guang-Shan Jiang and Danping Peng. Weighted eno schemes for hamilton–jacobi equations. *SIAM Journal on Scientific computing*, 21(6):2126–2143, 2000.

[51] D. D. Kale and A. B. Metzner. Turbulent drag reduction in dilute fiber suspensions: Mechanistic considerations. *AIChE Journal*, 22(4):669–674, 1976.

[52] K. Kawasaki. Kinetic equations and time correlation functions of critical fluctuations. *Annals of Physics*, 61(1):1–56, 1970.

[53] V. V. Khatavkar, P. D. Anderson, and H. E. H. Meijer. On scaling of diffuse–interface models. *Chemical Engineering Science*, 61(8):2364–2378, 2006.

[54] J. Kim, P. Moin, and R. Moser. Turbulence statistics in fully developed channel flow at low reynolds number. *Journal of Fluid Mechanics*, 177(1):133–166, 1987.

[55] J. S. Kim and J. Lowengrub. Phase field modeling and simulation of three-phase flows. *Interfaces and free boundaries*, 7(4):435, 2005.

[56] Y. Kodama, A. Kakugawa, T. Takahashi, and H. Kawashima. Experimental study on microbubbles and their applicability to ships for skin friction reduction. *International Journal of Heat and Fluid Flow*, 21(5):582–588, 2000.

[57] D. J. Korteweg. Sur la forme que prennent les equations du mouvements des fluides si lon tient compte des forces capillaires causees par des variations de densite considerables mais continues et sur la theorie de la capillarite dans lhypoth‘ese dune variation continue de la densite. *Archives Neerlandaises des Sciences Exactes et Naturelles*, 6:1–24, 1901.

[58] A. L. Kupershtokh, D. A. Medvedev, and D. I. Karpov. On equations of state in a lattice boltzmann method. *Computers & Mathematics with Applications*, 58(5):965–974, 2009.

[59] D. Lakehal, M. Meier, and M. Fulgosi. Interface tracking towards the direct simulation of heat and mass transfer in multiphase flows. *International Journal of Heat and Fluid Flow*, 23(3):242–257, 2002.

[60] H. Lamb. *Hydrodynamics Cambridge University Press.* Cambridge University Press, 1932.

[61] A. G. Lamorgese and R. Mauri. Nucleation and spinodal decomposition of liquid mixtures. *Physics of Fluids*, 17:034107, 2005.

[62] A. G. Lamorgese and R. Mauri. Diffuse-interface modeling of phase segregation in liquid mixtures. *International Journal of Multiphase Flow*, 34(10):987–995, 2008.

[63] A. G. Lamorgese, D. Molin, and R. Mauri. Phase field approach to multiphase flow modeling. *Milan Journal of Mathematics*, 79(2):597–642, 2011.

[64] R. Latorre. Ship hull drag reduction using bottom air injection. *Ocean engineering*, 24(2):161–175, 1997.

[65] R. Latorre, A. Miller, and R. Philips. Micro-bubble resistance reduction on a model ses catamaran. *Ocean engineering*, 30(17):2297–2309, 2003.

[66] G. L. Leal. *Advanced transport phenomena: fluid mechanics and convective transport processes.* Cambridge University Press, 2007.

[67] T. Lee and P. Fischer. Eliminating parasitic currents in the lattice boltzmann equation method for nonideal gases. *Physical Review E*, 74(4):046709, 2006.

[68] Z. Li and F. A. Jaberi. Turbulence-interface interactions in a two-fluid homogeneous flow. *Physics of Fluids*, 21:095102, 2009.

[69] J. Lowengrub and L. Truskinovsky. Quasi–incompressible cahn–hilliard fluids and topological transitions. *Proceedings of the Royal Society of London. Series A: Mathematical, Physical and Engineering Sciences*, 454(1978):2617–2654, 1998.

[70] J. Lu, A. Fernández, and G. Tryggvason. The effect of bubbles on the wall drag in a turbulent channel flow. *Physics of Fluids*, 17:095102, 2005.

[71] L. S. Luo and S. S. Girimaji. Lattice boltzmann model for binary mixtures. *Physical Review E*, 66(3):035301, 2002.

[72] L. S. Luo and S. S. Girimaji. Theory of the lattice boltzmann method: two-fluid model for binary mixtures. *Physical Review E*, 67(3):036302, 2003.

[73] F. Magaletti, F. Picano, M. Chinappi, L. Marino, and C. M. Casciola. The sharp-interface limit of the cahnhilliard/navierstokes model for binary fluids. *Journal of Fluid Mechanics*, 714:95–126, 2013.

[74] N. S. Martys, X. Shan, and H. Chen. Evaluation of the external force term in the discrete boltzmann equation. *Physical Review E*, 58(5):6855–6857, 1998.

[75] R. Mauri, R. Shinnar, and G. Triantafyllou. Spinodal decomposition in binary mixtures. *Physical Review E*, 53(3):2613, 1996.

[76] J. C. Maxwell. Capillary action. *Encyclopaedia Britannica*, 5, 1876.

[77] J. Meng and Y. Zhang. Gauss-hermite quadratures and accuracy of lattice boltzmann models for nonequilibrium gas flows. *Physical Review E*, 83(3):036704, 2011.

[78] D. M. Mitrinović, A. M. Tikhonov, M. Li, Z. Huang, and M. L. Schlossman. Noncapillary-wave structure at the water-alkane interface. *Physical Review Letters*, 85(3):582, 2000.

[79] P. Moin and K. Mahesh. Direct numerical simulation: a tool in turbulence research. *Annual Review of Fluid Mechanics*, 30(1):539–578, 1998.

[80] D. Molin and R. Mauri. Enhanced heat transport during phase separation of liquid binary mixtures. *Physics of Fluids*, 19:074102, 2007.

[81] D. Molin and R. Mauri. Spinodal decomposition of binary mixtures with composition-dependent heat conductivities. *Chemical Engineering Science*, 63(9):2402–2407, 2008.

[82] Y. Murai, H. Fukuda, Y. Oishi, Y. Kodama, and F. Yamamoto. Skin friction reduction by large air bubbles in a horizontal channel flow. *International journal of multiphase flow*, 33(2):147–163, 2007.

[83] X. Nie, X. Shan, and H. Chen. Thermal lattice boltzmann model for gases with internal degrees of freedom. *Physical Review E*, 77(3):035701–035701, 2008.

[84] J. Min Park, R. Mauri, and P. D. Anderson. Phase separation of viscous ternary liquid mixtures. *Chemical Engineering Science*, 80:270–278, 2012.

[85] J. S. Paschkewitz, Y. V. E. S. Dubief, C. D. Dimitropoulos, E. S. G. Shaqfeh, and P. Moin. Numerical simulation of turbulent drag reduction using rigid fibres. *Journal of Fluid Mechanics*, 518(10):281–317, 2004.

[86] P. Perlekar, L. Biferale, M. Sbragaglia, S. Srivastava, and Federico F. Toschi. Droplet size distribution in homogeneous isotropic turbulence. *Physics of Fluids (1994-present)*, 24(6):065101, 2012.

[87] B. Perot and P. Moin. Shear-free turbulent boundary layers. part 1. physical insights into near-wall turbulence. *Journal of Fluid Mechanics*, 295:199–227, 1995.

[88] P. C. Philippi, L. A. Hegele, L. O. E. Dos Santos, and R. Surmas. From the continuous to the lattice boltzmann equation: The discretization problem and thermal models. *Physical Review E*, 73(5):056702, 2006.

[89] S. D. Poisson. *Nouvelle théorie de l'action capillaire.* Bachelier père et fils, 1831.

[90] Stephen B Pope. *Turbulent flows.* Cambridge university press, 2000.

[91] I. Procaccia, V. S. Lvov, and R. Benzi. Colloquium: Theory of drag reduction by polymers in wall-bounded turbulence. *Reviews of Modern Physics*, 80(1):225–247, 2008.

[92] D. Qian, J.B. McLaughlin, K. Sankaranarayanan, S. Sundaresan, and K. Kontomaris. Simulation of bubble breakup dynamics in homogeneous turbulence. *Chemical Engineering Communications*, 193:1038–1063, 2006.

[93] L. Rayleigh. Xx. on the theory of surface forces.ii. compressible fluids. *The London, Edinburgh, and Dublin Philosophical Magazine and Journal of Science*, 33(201):209–220, 1892.

[94] Y. Renardy and M. Renardy. Prost: a parabolic reconstruction of surface tension for the volume-of-fluid method. *Journal of Computational Physics*, 183(2):400–421, 2002.

[95] F. Risso and J. Fabre. Oscillations and breakup of a bubble immersed in a turbulent field. *Journal of Fluid Mechanics*, 372:323–355, 1998.

[96] W. C. Sanders, E. C. Winkel, D. R. Dowling, M. Perlin, and S. L. Ceccio. Bubble friction drag reduction in a high-reynolds-number flat-plate turbulent boundary layer. *Journal of Fluid Mechanics*, 552:353–380, 2006.

[97] M. Sbragaglia, R. Benzi, L. Biferale, H. Chen, X. Shan, and S. Succi. Lattice boltzmann method with self-consistent thermo-hydrodynamic equilibria. *Journal of Fluid Mechanics*, 628:299, 2009.

[98] M. Sbragaglia, R. Benzi, L. Biferale, S. Succi, K. Sugiyama, and F. Toschi. Generalized lattice boltzmann method with multirange pseudopotential. *Physical Review E*, 75(2):026702, 2007.

[99] L. Scarbolo, D. Molin, P. Perlekar, M. Sbragaglia, A. Soldati, and F. Toschi. Unified framework for a side-by-side comparison of different multicomponent algorithms: lattice boltzmann vs. phase field model. *Journal of Computational Physics*, 234:263–279, 2013.

[100] L. Scarbolo and A. Soldati. Turbulence modulation across the interface of a large deformable drop. *Journal of Turbulence*, 14(11):27–43, 2013.

[101] R. Scardovelli and S. Zaleski. Direct numerical simulation of free-surface and interfacial flow. *Annual Review of Fluid Mechanics*, 31(1):567–603, 1999.

[102] J. A. Sethian. *Level set methods and fast marching methods: evolving interfaces in computational geometry, fluid mechanics, computer vision, and materials science*, volume 3. Cambridge university press, 1999.

[103] X. Shan. Pressure tensor calculation in a class of nonideal gas lattice boltzmann models. *Physical Review E*, 77(6):066702, 2008.

[104] X. Shan. Multicomponent lattice boltzmann model from continuum kinetic theory. *Physical Review E*, 81(4):045701, 2010.

[105] X. Shan. Multicomponent lattice boltzmann model from continuum kinetic theory. *Physical Review E*, 81(4):045701, 2010.

[106] X. Shan and H. Chen. Lattice boltzmann model for simulating flows with multiple phases and components. *Physical Review E*, 47(3):1815, 1993.

[107] X. Shan and H. Chen. Simulation of nonideal gases and liquid-gas phase transitions by the lattice boltzmann equation. *Physical Review E*, 49(4):2941, 1994.

[108] X. Shan and G. Doolen. Multicomponent lattice-boltzmann model with interparticle interaction. *Journal of Statistical Physics*, 81(1-2):379–393, 1995.

[109] X. Shan and G. Doolen. Diffusion in a multicomponent lattice boltzmann equation model. *Physical Review E*, 54(4):3614, 1996.

[110] X. Shan and X. He. Discretization of the velocity space in the solution of the boltzmann equation. *Physical Review Letters*, 80(1):65, 1998.

[111] X. Shan, X. Yuan, and H. Chen. Kinetic theory representation of hydrodynamics: a way beyond the navier-stokes equation. *Journal of Fluid Mechanics*, 550(1):413–441, 2006.

[112] M. Shapira and S. Haber. Low reynolds number motion of a droplet in shear flow including wall effects. *Int. J. Multiphase Flow*, 16(2):305–321, 1990.

[113] O. Shardt, J. J. Derksen, and S. K. Mitra. Simulations of droplet coalescence in simple shear flow. *Langmuir*, 29(21):6201–6212, 2013.

[114] D. N. Siebert, L. A. Hegele, R. Surmas, L. O. E. Dos Santos, and P. C. Philippi. Thermal lattice boltzmann in two dimensions. *International Journal of Modern Physics C*, 18(04):546–555, 2007.

[115] E. D. Siggia. Late stages of spinodal decomposition in binary mixtures. *Physical Review A*, 20(2):595, 1979.

[116] L. Sirovich. Kinetic modeling of gas mixtures. *Physics of Fluids*, 5:908, 1962.

[117] L. Sirovich. Mixtures of maxwell molecules. *Physics of Fluids*, 9:2323, 1966.

[118] S. Succi. *The lattice Boltzmann equation: for fluid dynamics and beyond*. Oxford university press, 2001.

[119] M. R. Swift, W. R. Osborn, and J. M. Yeomans. Lattice boltzmann simulation of nonideal fluids. *Physical Review Letters*, 75(5):830, 1995.

[120] G. I. Taylor. The formation of emulsions in definable fields of flows. *Proceedings of Royal Society A*, (146):501–523, 1934.

[121] Be A. Toms. Some observations on the flow of linear polymer solutions through straight tubes at large reynolds numbers. In *Proceedings of the 1st International Congress on Rheology*, volume 2, pages 135–141, 1948.

[122] P. Trontin, S. Vincent, J. L. Estivalezes, and J. P. Caltagirone. Direct numerical simulation of a freely decaying turbulent interfacial flow. *International Journal of Multiphase Flow*, 36(11):891–907, 2010.

[123] G. Tryggvason, R. Scardovelli, and S. Zaleski. *Direct Numerical Simulations of Gas-Liquid Multiphase Flows.* Cambridge University Press, 2011.

[124] M. Uhlmann. An immersed boundary method with direct forcing for the simulation of particulate flows. *Journal of Computational Physics*, 209(2):448–476, 2005.

[125] S. O. Unverdi and G. Tryggvason. A front-tracking method for viscous, incompressible, multi-fluid flows. *Journal of computational physics*, 100(1):25–37, 1992.

[126] T. H. van den Berg, S. Luther, D. P. Lathrop, and D. Lohse. Drag reduction in bubbly taylor-couette turbulence. *Physical Review Letters*, 94:044501, 2005.

[127] J. D. van der Waals. The thermodynamic theory of capillarity under the hypothesis of a continuous variation of density verh. k. akad. wet. amsterdam section 1 1 8 van der waals jd 1894. *Z. Phys. Chem*, 13:657, 1893.

[128] D. P. M. van Gils, D. Narezo Guzman, C. Sun, and D. Lohse. The importance of bubble deformability for strong drag reduction in bubbly turbulent taylor–couette flow. *Journal of Fluid Mechanics*, 722:317–347, 2013.

[129] P. S. Virk. Drag reduction fundamentals. *AIChE Journal*, 21(4):625–656, 1975.

[130] N. Vladimirova, A. Malagoli, and R. Mauri. Diffusion-driven phase separation of deeply quenched mixtures. *Physical Review E*, 58(6):7691, 1998.

[131] A. J. Wagner. The origin of spurious velocities in lattice boltzmann. *International Journal of Modern Physics B*, 17(01n02):193–196, 2003.

[132] A. J. Wagner. Thermodynamic consistency of liquid-gas lattice boltzmann simulations. *Physical Review E*, 74(5):056703, 2006.

[133] M. D. Warholic, G. M. Schmidt, and H. T. J. Hanratty. The influence of a drag-reducing surfactant on a turbulent velocity field. *Journal of Fluid Mechanics*, 388(1):1–20, 1999.

[134] C. M. White and M. G. Mungal. Mechanics and prediction of turbulent drag reduction with polymer additives. *Annu. Rev. Fluid Mech.*, 40:235–256, 2008.

[135] D. A. Wolf-Gladrow. *Lattice-gas cellular automata and lattice Boltzmann models: an introduction.* Number 1725. Springer, 2000.

[136] S-J. Wu, C-H. Hsu, and T-T. Lin. Model test of the surface and submerged vehicles with the micro-bubble drag reduction. *Ocean engineering*, 34(1):83–93, 2007.

[137] H. Yang, C. C. Park, Y. T. Hu, and L. G. Leal. The coalescence of two equal-sized drops in a two-dimensional linear flow. *Physics of Fluids (1994-present)*, 13(5):1087–1106, 2001.

[138] P. Yuan and L. Schaefer. Equations of state in a lattice boltzmann model. *Physics of Fluids*, 18:042101, 2006.

[139] P. Yue, J. J. Feng, C. Liu, and J. Shen. A diffuse-interface method for simulating two-phase flows of complex fluids. *Journal of Fluid Mechanics*, 515(1):293–317, 2004.

[140] P. Yue, J. J. Feng, C. Liu, and J. Shen. Diffuse-interface simulations of drop coalescence and retraction in viscoelastic fluids. *Journal of Non-Newtonian Fluid Mechanics*, 129(3):163–176, 2005.

[141] P. Yue, C. Zhou, and J. J. Feng. Spontaneous shrinkage of drops and mass conservation in phase-field simulations. *Journal of Computational Physics*, 223(1):1–9, 2007.

[142] P. Yue, C. Zhou, and J. J. Feng. Sharp-interface limit of the cahn–hilliard model for moving contact lines. *Journal of Fluid Mechanics*, 645:279–294, 2010.

[143] J. L. Zakin, B. Lu, and H-W Bewersdorff. Surfactant drag reduction. *Reviews in Chemical Engineering*, 14(4-5):253–320, 1998.

[144] J. Zhang and F. Tian. A bottom-up approach to non-ideal fluids in the lattice boltzmann method. *EPL (Europhysics Letters)*, 81(6):66005, 2008.

[145] S. Ziering and M. Sheinblatt. Kinetic theory of diffusion in rarefied gases. *Physics of Fluids*, 9:1674, 1966.

[146] F. Zonta, C. Marchioli, and A. Soldati. Modulation of turbulence in forced convection by temperature-dependent viscosity. *Journal of Fluid Mechanics*, 697:150–174, 2012.